AD-A037 163 STANFORD RESEARCH INST MENLO PARK CALIF F/G 20/5
LASER DAMAGE PHENOMENA IN MATERIALS.(U)
NOV 76 T J MAGEE, J PENG, R A ARMISTEAD F44620-73-C-0019
UNCLASSIFIED AFOSR-TR-77-0155 NL

1 OF 2
AD A037163

AD A037163

AFOSR - TR - 77 - 0155

Final Report
Covering the Period 1 November 1972 to 31 October 1976

November 1976

LASER DAMAGE PHENOMENA IN MATERIALS

By: T. J. MAGEE, J. PENG, and R. A. ARMISTEAD

Prepared for:

AIR FORCE OFFICE OF SCIENTIFIC RESEARCH
BOLLING AIR FORCE BASE
BUILDING 410
WASHINGTON, D. C. 20332

DDC
RECEIVED
MAR 18 1977
C

Contract F44620-73-C-0019

Reproduction in whole or in part is permitted for any purpose of the United States Government.

This research was sponsored by the Air Force Office of Scientific Research under AFOSR Contract F44620-73-C-0019.

DISTRIBUTION STATEMENT A
Approved for public release;
Distribution Unlimited

STANFORD RESEARCH INSTITUTE
Menlo Park, California 94025 · U.S.A.

1473

AIR FORCE OFFICE OF SCIENTIFIC RESEARCH (AFSC)
NOTICE OF TRANSMITTAL TO DDC
This technical report has been reviewed and is
approved for public release IAW AFR 190-12 (7b).
Distribution is unlimited.
A. D. BLOSE
Technical Information Officer

UNCLASSIFIED

SECURITY CLASSIFICATION OF THIS PAGE (When Data Entered)

AFOSR REPORT DOCUMENTATION PAGE

READ INSTRUCTIONS BEFORE COMPLETING FORM

1. REPORT NUMBER: AFOSR-TR-77-0155	2. GOVT ACCESSION NO.
3. RECIPIENT'S CATALOG NUMBER	
4. TITLE (and Subtitle): LASER DAMAGE PHENOMENA IN MATERIALS.	5. TYPE OF REPORT & PERIOD COVERED: Final - 1 November 1972-31 October 1976
	6. PERFORMING ORG. REPORT NUMBER
7. AUTHOR(s): T. J. Magee, J. Peng and R. A. Armistead	8. CONTRACT OR GRANT NUMBER(s): F44620-73-C-0019
9. PERFORMING ORGANIZATION NAME AND ADDRESS: Stanford Research Institute, Menlo Park, California 94025	10. PROGRAM ELEMENT, PROJECT, TASK AREA & WORK UNIT NUMBERS: 9751-01, 61102F, 01
11. CONTROLLING OFFICE NAME AND ADDRESS: AFOSR/NP, Bolling AFB, DC 20332	12. REPORT DATE: November 1976
	13. NUMBER OF PAGES: 117 (116 p.)
14. MONITORING AGENCY NAME & ADDRESS (if different from Controlling Office)	15. SECURITY CLASS. (of this report): UNCLASSIFIED
	15a. DECLASSIFICATION/DOWNGRADING SCHEDULE

16. DISTRIBUTION STATEMENT (of this Report)

Approved for Public Release; Distribution Unlimited

Final rept. 1 Nov 72-31 Oct 76,

17. DISTRIBUTION STATEMENT (of the abstract entered in Block 20, if different from Report)

18. SUPPLEMENTARY NOTES

19. KEY WORDS (Continue on reverse side if necessary and identify by block number)

Scanning electron microscopy	Plasma diagnostics
Laser damage	Color centers
Laser interactions	Laser calorimetry
Laser-induced pressure	Infrared absorption

20. ABSTRACT (Continue on reverse side if necessary and identify by block number)

This report describes progress on a program to characterize laser-induced damage in selected materials and to identify the role of microstructural defects and radiation damage in altering infrared transmission of laser windows and optical coatings.

DD FORM 1 JAN 73 1473 EDITION OF 1 NOV 65 IS OBSOLETE

UNCLASSIFIED 332 500

SECURITY CLASSIFICATION OF THIS PAGE (When Data Entered)

INTRODUCTION

The objectives of this program were to provide a detailed evaluation of the interaction of a high-power laser beam with selected materials and to identify the influence of inherent or induced defects on the development of damage within these materials. The program has included:

- Design, development, and calibration of a coupled laser-scanning electron microscope (SEM) system for in-situ examination of laser damage to selected material during pulsed laser bombardment or subsequent to CW laser exposure.
- Evaluation of the mechanisms of damage to window materials during pulsed or CW laser exposure.
- Identification of microstructural defects in CdTe and correlation with increased infrared absorption at 10.6 μm.
- Microstructural evaluation of polycrystalline ZnSe laser window materials and identification of defects responsible for localized banding and scatter at 10.6 μm.
- Evaluation of the influence of coatings on the magnitude of laser-induced stresses in materials.
- Correlation of the induced stress wave profiles and the dynamics of the plasma produced by laser irradiation of plane solid targets.
- Identification of the transient and permanent changes in the infrared absorption of single crystal and polycrystalline (mixed) KCl samples exposed to pulsed or CW ionizing radiation.
- Investigation of the influence of microdefects on the radiation induced infrared absorption of ZnSe at 10.6 μm.

DDC
MAR 18 1977

This report summarizes progress and results obtained during the research program. Interim Annual Reports 1 to 3 and journal articles 1 through 11 provide detailed descriptions of the research. Reprints of articles are attached as Appendices A through H.

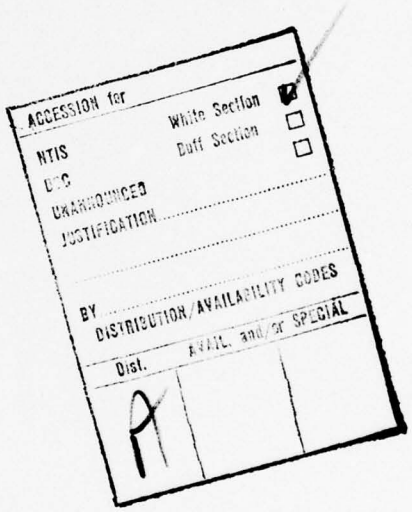

PROGRAM SUMMARY

During the first year of this program, we developed a system for examining in situ the development of microstructural surface damage during laser irradiation. For this system, a scanning electron microscope (SEM) was modified to accept a laser beam into the sample cavity. Electronic triggering circuitry was developed to allow monitoring of the surface during CW laser irradiation or after pulsed laser bombardment by the introduction of a fixed delay between the firing of the laser and the initiating of a single-raster SEM scan. The SEM was then used to obtain information on the development of damage as a function of laser intensity and irradiation time.

During the second year of the program, research continued on the evaluation of parameters influencing the progression of damage in selected IR laser window materials. We conducted a detailed evaluation of microstructural defects in CdTe and correlated the data with the infrared absorption coefficient at 10.6 μm. The influence of thin-film coatings on the magnitude of laser-induced stress in targets was also investigated, and initial work was begun on the correlation between measured plasma profiles and momentum transfer in a sample irradiated by a pulsed laser beam.

In the third year, we completed the analysis of plasma expansion and momentum transfer at the surface of laser-irradiated targets, and conducted experiments on mixed and single crystal KCl samples to assess the influence of high-energy electrons on the infrared absorption at 10.6 μm. The studies included simultaneous CW electron and F-light irradiation to determine the correlation between F-aggregate centers

and infrared absorption. In addition, during this period, we completed the identification of scatter and absorption sites responsible for the decreased infrared transmission in polycrystalline ZnSe samples.

In the final year, we investigated the influence of pulsed ionizing radiation on the transient and steady-state infrared absorption of single crystal KCl and polycrystalline KCl-$EuCl_2$ mixed samples. The objective of these studies was to determine the correlation between possible "spike" infrared absorption during and subsequent to pulsed ionizing radiation and the creation/annihilation times for F- and F-aggregate centers. Using a pulsed 600 kV electron beam of 3-ns duration, we found that the F-center absorption increased rapidly during the first 200 ns after electron-beam irradiation. Subsequent F-center absorption increased slowly and reached a saturation limit after $\simeq$ 1 μs. Simultaneous exposure of the sample to Hg lamp illumination and pulsed electron irradiation resulted in a slow ($t > 1$ μs) conversion of F-centers to M-centers. Thus, the results indicate two regions of radiation induced 10.6 μm absorption. The first "spike" absorption occurs within 200 ns after electron-beam irradiation and is correlated with rapid charge mobility and creation of F-centers in the KCl. The second 10.6 μm absorption region is correlated with F to M conversion and occurs slowly at $t > 1$ μs after electron irradiation. The steady-state 10.6 μm absorption was shown to be proportional to the M-center density, which is in agreement with results obtained earlier in this research program.

CUMULATIVE LIST OF PUBLICATIONS
(AFOSR CONTRACT F44620-73-C-0019

1. T. J. Magee and P. Krehl, "Studies of Laser-Metal Interactions Using a Coupled Laser-SEM System," Proceedings of the Electron Microscopy Society of America (Claitor Publishing Company, Baton Rouge, Louisiana, 1973).

2. T. J. Magee, J. Peng, and J. Bean, "Preparation of Thin CdTe Samples for Electron Microscope Studies," Proceedings of the Electron Microscopy Society of America (Claitor Publishing Company, Baton Rouge, Louisiana, 1974).

3. T. J. Magee, P. Krehl, K. Hirschberg, and J. Terry, "A Coupled Laser-Scanning Electron Microscope System for Investigating Laser-Materials Interactions," Rev. Sci. Instr. 45, 907 (1974).

4. T. J. Magee, J. Peng, and J. Bean, "Microscopic Defects and Infrared Absorption in Cadmium Telluride," Physica Status Solidi (A) 27, 557 (1975).

5. T. J. Magee, R. A. Armistead, and P. Krehl, "Laser Induced Stresses in Coated and Uncoated Targets," J. Physics (D) 8, 498 (1975).

6. P. Krehl, F. Schwirzke, and A. W. Cooper, "Correlation of Stress Wave Profiles and the Dynamics of the Plasma Produced by Laser Irradiation of Plane Solid Targets," J. Appl. Phys. 46, 4400 (1975).

7. T. J. Magee, N. Johnson, and J. Peng, "The Influence of High Energy Electron Irradiation on the 10.6 μm Absorption of Mixed KCl Crystals," Physica Status Solidi (A) 30, 81 (1975).

8. T. J. Magee, N. M. Johnson, and J. Peng, "The Effect of Illumination on the 10.6 μm Absorption Coefficient of Electron Irradiated Single Crystal KCl," Physica Status Solidi (A) (1976).

9. T. J. Magee, N. M. Johnson, M. Lehmann, J. Peng, and J. Hannigan, "Compact Laser Calorimeter for Measuring Absorption Coefficients of Small Samples," Rev. Sci. Instr. 47, 301 (1976).

10. R. A. Armistead and T. J. Magee, "Laser Damage Phenomenology in Materials," Presented at Fourth International Conference on Laser Interaction and Related Plasma Phenomena, November 8-12, 1976, Troy, N.Y. (to be published 1977, Plenum Publ. Corp.).

11. T. J. Magee, J. Peng and R. A. Armistead, "Transient Absorption in KCl Produced by Pulsed Electron Beam Irradiation," (to be published).

APPENDIX A

REPRINT

"CORRELATION OF STRESS WAVE PROFILES AND THE DYNAMICS OF THE PLASMA PRODUCED BY LASER IRRADIATION OF PLANE SOLID TARGETS"

By

P. Krehl, F. Schwirzke and A. W. Cooper
(Journal Applied Physics 46, 4400 (1975))

Correlation of stress-wave profiles and the dynamics of the plasma produced by laser irradiation of plane solid targets

P. Krehl*

Poulter Laboratory, Stanford Research Institute, Menlo Park, California 94025

F. Schwirzke and A. W. Cooper

Department of Physics, Naval Postgraduate School, Monterey, California 93940
(Received 17 March 1975)

The interaction of 20-nsec 300-MW pulses of 1.06-μm laser radiation with thick aluminum targets in vacuum has been studied. The time history of the target impulse has been measured with a Sandia quartz gauge. A time sequence of plasma density maps constructed from floating double-probe data has been used with measured expansion velocities to estimate the plasma momentum. The results show that the stress wave is predominantly produced by about 10% of the evaporated target material which is ionized and expands from the surface in the form of a hot plasma during and shortly after the laser pulse. The estimated momentum of the plasma and neutral emitted particles is 5.6 gcm/sec for a typical case compared with the measured target impulse of 6.1 gcm/sec.

PACS numbers: 52.50.J, 79.20.D

I. INTRODUCTION

In the interaction of high-power pulsed laser radiation with a solid target, gas breakdown and subsequent plasma formation in the vicinity of the surface dominate the later transfer of energy and momentum to the solid. Studies of the interaction in an air atmosphere have demonstrated the appearance of laser-supported absorption waves,[1-3] initiated by air breakdown close to the surface and propagating in the direction of the laser. After the initiation the target is partially or completely shielded from the incoming radiation by the absorbing plasma layer, and further momentum transfer to the target occurs through pressure buildup behind the shock front.[4,5] In this way the magnitude of the target impulse may be increased above the vacuum value, and its duration extended beyond the laser pulse length. The target heating is by energy transfer from the shocked air, and the heated area may be many times the focal spot size. In the absence of atmosphere, a hot dense plasma is formed on the surface by initial ablation of target material and further ionization and heating by laser radiation absorbed through the inverse bremsstrahlung mechanism in the plasma layer at critical density. At plasma densities above critical, radiative transport of laser energy is cut off, and heat conduction by electrons becomes the principal mechanism of energy transport through the overdense plasma to the target. Temperature and density gradients determine the dynamics of the expanding plasma; thus the target effects in the interaction depend not only on the intensity, pulse duration, and wavelength of the laser, but also on the plasma parameters which determine the transport of energy and momentum to the surface. Previous measurements have been reported[6] of the total impulse transmitted to thin targets in vacuum, as measured with a ballistic pendulum. In the present investigation the continuous time history of the target impulse has been measured with a quartz pressure gauge,[7] in plasma properties measured under almost identical conditions. The objective of this study was to correlate the measured dynamics of the plasma with the stress pulses propagating into the target.

II. PLASMA PRODUCTION BY LASER IMPACT AND STRESS PRODUCTION

The "skin depth" for the high-frequency radiation of a neodymium laser in aluminum is only 50 Å. The number of atoms exposed to the radiation in the small disk given by this skin depth and a focal spot of 5-mm diameter is about 6×10^{15}. To ionize these particles and heat the plasma to a few eV would require only about 10^{-2} J, a small fraction of the available laser pulse energy of about 6 J. Hence, a dense high-temperature plasma layer is produced immediately after laser onset. The rapid ionization and heating of the target material generates a plasma of almost solid-state density with particle density ranging from $n\sim10^{22}$ to 10^{23} cm^{-3}. The plasma frequencies corresponding to these densities are higher than the neodymium laser frequency, so that further propagation of the laser radiation to the target beyond the critical plasma density of $n_c\simeq10^{21}$ cm^{-3} is inhibited. Most of the laser radiation is then absorbed via inverse bremsstrahlung in a thin layer of plasma in

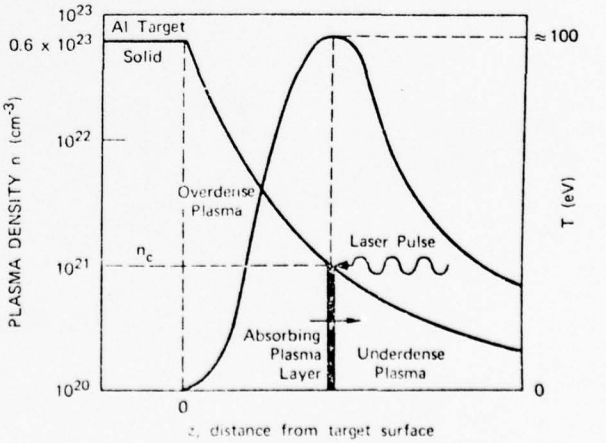

FIG. 1. Schematic of plasma density and plasma temperature in front of a solid target. The incident laser light is absorbed in a thin layer near the critical density $n_c\simeq10^{21}$ cm^{-3}, resulting in rapid heating and expansion.

 Copyright © 1975 American Institute of Physics

front of the target where the plasma frequency is close to the laser frequency. This is shown schematically in Fig. 1.

The heating process produces temperature and pressure gradients. The temperature gradient causes electronic heat conduction through the overdense plasma to the target and thus further vaporization and ionization of the target material. Pressure gradients cause the plasma to expand, with the absorbing plasma layer at the critical density propagating towards the laser in the form of a laser-supported detonation wave.

The temperature of the plasma is determined by the rate of energy increase due to laser heating and the rate of energy loss due to plasma expansion. The ions and electrons are assumed to have the same temperature and propagation velocity so that the plasma can be regarded macroscopically as quasineutral. The plasma expands adiabatically and most of the thermal energy of the plasma shows up as kinetic expansion energy of the ions. After laser shutoff the acceleration rapidly approaches zero and the plasma expansion velocity approaches an asymptotic value as the temperature decreases to small values.

The evaporation of target material and the subsequent laser heating of the plasma at the critical density layer produce a stress pulse which propagates into the target. Damage to the target can be observed in the form of mass ejecta craters and fractures, depending upon the energy density of the laser beam and the pulse duration. Even after laser shutoff, vaporization of surface material will continue for an appreciable time until the surface temperature decreases below the vaporization temperature. Obviously, a detailed description of the plasma and neutral particle blowoff from the target surface is involved. However, a description of the processes in the laser-heated surface layers can be avoided, when, as in shock-wave theory, the conservation of mass, momentum, and energy is considered. The mechanical impulse $i(t)$ resulting from the blowoff of target material is given by the integral

$$i(t) = A \int_0^t P_t(t)\,dt, \tag{1}$$

with A being the area of the focal spot and $P_t(t)$ the stress in the target. The impulse is produced by the neutral and charged particles which leave the target surface in the normal direction (at low energy) or which impact the surface from the rapidly expanding plasma layer (at high energy):

$$i(t) = m_i v_i(t) N_i(t) + m_e v_e(t) N_e(t) + m_n v_n(t) N_n(t),$$

with v, m, and N being the velocity, number, and mass of the ions, electrons, and neutral atoms. Since the plasma is quasineutral, $v_e \approx v_i$ and with $m_i \approx m_n$ one obtains, neglecting the small contribution of the impulse of the electrons, $m_i \gg m_e$,

$$i(t) = m_n [v_i(t) N_i(t) + v_n(t) N_n(t)]. \tag{2}$$

The contribution of the neutral atoms to the impulse cannot be measured directly. However, during and just after laser impact, the evaporated target material has still a high temperature and is mostly ionized, so that Eq. (2) can be simplified to

$$i(t) = m_n v_i(t)\, N_i(t).$$

The velocity of the ions, $v_i(t)$, can be measured with an electrostatic double probe and the number of ions $N_i(t)$ can be estimated from a spatial integration of the ion density distribution of the plasma cloud so that the impulse $i(t)$ due to the plasma blowoff can be determined.

III. EXPERIMENTAL

A schematic of the experimental arrangement is shown in Fig. 2. The laser used is a Q-switched Korad K-1500 oscillator-amplifier neodymium system with an output ranging from 4 to 11.5 J. The pulsewidth at half-peak-power is 25 nsec. The $\frac{3}{4}$-in.-diam beam is focused by means of a 28-cm-focal-length lens into a vacuum chamber and strikes the target at an angle of 30° with respect to the target normal. The resultant plasma expands along the target normal. The choice of a 30° incident angle permits probing of the plasma along the target normal without having the laser beam strike the probes. Two different focal spot sizes of 5- and 1.5-mm

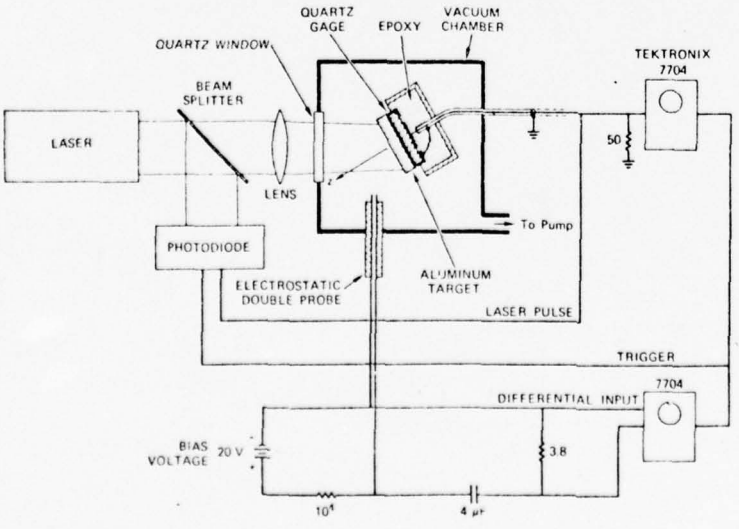

FIG. 2. Experimental configuration for measuring plasma density and expansion velocity in front of the target and stress-wave propagation in its interior.

diameter were used. A large focal spot size is required for proper stress profile measurement, while a small focal spot size permits plasma density probing for nearly the whole outer half-space with the exception only of the incident narrow laser beam cone.

The target consists of 1145-aluminum and is a disk of 10-mm diameter and 2-mm thickness. It is glued by epoxy on a 1-mm-thick quartz stress gauge (Valpey Corp.) of the Sandia type.[7] Using a shunt resistor of 50 Ω, the sensitivity of the gauge is 1.09 mV/bar. The recording time of the stress history is determined by the thickness of the gauge and amounts to 175 nsec. A longer regime would be desirable for shots in air, but would require a thicker gauge. To provide at least a ratio of 5:1 for the inner electrode diameter to the gauge thickness, which is a condition for proper gauge operation, a larger focal spot size would be necessary for homogeneous loading conditions. However, to maintain the same power density in the focal spot, a higher energy, exceeding that available, would be required. The propagation time of the stress wave from the front to the back surface of the target is 311 nsec and is large compared to the recording time of the stress gauge, so that reflections at the interface of target and gauge cannot interfere.

The laser pulse is monitored with a photodiode and is displayed for time reference together with the stress pulse.

The dynamics of the plasma are investigated by means of an electrostatic double probe[8] which permits local measurement of the plasma density as a function of time. For accurate determination of the velocity of the expanding plasma body, a tandem double probe was used to allow simultaneous sampling of the same plasma. The double-probe circuit was electrically isolated from the target and chamber, thus overcoming the problem of providing a stable reference potential in electrical contact with the plasma as required for single-probe operation. The floating double probe consists of two identical small tungsten wires of 0.024-cm diameter with a spacing of 0.08 cm, projecting 0.19 cm from the end of a thin insulating shaft and connected externally to a 20-V potential source and a 3.8-Ω resistor for current readout. The double probes were always oriented with the plane of the wires normal to the plasma expansion direction. The ion density n_i can be evaluated as[9]

$$n_i = 1.59 \times 10^{20}\, U/v_i \text{ cm}^{-3}, \tag{3}$$

where U (V) is the probe output voltage generated across 3.8 Ω and v_i (cm/sec) the ion velocity. The typical oscilloscope setting of 100 nsec/div and 2 V/div gave a measurement sensitivity of about 10^{12} cm^{-3} or 1%. The detection limit was approximately 1×10^{11} cm^{-3}.

IV. EXPERIMENTAL RESULTS

A. Stress-wave measurements

For a focal spot size of only 5 mm, the strain in the quartz is no longer uniaxial, because rarefaction waves from the border of the target and the gauge make the stress-wave profile narrower than the 5-mm diameter of the inner electrode of the gauge. Since the velocities of the stress wave and the rarefaction are closely similar, the stress profile reduces at about a 45° angle. In this case the measured pressure profiles must be corrected both in shape and amplitude. The correction required can be obtained empirically from gas gun experiments in which a known shock stress is imparted to the gauge by impact of a projectile with a 5-mm-diam head, and the resulting gauge output associated with the magnitude of the input stress. The measured stress in the quartz, P_q, must be related to the stress in the target, P_t. For waves that are linearly elastic, the relation is

$$P_t = P_q(v_q\rho_q + v_t\rho_t)/2v_q\rho_q, \tag{4}$$

where ρ is the initial density and v the elastic wave velocity of either the quartz or the target. For aluminum as target material, Eq. (4) becomes $P_{al} = 1.07P_q$.

It should be noted that for inhomogeneities in the target, such as large grain sizes or textures, the stress at the entrance surface of the target might differ considerably from the stress the gauge receives. Since the rise time of the pressure pulse can amount only to a few nanoseconds, high-frequency harmonic components in the pulse would be attenuated significantly, resulting in a considerable deformation of the pressure pulse.

Typical stress-time profiles in an aluminum target for a shot in vacuum (10^{-5} Torr) and in air at atmospheric pressure are shown in Fig. 3a. The stress pulse rises nearly as steeply as the laser pulse and reaches a peak pressure of 800 bar. For a shot in air, which is shown only for comparison, but not used later

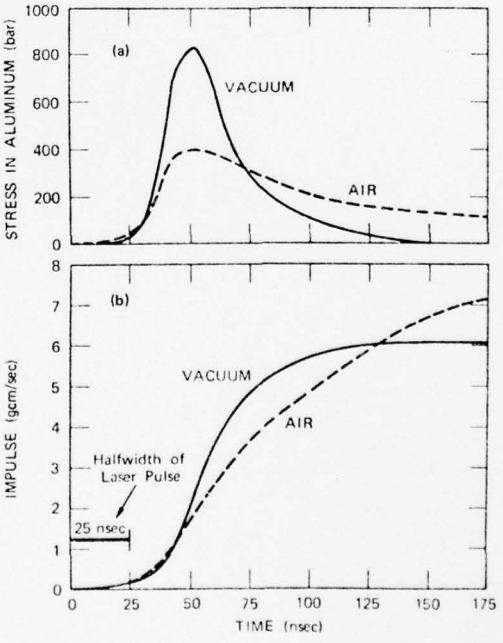

FIG. 3. (a) Reproduction of oscillograms from recording of stress-time history for laser irradiance of an aluminum target in air and vacuum at 5-mm focal spot diameter. (b) Corresponding impulse-time histories obtained by graphical integration of the stress-time profiles.

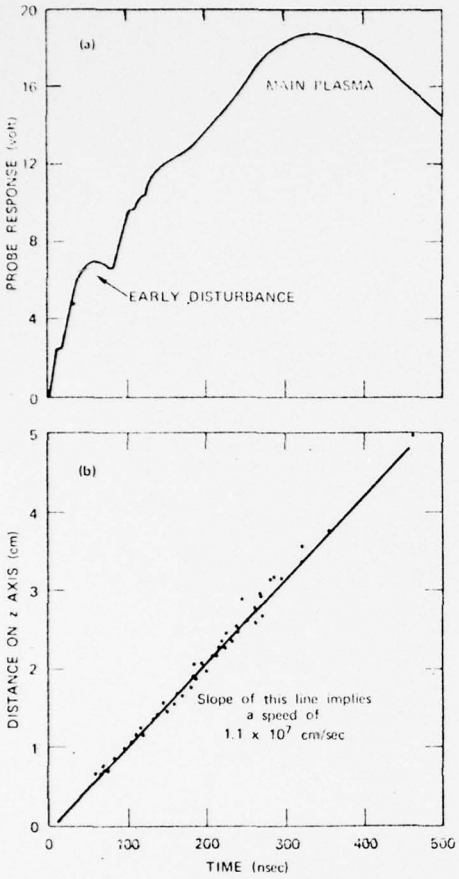

FIG. 4. (a) Typical response of an electric double probe, located 0.6 cm from the target surface on the normal axis. An early disturbance precedes the main plasma body. (b) Time of passage of the main plasma front versus probe position (Ref. 9).

for correlation with plasma measurements, the peak pressure is less than half of that obtained for a shot in vacuum. However, the stress pulse lasts longer than the laser pulse and exceeds even the recording time of the stress gauge.

To determine the impulse $i(t)$ these stress profiles were graphically integrated and are shown in Fig. 3(b). It is obvious that the rate of momentum transfer increases during the duration of the laser pulse, decreases after shutoff, and ceases at about 120 nsec. During laser irradiation, the impulse has reached only a fraction of its final value, independently of the ambient pressure. For laser irradiation in vacuum, the impulse reaches a final value during the recording time of the gauge. Although the peak pressure of an air shot is only half that of a vacuum shot, the total impulse and also the total mass removal are higher than for a shot in vacuum.

B. Plasma measurements

The ion density profiles of the expanding plasma plume were taken with the same laser energy, but smaller focal spot of 1.5-mm diameter. Comparative experiments revealed that in this range of power densities no significant differences in the expansion behavior occur. However, a small focal spot size allows a narrower cone of the incident laser beam and therefore probing of larger solid angles of the outer half-space. The expansion velocity has been measured and the plasma density has been mapped by using electrostatic double probes. A typical probe response is traced in Fig. 4(a). The main plasma front passage times were measured as function of probe distance z from the target [Fig. 4(b)]. As can be seen, the plasma front propagates with the asymptotic expansion velocity $v_i = 1.1 \times 10^7$ cm/sec. Two low-density fast plasma pulses were observed before arrival of the main plasma, traveling with constant speeds of 1.1×10^8 and 5.9×10^7 cm/sec.

Relative density contour maps of the expanding plas-

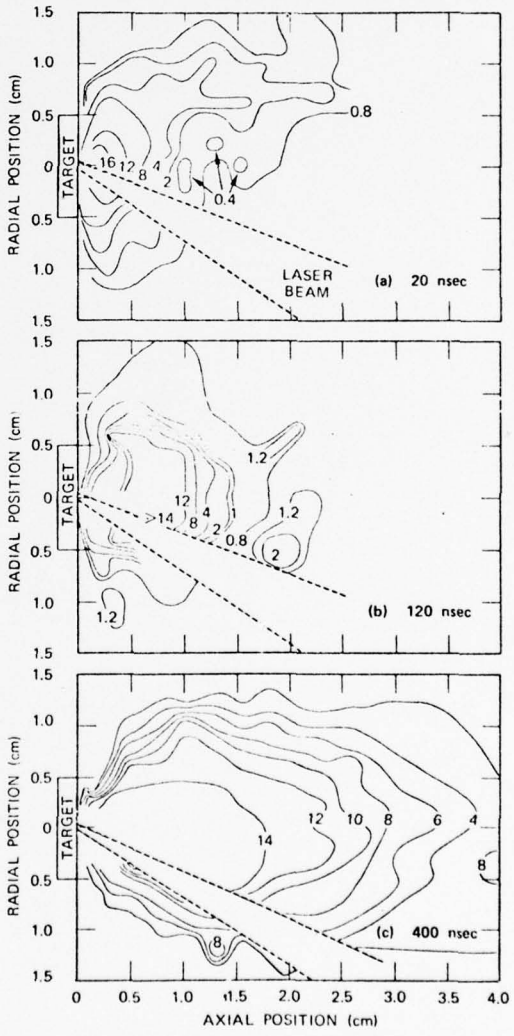

FIG. 5. Laser-produced plasma relative density contours for target irradiance in vacuum at three different time instants (after Brooks, Ref. 9): (a) Propagation of the fast early disturbance with about 1.1×10^8 cm/sec. (b) Detachment of the main plasma body from the target with about 1.1×10^7 cm/sec. (c) Later expansion of the main plasma with about 5×10^6 cm/sec.

ma for different times are given in Fig. 5(a)–5(c). For the early plasma pulse, the probe response was mapped at 20 nsec, i.e., during laser irradiation. The density map [Fig. 5(a)] shows that at this time the early expansion propagates along the reflected laser beam and separates from the main plasma pulse. The early disturbance then moves rapidly out of the observation region, and subsequent figures at later times contain only main plasma contours. For times greater than 50 nsec, the plasma expands symmetrically around the target normal. The self-induced magnetic fields in the plasma create a confining force that produces the typical cylindrical shape of the plasma plume.[10] At later times, the expansion of the plasma slows down and the innermost contour, representing the highest measured ion density, reaches its largest extent at 400 nsec.

V. DISCUSSION

For a quantitative correlation between stress profiles and plasma dynamics, the absolute number of ions $N_i(t)$ has to be determined. This involves the problem of transforming the relative ion density contours of Fig. 5(a)–5(c) [i.e., the voltage contours $U_i(t)$] into absolute ion densities $n_i(t)$. This can be accomplished directly by applying Eq. (3) only if the appropriate v_i of every contour is known. Out of a sequence of density contour maps taken at intervals of 10 nsec, one can determine the propagation velocities of the contours which until 120 nsec after laser onset are very close to the velocity of the leading edge of the main plasma body, i.e., 1.1×10^7 cm/sec. However, at later times [e.g., at 400 nsec, Fig. 5(c)] the plasma ion cloud expands more slowly in the radial than in the axial direction; the difference is about 50%. Therefore, at later times the ion velocity differs along the voltage contours so that the shape of the estimated absolute ion density map is no longer identical with the measured relative ion density map. However, reasonable estimates can be made from a time sequence of density contours. From the density contour maps of Fig. 5, the number of ions at three different times can be estimated: $N_i(20\text{ nsec}) = 1\times10^{14}$; $N_i(120\text{ nsec}) = 5\times10^{14}$, and the maximum $N_i(400\text{ nsec}) = 1\times10^{16}$. This shows that the number of particles in the early pulse is estimated to be about 1% of the main plasma. It also shows that the number of ions can still increase after laser irradiation has ceased, perhaps by particle flow from the inner core of the plasma cloud to outer parts. Experiments by others have shown that the core which detaches from the target and moves towards the laser has a high plasma temperature and therefore represents a considerable source of soft x-rays.[11] The ion density in the core cannot be measured by the electric probe because of its limited dynamic range. However, it is quite possible that the core contains a high ion density at 120 nsec which is partly released at 400 nsec and measured by the probe. Assuming that the 10^{16} ions measured at 400 nsec already existed at 120 nsec, at which time the density contour lines are traveling with approximately the front velocity of 1.1×10^7 cm/sec, the total plasma momentum in the direction normal to the target can be estimated as 5.0 g cm/sec.

To estimate the total momentum transferred to the laser-irradiated target, one must determine also the number of neutral atoms evaporated per shot [see Eq. (2)]. The target was weighed before and after a total of 234 shots.[9] For an average incident pulse of 300 MW, about 10^{17} aluminum atoms were removed per shot. Since the total number of ions amounts to 10^{16}, it can be concluded that 90% of the particles ejected per incident laser pulse are neutral atoms which evaporate from the target.

To gain further insight into this evaporation process, a theoretical model was assumed to predict the temperature rise at the surface and in the target as a function of time. The model assumes uniform radiation incident normally on an infinite plane solid so that heat flow is one-dimensional, that all incident energy is absorbed and not shielded by a plasma skin at critical density, that the thermal properties of the medium do not change with power density or temperature, and that the medium does not undergo a phase change. The laser pulse is assumed Gaussian in time. The solution is compared with that for a rectangular pulse of pulsewidth 2δ and amplitude P_0, having the same energy as the Gaussian pulse. The Gaussian pulse can be regarded as a sum of q columns of equal width τ, but varying power density. Since a rectangular pulse of duration τ can be written as the difference of two Heaviside functions which are given in the literature,[12] the change in temperature ΔT can be defined as a superposition of all the temperature-time profiles of the individual columns. The solution is given by

$$\Delta T(Z,t) = \frac{4P_0}{K}\left(\frac{\ln 2}{\pi}\right)^{1/2}\left[\sum_{q=1}^{q}\exp\left(\frac{-(q\tau-\delta)}{2\delta^2}\right)\{\kappa[t-(q-1)]\tau\}^{1/2}\right.$$
$$\times\sum_{n=0}^{\infty}\left(i\mathrm{erfc}\,\frac{(2n+1)d-Z}{2[\kappa t-(q-1)\tau]^{1/2}}\right.$$
$$\left.+\,i\mathrm{erfc}\,\frac{(2n+1)d+Z}{2\{\kappa[t-(q-1)]\tau\}^{1/2}}\right)-[\kappa(t-q\tau)]^{1/2}$$
$$\left.\times\sum_{n=0}^{\infty}\left(i\mathrm{erfc}\,\frac{(2n+1)d-Z}{2[\kappa(t-q\tau)]^{1/2}}+i\mathrm{erfc}\,\frac{(2n+1)d+Z}{2[\kappa(t-q\tau)]^{1/2}}\right)\right].$$

For aluminum as the target material, K is the thermal conductivity $= 2.37$ W/cm °K, κ is the thermal diffusivity $= 0.97$ cm^2 sec^{-1}, P_0 is the power density of rectangular pulse $= 1.29\times10^9$ W/cm^2, $q = 2\delta/\tau$ is the number of columns, τ is time (sec), Z is depth (cm), starting at the back side of target of thickness d (cm), $\sigma = \delta/(2\ln 2)^{1/2}$ (sec).

Figure 6 shows the total temperature-time profiles for different depths in the target. The time where the surface temperature exceeds the evaporation temperature is very long, about 10 μsec. Therefore it can be concluded that the process of evaporation lasts at least several orders of magnitude longer than the onset of laser irradiation. The figure also shows that the temperature decays very fast under the surface and that the stress wave propagates into a medium which is still at room temperature.

The average thermal velocity of the neutral atoms can be determined by

$$\bar{v}_n = (3kT/m)^{1/2}, \tag{5}$$

where k is the Boltzmann constant, T is the absolute temperature, and $m = 4.5\times10^{-23}$ g is the mass of the aluminum atom. For the evaporation temperature of aluminum, $T = 2333$ °K, Eq. (5) becomes $\bar{v}_n = 1.46\times10^5$ cm/sec.

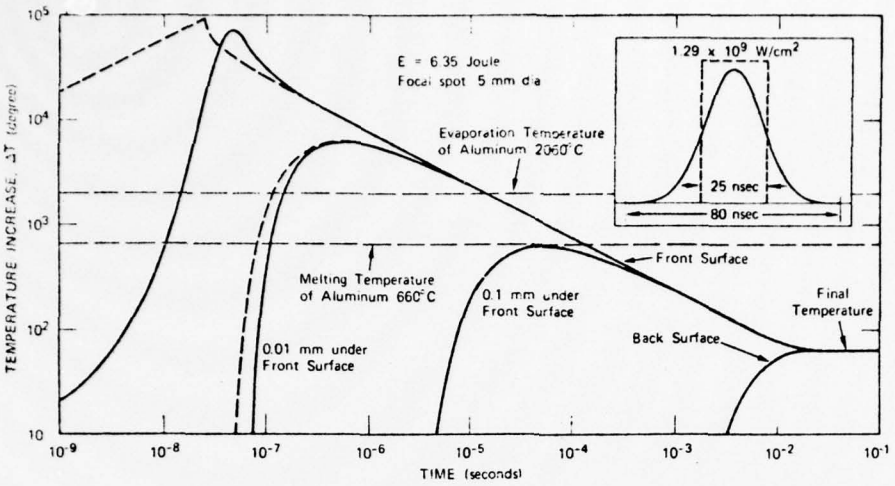

FIG. 6. Computed target temperature as function of time after laser onset of radiation on an infinite aluminum slab target of 2-mm thickness. Solutions are shown for a Gaussian pulse (solid curve) and for an assumed ideal rectangular pulse (broken curve) of the same energy, both starting at time zero. These curves show no appreciable difference after the first 100 nsec.

The degree of ionization α of the evaporated material at temperature T can be estimated by the Saha equation[13]

$$\alpha = \left(\frac{2P_i}{P_n}\right)^{1/2} \frac{(kT)^{3/4}}{\sqrt{n}} \left(\frac{2\pi m_e}{h^2}\right)^{3/4} \exp\left(-\frac{eV}{2kT}\right),$$

where P_i and P_n are the internal partition functions of the singly ionized and of the neutral target material, $n = n_e + n_i + n_n \approx 10^{23}$ particles/cm^3 (solid density assumed), m_e is the mass of electron $= 9.1 \times 10^{-28}$ g, h is Planck's constant $= 6.626 \times 10^{-27}$ erg sec, V is the ionization potential $= 5.96$ V. As Table I shows, the degree of ionization is small for evaporated material, even if the temperature is several thousand degrees above the boiling point. Also the velocity of the neutral atoms remains small compared to the ion velocity $v_i = 1.1 \times 10^7$ cm/sec. Thus plasma development in the vaporized metal followed by energy absorption through the inverse bremsstrahlung process must be invoked to account for the measured plasma densities, which must therefore occur during the laser pulse. We assume that the plasma at this time is highly ionized and expanding rapidly, while surface material evaporated later by residual target heat and by heat transport through the plasma remains un-ionized and expands at the ion thermal velocity corresponding to the vaporization temperature. Since we have 0.9×10^{17} neutral atoms leaving the target surface with an average speed of at least 1.4×10^5 cm/sec, the impulse contributed by the neutral particles amounts to about 0.6 g cm/sec. This added to 5 g cm/sec contributed by the ions gives an estimated total impulse of 5.6 g cm/sec, which is in reasonable agreement with the measured impulse of 6.1 g cm/sec.

A similar comparison can be carried out at an earlier time, before the measured impulse has reached its maximum. Using the plasma density contours at 20 nsec from Fig. 5(a) and the "early plasma" expansion velocity we arrive at an impulse of 0.1 g cm/sec, which agrees with the measured pressure gauge reading for the same time from Fig. 3(b).

VI. CONCLUSIONS

Measurements have been made of the time-resolved plasma density contours and expansion velocities produced by laser irradiation of a solid target, and comparisons have been made with target impulse measured with a quartz pressure gauge. Integration of the density contours has indicated a total ion number of 10^{16} per laser pulse, while mass removal measurements show that 10^{17} aluminum atoms are removed from the target by each pulse. Thus 10% of the total ejected mass appears in ionized form. A comparison of the momentum of these ions with the response of the stress gauge shows that the ionized particles account for 80% of the total momentum transferred to the target. Attributing the thermal velocity at evaporation temperature to the neutral atoms ejected accounts for a further 10%: the remaining 10% may be related to undetected ions or to an underestimate of the neutral particle expansion velocity. This indicates that the target impulse is dominated by the fast-moving ionized component of the blowoff material. It is also possible to correlate the time history of the impulse with the laser pulse. Comparison of the density contours with the pressure-time record indicates that the plasma cloud detaches from the target as the impulse reaches its maximum value. The example cited shows agreement to 10%. Inherent limitations on the method make it impractical to attempt a more precise comparison. The use of electrostatic probes for plasma density determination with the need for the absolute particle velocity in the calibration rela-

TABLE I. Dependence of Saha-equation predictions of degree of ionization α, and neutral atomic thermal velocity for evaporated target material, on target surface temperature. P_i and P_n are ion and neutral partition functions.

T (°K)	P_i	P_n	α	v_n (10^5 cm/sec)
2000	1	5.692	8.62×10^{-10}	1.35
3000	1	5.792	3.68×10^{-7}	1.66
4000	1	5.843	8.08×10^{-6}	1.92
5000	1	5.874	5.37×10^{-5}	2.14
6000	1	5.895	1.94×10^{-4}	2.34
7000	1	5.947	4.94×10^{-4}	2.53

tion, and the limited dynamic range which prevents the measurement of the higher-density contours, limit the precision of the plasma measurement of the neutral particle component.

ACKNOWLEDGMENTS

The authors wish to thank H. M. Herreman for careful experimentation, and Dr. W. Murri for stimulating discussions and help in setting up the gas gun calibration tests for the quartz gauge. Thanks are due to K. Brooks who performed the measurements of the plasma density contours as a portion of his M.S. research. This work was supported by the Air Force Office of Scientific Research and by the Office of Naval Research.

*Present address: Ernst-Mach-Institut, Freiburg/Breisgau, West Germany.

[1]S. A. Ramsden and P. Savic, Nature (Lond.) 203, 1217 (1964).
[2]P. E. Nielson and G. H. Canavan, Laser Division Digest, Report No. AFWL-LRD-71-2, 1971 (unpublished).
[3]R. Hall, Report AFWL-TR-73-28, 1973 (unpublished).
[4]A. N. Pirri, R. Schlier, and D. Northam, Appl. Phys. Lett. 21, 79 (1972).
[5]A. N. Pirri, Phys. Fluids 16, 1435 (1973).
[6]D. W. Gregg and S. J. Thomas, J. Appl. Phys. 37, 2787 (1966).
[7]R. A. Graham, F. W. Neilson, and W. B. Benedick, J. Appl. Phys. 36, 1775 (1965).
[8]R. S. Bird, Ph. D. thesis (Naval Postgraduate School, 1973) (unpublished).
[9]K. M. Brooks, M.S. thesis (Naval Postgraduate School, 1973) (unpublished).
[10]L. L. McKee, Ph. D. thesis (Naval Postgraduate School, 1972) (unpublished).
[11]D. Nagel (private communication).
[12]H. Carslaw and J. Jaeger, *Conduction of Heat in Solids* (Clarendon, Oxford, 1959), p. 112.
[13]G. W. Sutton and A. Sherman, *Engineering Magnetohydrodynamics* (McGraw-Hill, New York, 1965), p. 226.

APPENDIX B

REPRINT

"THE INFLUENCE OF HIGH ENERGY ELECTRON IRRADIATION ON THE 10.6 μm ABSORPTION OF MIXED KCl CRYSTALS"

By

T. J. Magee, N. Johnson, and J. Peng

(Physica Status Solidi (A) 30, 81 (1975))

The Influence of High Energy Electron Irradiation on the 10.6 μm Absorption of Mixed KCl Crystals[1)]

by

T. J. Magee, N. Johnson, and J. Peng[2)]

ABSTRACT

Polycrystalline potassium chloride crystals alloyed with either RbCl, KBr, or $EuCl_2$ have been irradiated with 1 MeV electrons at a dose rate of approximately 3.3×10^5 R/sec. Measurements of the 10.6 μm absorption coefficient after each exposure indicated that the radiation induced infrared absorption saturated rapidly as a function of increasing electron exposure time. Measurements of the visible and near-infrared absorption spectra indicated no positive correlation between F- absorption centers and increased infrared absorption at 10.6 μm. A definite correlation was found between the density of F- aggregate centers and the change in 10.6 μm absorption. In particular, it was found that the largest changes in 10.6 μm absorption can be associated with the presence of R-centers in the mixed crystals.

---

1) Research supported by AFOSR Contract No. F44620-73-C-0019

2) Post doctoral research fellow

Polykristalline Kaliumchloridkristalle wurden mit Beigaben von RbCl, KBr oder $EuCl_2$ hergestellt und mit 1 MeV Elektronen bestrahlt. Die Dosis betrug annähernd 3.3×10^5 R/sec. Messungen des Absorptionskoeffizienten bei 10.6 µm nach jeder Bestrahlung zeigten, dass die durch die Strahlung hervorgerufene Infrarotabsorption als eine Funktion zunehmender Elektronen bestrahlungsdauer sich sehr schnell einem Sättigungswert näherte. Messungen der Spektren im Sichtbaren und nahe-IR zeigten bei 10.6 µm keine positive Korrelation zwischen. F-Absorptions zentren und steigender Infrarotabsorption. Ein ausdrücklicher Zusammenhang fand sich zwischen der Dichte der F-Aggregatzentren und der Veränderung der Absorption bei 10.6 µm. Insbesondere stellte es sich heraus, dass die grössten Veränderungen der Absorption bei 10.6 µm mit der Gegenwart von R-Zentren in den Mischkristallen in Zusammenhang gebracht werden können.

1. Introduction

The development of high-power CO_2 infrared laser systems has provided the impetus for an increased number of investigations on the use of alkali halide materials for laser windows. Significant improvements have been reported both in terms of the processing of materials [1] and the understanding of the influence of structural defects on the infrared transmission characteristics. Ionizing radiation has been shown to increase the resolved flow stress in mixed KCl crystals [2] by introducing halogen interstitial clusters, [3] which strengthen the material for laser window applications. [4] However, reports on the alteration in the 10.6 μm absorption coefficient and the correlation with radiation-induced color centers have been limited.

In an earlier investigation [5] of KCl single crystals subjected to relatively high dose rate (10^6 R/sec) 1 MeV electron and (10^5 R/sec) x-ray irradiations, it was shown that the 10.6 μm absorption coefficient increased linearly as a function of dose with saturation occurring at doses $> 5 \times 10^7$ R. Subsequent experiments by Phillipi [6] on x-irradiated samples tended to confirm the previous results. Using lower dose rate (2.8×10^2 R/sec) gamma irradiation, Lipson et al. [7] recently reported that the change in the 10.6 μm absorption coefficient of undoped KCl could be associated with the presence of F-aggregate centers.

In all the previous studies, experiments were conducted on undoped single crystal or polycrystalline KCl. There have been no published reports on the influence of high dose-rate electron irradiation on the alteration of the 10.6 μm absorption coefficient of mixed or doped KCl

samples. In this study, we have concentrated on the effects of 1 MeV electron irradiation on polycrystalline KCl-KBr, KCl-RbCl and KCl-$EuCl_2$ alloyed crystals. This paper reports on the dose dependence of the induced change in infrared absorption and the correlation with F- and F-aggregate centers after electron irradiation and subsequent bleaching with F- band light.

2. Experimental Procedure

Samples used in this study were processed by the Honeywell Corporation. The samples were prepared by a hot forging technique [8] and included: 1) KCl alloyed with 5 mol% KBr, 2) KCl alloyed with 5 mol% RbCl, and 3) KCl alloyed with 0.05 mol % $EuCl_2$. Using conventional CO_2 laser calorimetry techniques, [9,10] we determined that the 10.6 μm absorption coefficients averaged $\simeq 8 \times 10^{-4}$ cm^{-1}.

Samples were prepared for irradiation in the form of parallelopipeds of 1 cm and 0.14 cm thickness, a 1.5 cm^2 surface area, and subsequently exposed to 1 MeV electrons at a dose rate of 3.3×10^5 R/sec. After each exposure the 10.6 μm absorption coefficient was determined by laser calorimetry and the absorption spectra monitored in the visible and near-infrared regions for all samples with a Beckman DK-2 spectrophotometer. The maximum depth of visible coloration in these samples was determined to be $\simeq$ 1.3 mm.

To provide suitable control data and to assure that the 10.6 μm measurements were indicative of a dose-dependent change in infrared absorption, a separate set of samples was exposed to the same environmental conditions but not subjected to electron irradiation. In all

cases there was no significant change in the 10.6 μm absorption coefficient of the control samples. In additional control experiments, selected samples were repolished after electron irradiation. The 10.6 μm absorption coefficients measured after repolishing remained essentially unchanged from the post-irradiation values.

Bleaching experiments were conducted on a number of the irradiated samples by using an Hg-lamp source and a Bausch and Lomb monochromator. The samples were exposed to 0.55 μm light for periods ranging from 1 sec to 600 sec.

3. Results

Figure 1 shows a typical optical absorption curve obtained on KCl-RbCl illustrating the presence of F and M-centers. All samples examined showed either an extremely low density or an apparent absence of R and N centers following electron irradiation. Figures 2 to 4 show the F- and M-center peak absorption coefficients as a function of exposure time in a 1 MeV electron beam at a dose rate of 3.3×10^5 R/sec for polycrystalline KCl-KBr, KCl-RbCl, and KCl-$EuCl_2$ samples, respectively. Also shown is the induced change in the 10.6 μm absorption coefficients, $\Delta R_{10.6}$, as a function of exposure time.

Comparing Figures 2 to 4, we observe that the behavior of the F-center absorption as a function of dose for all the samples is qualitatively similar. In the lower dose ranges, the absorption increases linearly, with apparent saturation occurring at doses $> 3 \times 10^6$ R. Correspondingly, the M-center absorption and the change in 10.6 μm

absorption exhibit a similar dose dependence. In agreement with previous studies [2,11,12] the coloration rate for F- and M-centers in the mixed crystals was found to be considerably lower than that for undoped KCl. In contrast to the results obtained on electron irradiated single crystal (undoped) KCl [5] or low dose-rate gamma irradiated polycrystalline (undoped) KCl, [7] $\Delta\beta_{10.6}$ saturates rapidly with increasing electron-beam exposure time for mixed KCl crystals.

F-center densities, n_F, and M-center densities, n_M, were calculated with the relations, $n_F(cm^{-3}) = 8.7 \times 10^{15}\ \beta_F W_F$, and $n_M(cm^{-3}) = 1.9 \times 10^{16}\ \beta_M W_M$, where β_F, β_M are the F- and M-center peak optical absorption coefficients in cm^{-1}, respectively, and W_F, W_M, the corresponding widths in eV of the absorption peaks at half maximum amplitudes. Since the oscillator strengths are not known exactly for these crystals, the calculated densities represent at best an approximation, but serve as an appropriate basis of comparison between samples.

From the data obtained it was found that the change in absorption at 10.6 μm could not be adequately related to the F-center density. Similar results were reported by Lipson et al. [7] on undoped gamma-irradiated KCl. In Figure 5, the change in $\Delta\beta_{10.6}$ as a function of increasing M-center density indicates that the induced changein 10.6 μm absorption reaches a saturation limit at relatively low M-center densities. The KCl-$EuCl_2$ samples exhibit the smallest change in 10.6 μm absorption, approaching a saturation value of $\Delta\beta_{10.6} \simeq 9 \times 10^{-4}\ cm^{-1}$ for M-center densities $> 1.5 \times 10^{16}\ cm^{-3}$. In all cases, the mixed crystals show an initial rapid change in 10.6 μm absorption as a function of M-center density, followed by a region of relative saturation. For undoped KCl crystals, the change in 10.6 μm absorption exhibits a linear dependence

on M-center concentration over the same density range. [5,7]

The results suggest that the increase in 10.6 μm absorption can be related to the same mechanism causing absorption in F- or F-aggregate bands, or to the presence of Cl interstitial clusters introduced by the irradiation. In addition, it is possible that F- or F-aggregate bands having a Lorentzian line shape might contribute to the 10.6 μm absorption. The presence of interstitial clusters has been effectively eliminated as a mechanism for increasing the infrared absorption. [7] Assuming a Lorentzian curve of the form:

$$\beta(\lambda) = \frac{b}{\pi} \quad \frac{1}{1 + C^2 \left(1/\lambda - \frac{1}{\lambda_m}\right)^2}$$

where λ_m is the wavelength at the peak of the absorption band, calculations based on the absorption data predicted a greater absorption than the experimentally determined 10.6 μm absorption. Furthermore, the amplitudes of the F- and M-center absorption bands in the crystals examined in this study were often comparable, and should exhibit, according to the previous equation, comparable absorptions at 10.6 μm, in disagreement with experimental data. Hence, Lorentzian band shape tailing of absorption peaks from F- or F-aggregate centers cannot satisfactorily account for the increased infrared absorption in KCl.

To obtain further information on the correlation between F- and F-aggregate centers and the increase in the 10.6 μm absorption coefficient, and to test the hypothesis of Lipson et al. that concentrations of F-aggregate centers can be associated with changes in the infrared absorption, a number of the electron irradiated samples were bleached

with 0.55 μm light at nominal levels of 500 $\mu W/cm^2$ for periods between 1 sec to 600 sec. Subsequently, the 10.6 μm absorption coefficient was measured and the visible and near-infrared absorption spectra recorded. In all cases, R- and N-centers appeared and increased in concentration during the early stages of bleaching. Figures 6 and 7 illustrate the results obtained for a KCl-RbCl sample. Figure 6 shows that the F-center absorption decreases continuously as a function of bleach time, while the M-center absorption increases rapidly, but decreases after a 30 sec bleach time. In like manner, the R_2-center absorption increases, eventually decreasing for bleach times exceeding 120 sec. Measurements obtained on all samples indicated a continual decrease in F- and F-aggregate center absorption for exposure times between 140 sec. and 600 seconds. In Figure 7 the 10.6 μm absorption increases for bleach times < 120 sec., but decreases thereafter.

A comparison of the data in Figures 6 and 7 indicates that the increase in the 10.6 μm absorption shows no positive correlation with the presence of F-centers, since the F-center absorption coefficient is decreasing over the range in which the 10.6 μm absorption coefficient is increasing. In contrast, the F-aggregate center absorptions are increasing when the infrared absorption is increasing. Changes in the M-center absorption coefficient cannot alone explain the large increase in $\Delta\beta_{10.6}$ observed in Figure 7 since it has been shown (Figure 3) that relative changes in M-center absorption of the magnitude observed in the bleached samples are correlated with only small changes in $\Delta\beta_{10.6}$, while the increase and decrease of the R_2-center absorption coefficient show a direct correlation with the behavior of the 10.6 μm absorption.

The data support the general contention of Lipson et al. that the change in the 10.6 μm absorption can be correlated with the presence of F-aggregate centers rather than F-centers. More specifically, the present study indicates for electron-irradiated, mixed KCl crystals that the change in 10.6 μm absorption saturates with increasing M-center density. Both R and N centers appear after bleaching and can be correlated with changes in the 10.6 μm absorption coefficient. However, it is the R-center that appears to be the F-aggregate center associated with large changes in infrared absorption.

4. Conclusions

In this study we have shown that the F- and M-center coloration rate for mixed KCl crystals irradiated with 1 MeV electrons is lower than that for comparably irradiated pure KCl samples, in agreement with previous authors. [2,11,12] It has also been shown that the alteration in 10.6 μm absorption can be correlated with increasing F-aggregate center concentrations. Although the presence of M-centers can be correlated with increases in 10.6 μm absorptions, the present study indicates that the presence of R-centers exerts the most dominant influence on the infrared absorption in mixed KCl crystals.

The authors would like to acknowledge the assistance of R. Goldberg and J. Fenter of the Air Force Materials Laboratory in supplying mixed KCl samples for these investigations.

References

[1] S. D. Allen, M. Braunstein, C. Giuliano, and V. Wang, in Proc. Symposium on Laser Induced Damage in Optical Materials, A. J. Glass and A. H. Guenther, eds., National Bureau of Standards Special Publ. No. 414, December 1974 (p. 66).

[2] J. R. Hopkins, J. J. Martin, and J. Larkin, J. Appl. Phys. 45, 2804 (1974).

[3] L. W. Hobbs, A. E. Hughes, and D. Pooley, Proc. Roy. Soc. (London) A332, 167 (1973).

[4] J. J. Martin, C. T. Butler, J. R. Hopkins, and W. A. Sibley, in Proc. Third Conference on High Power Infrared Laser Window Materials, C. A. Pitha, A. Armington, and H. Posen, eds., U.S. Air Force Cambridge Research Laboratories Tech. Rpt. TR-74-0085 (11), Bedford, Massachusetts 1974 (p. 547).

[5] T. J. Magee, Stanford Research Institute Technical Report No. 2266-1, Menlo Park, California (1972).

[6] C. Phillipi, (unpublished data), U.S. Air Force Materials Laboratory, Dayton, Ohio (1973).

[7] H. G. Lipson, A. Kahan, P. Ligor, and J. J. Martin, in Proc. Fourth Conference on Infrared Laser Window Materials, C. R. Andrews and C. L. Strecker, eds., U.S. Air Force Materials Laboratory Special Report, Wright-Patterson AFB, Ohio 1975 (p. 589).

[8] W. B. Harrison, G. O. Hendrickson, and J. E. Starling, in Proc. Third Conference on High Power Infrared Laser Window Materials, C. A. Pitha, A. Armington, and H. Posen, eds., U.S. Air Force Cambridge Research Laboratories Tech. Rpt. TR-74-0085 (11), Bedford, Massachusetts 1974 (p. 615).

[9] H. G. Lipson, L. H. Skolnik, and D. L. Stierwalt, in Proc. Third Conference on High Power Infrared Laser Window Materials, C. A. Pitha and B. Bendow, eds., U.S. Air Force Cambridge Research Laboratories Tech. Rpt. TR-74-0085 (1), Bedford, Massachusetts 1974 (p. 337).

[10] L. H. Skolnik, A. Hordvik, and A. Kahan, Appl. Phys. Letters 23, 477 (1973).

[11] J. Arends, H. W. Den Hartog, and A. J. Dekker, phys. stat. sol. 10, 105 (1965).

[12] P. P. Still and D. Pooley, phys. stat. sol. 32, K147 (1969).

List of Figures

Fig. 1. Absorption spectra of a KCl-RbCl crystal following a 4 second electron irradiation. Both the irradiation and the measurement were performed at 25°C. The electron energy was 1 MeV and the dose rate, 3.3×10^5 R/sec.

Fig. 2. β_F, β_M, and $\Delta\beta_{10.6}$ as a function of electron exposure time at 25°C in KCl-KBr samples. The scales on the right show the absorption constants determined at the peak position of the F band (β_F) and the M-band (β_M). The scale on the left shows the change in the 10.6 μm absorption coefficient, $\Delta\beta_{10.6} = (\beta_{10.6})_f - (\beta_{10.6})_o$, where $(\beta_{10.6})_f$ represents the value of the 10.6 μm absorption coefficient after irradiation and $(\beta_{10.6})_o$, the value for the unirradiated sample.

Fig. 3. β_F, β_M, and $\Delta\beta_{10.6}$ as a function of electron exposure time at 25°C in KCl-RbCl samples. Scales on the right refer to values of the absorption coefficients, β_F and β_M. The scale on the left refers to the change in the 10.6 μm absorption coefficient, $\Delta\beta_{10.6}$.

Fig. 4. β_F, β_M, and $\Delta\beta_{10.6}$ as a function of electron exposure time at 25°C in KCl-$EuCl_2$ sample. Scales on the right refer to values of the absorption coefficients, β_F and β_M. The scale on the left refers to the change in the 10.6 μm absorption coefficients, $\Delta\beta_{10.6}$.

Fig. 5. Change in the 10.6 μm absorption coefficient, $\Delta\beta_{10.6}$, as a function of M-center density in mixed KCl crystals. $\Delta\beta_{10.6}$ for KCl-$EuCl_2$ samples is referred to the scale at the right; $\Delta\beta_{10.6}$ for other samples is referred to the scale at the left. ● - KCl-KBr; ■ - KCl-RbCl; ▼ - KCl-$EuCl_2$.

Fig. 6. β_F, β_M, and β_{R_2}, as a function of bleach time for an electron irradiated KCl-RbCl sample. After electron irradiation the sample was exposed to 0.55 μm light for variable periods. All measurements were obtained at 25°C. Values of β_M and β_{R_2} are referred to the scale at the left and β_F, to the scale at the right. ■ - β_M; ▲ - β_{R_2}; ● - β_F.

Fig. 7. Change in $\Delta\beta_{10.6}$ as a function of bleach time for an electron irradiated KCl-RbCl sample.

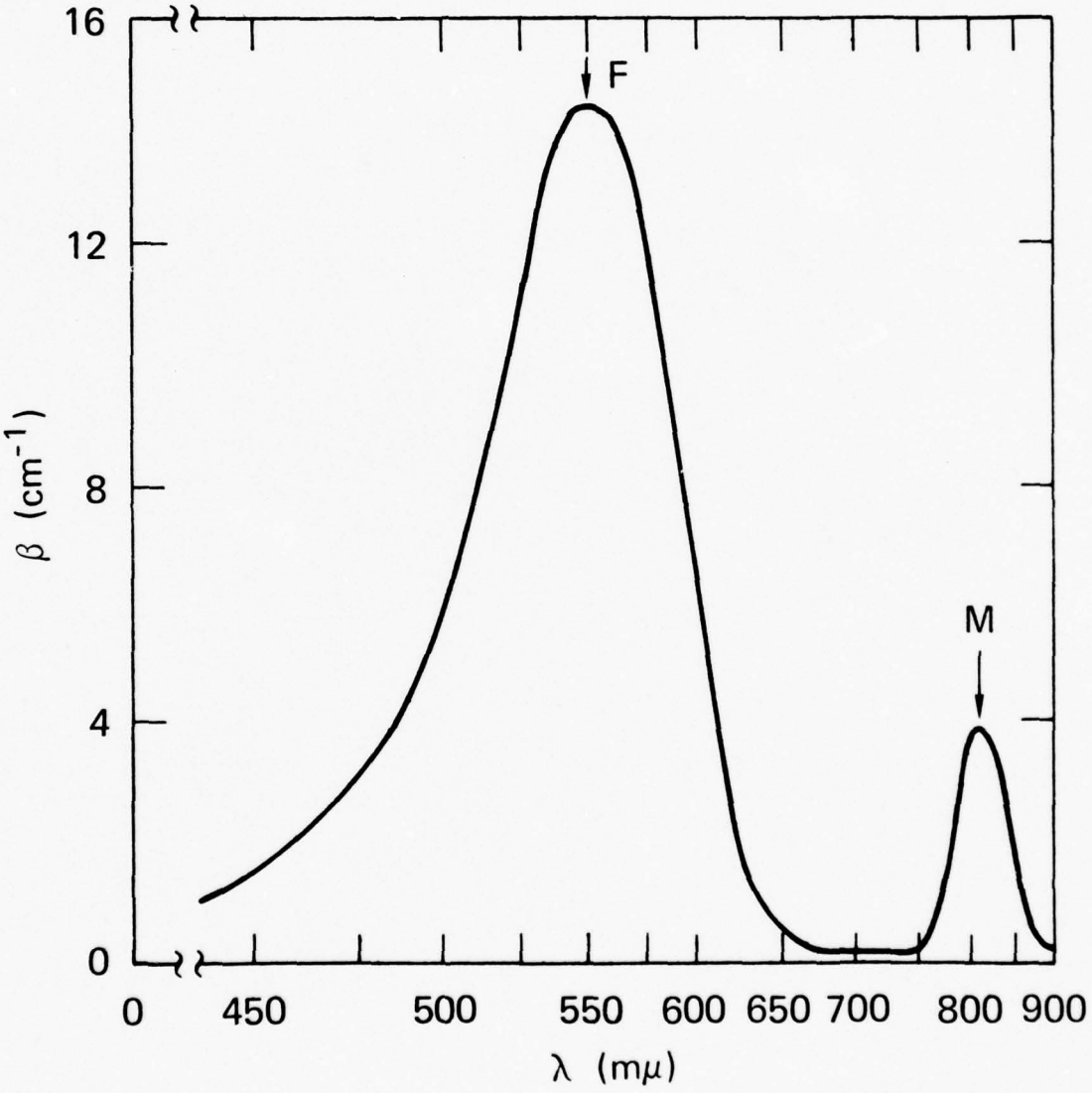

MA-319522-25

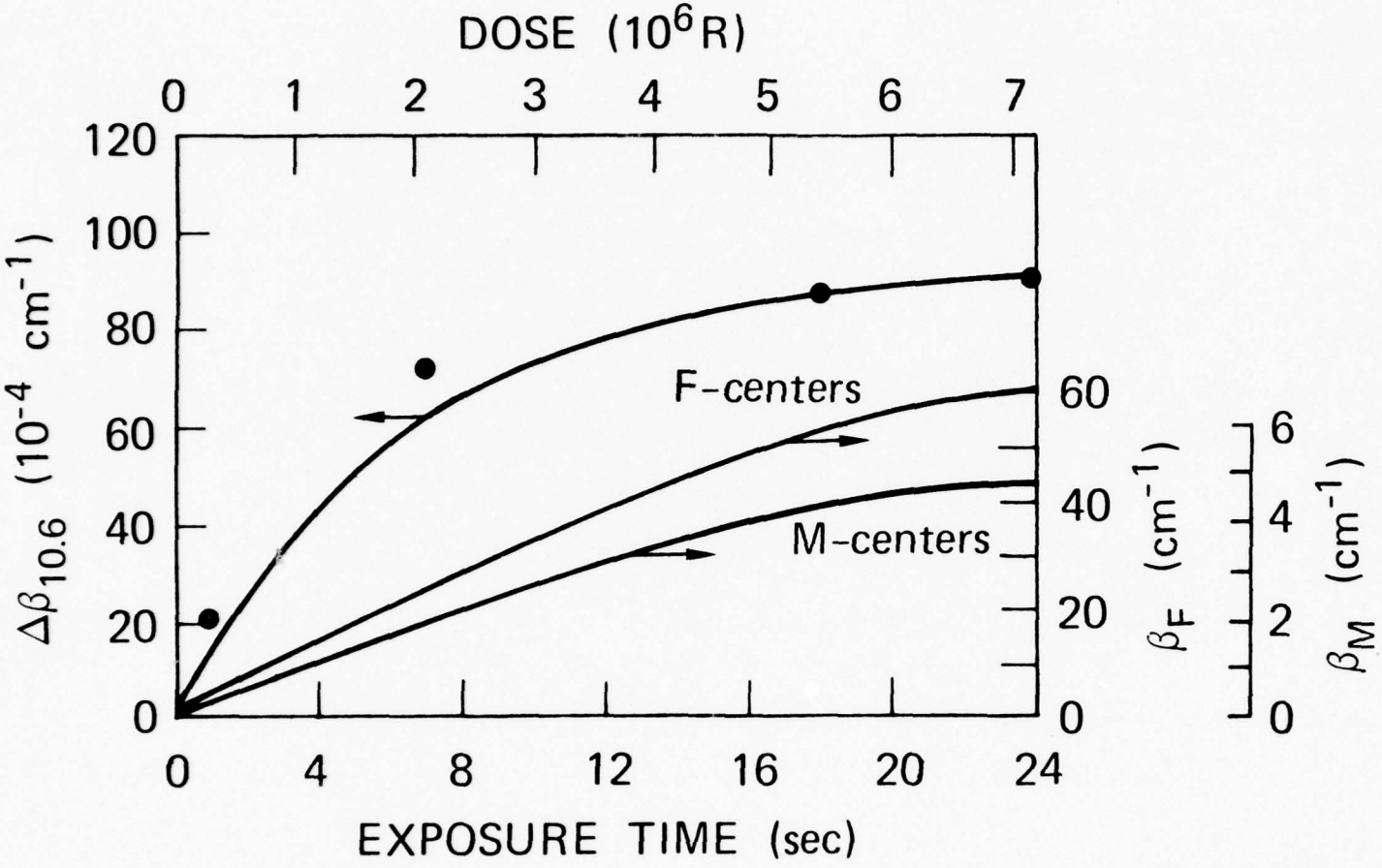
DOSE (10^6R)
0 1 2 3 4 5 6 7
120
100
80
60
40
20
0
$\Delta\beta_{10.6}$ (10^{-4} cm^{-1})
F-centers
M-centers
60
40
20
0
β_F (cm^{-1})
6
4
2
0
β_M (cm^{-1})
0 4 8 12 16 20 24
EXPOSURE TIME (sec)

MA-319522-23

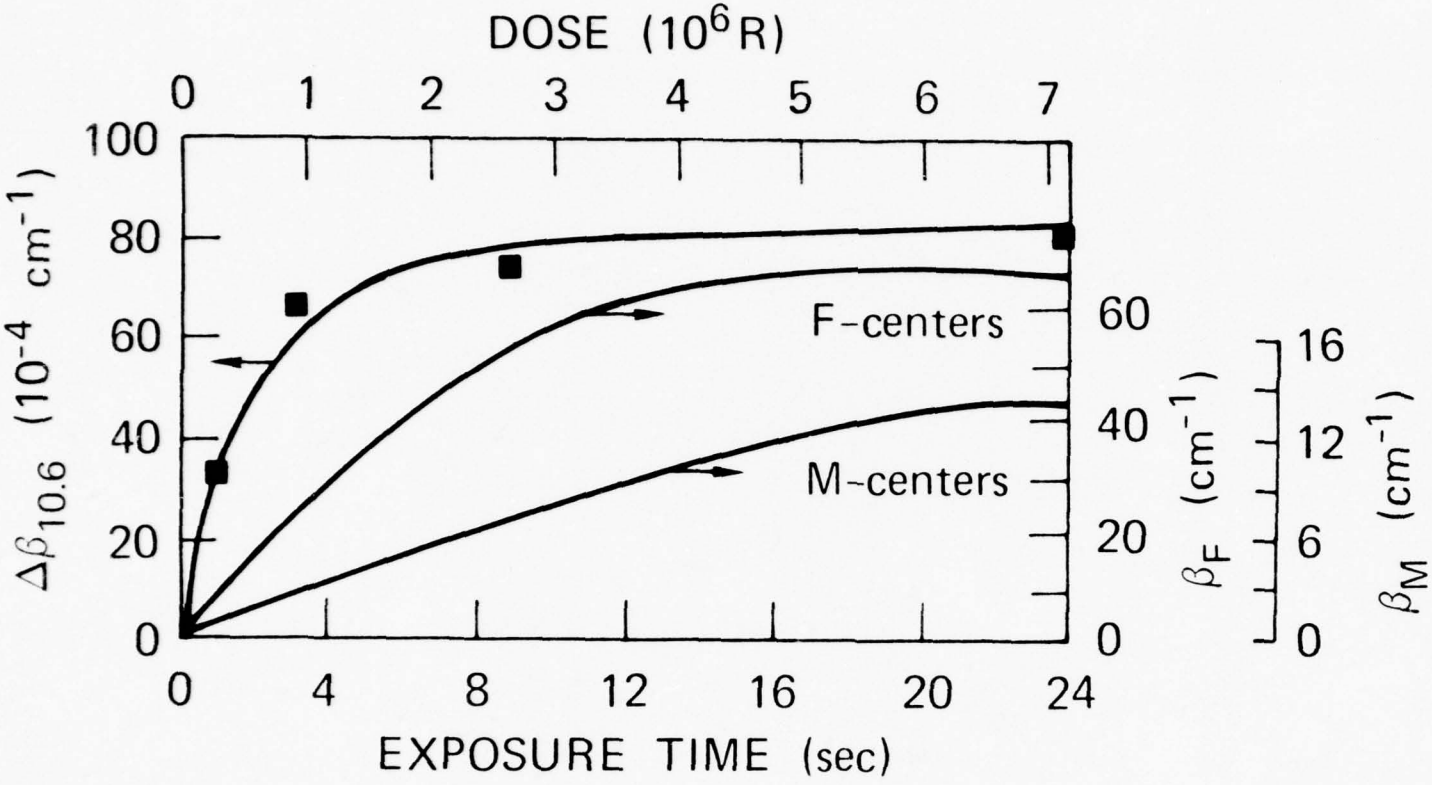
DOSE (10^6R)
0 1 2 3 4 5 6 7
100
80
60
40
20
0
$\Delta\beta_{10.6}$ (10^{-4} cm^{-1})
F-centers
M-centers
60
40
20
0
16
12
6
0
β_F (cm^{-1})
β_M (cm^{-1})
0 4 8 12 16 20 24
EXPOSURE TIME (sec)

MA-319522-22

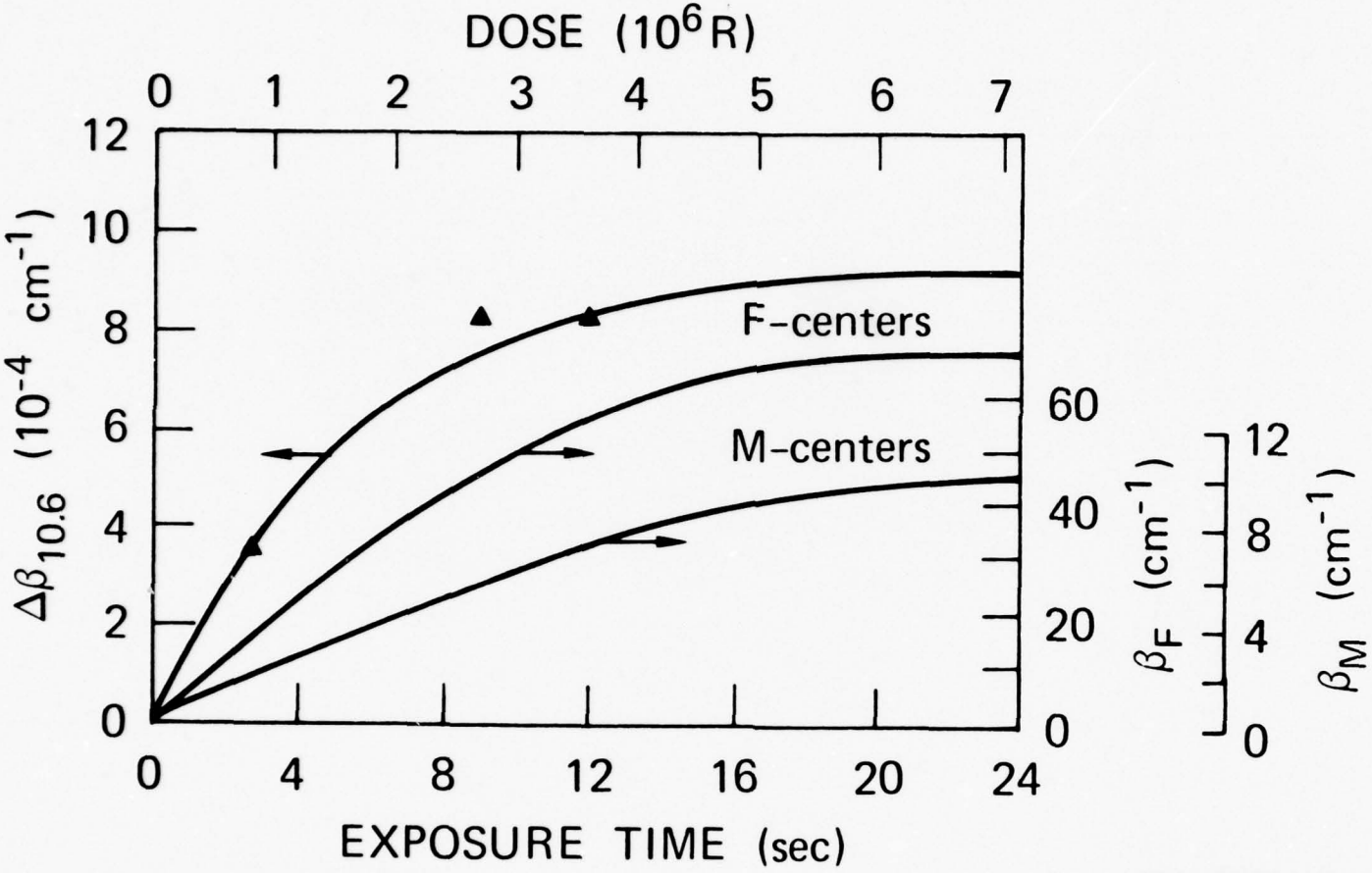
DOSE (10^6 R)
0 1 2 3 4 5 6 7
12 10 8 6 4 2 0
$\Delta\beta_{10.6}$ (10^{-4} cm^{-1})
F-centers
M-centers
60 40 20 0
12 8 4 0
β_F (cm^{-1})
β_M (cm^{-1})
0 4 8 12 16 20 24
EXPOSURE TIME (sec)

MA-2266-13A

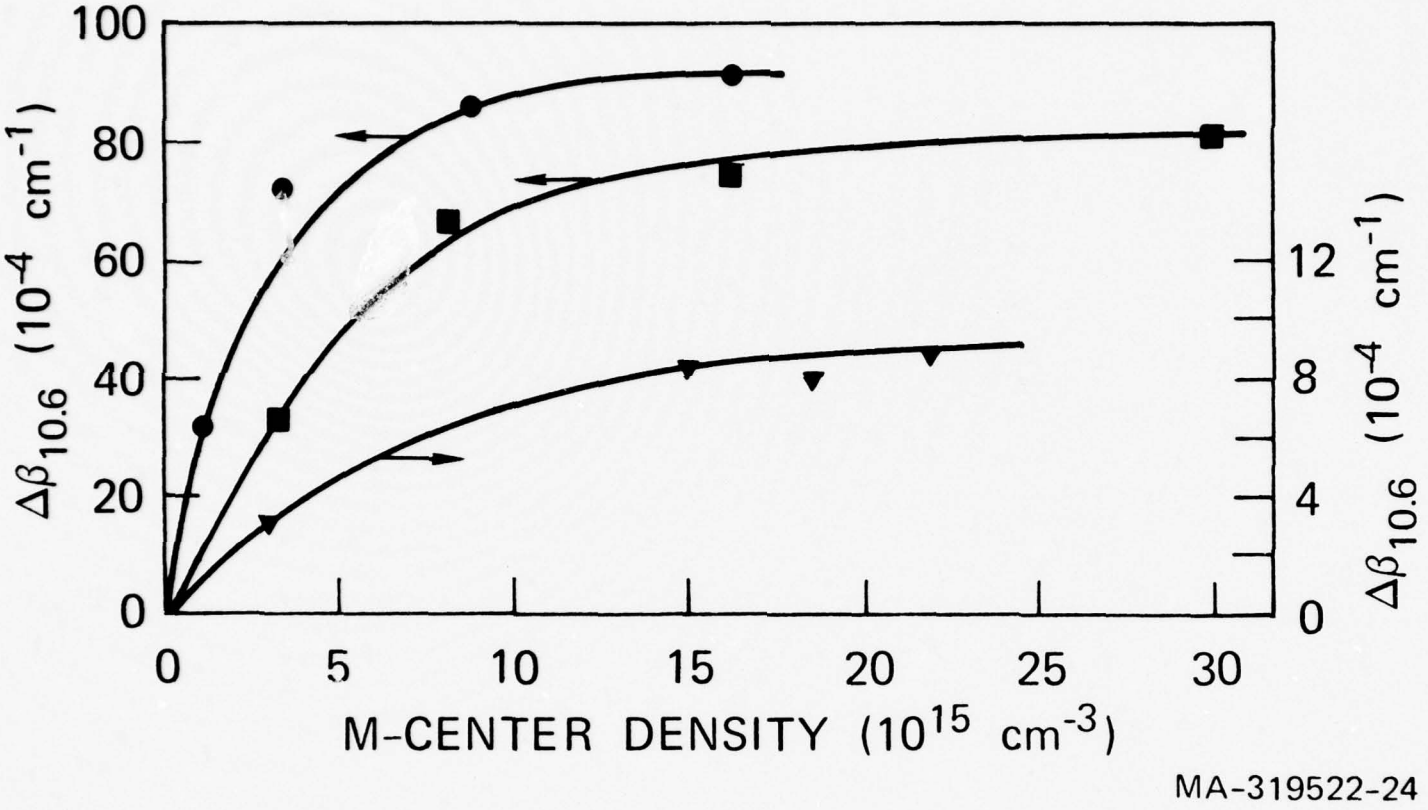
100
80
60
40
20
0
$\Delta\beta_{10.6}$ (10^{-4} cm^{-1})
0
5
10
15
20
25
30
M-CENTER DENSITY (10^{15} cm^{-3})
12
8
4
0
$\Delta\beta_{10.6}$ (10^{-4} cm^{-1})

MA-319522-24

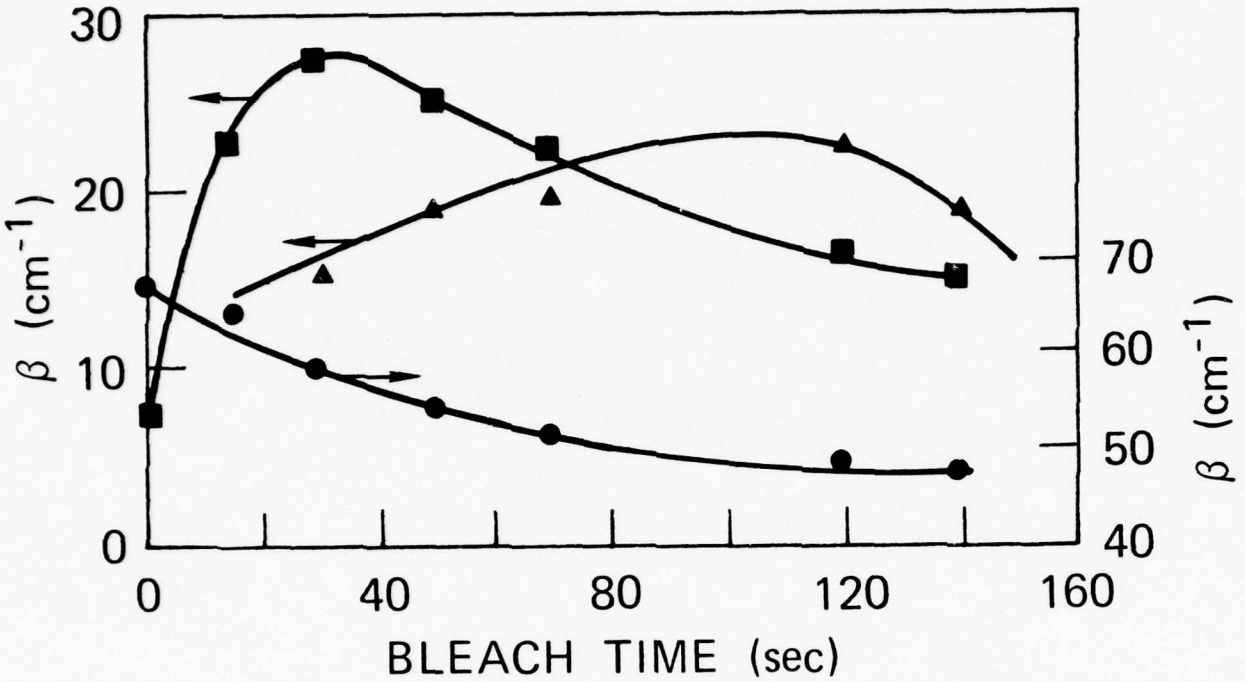

MA-319522-20

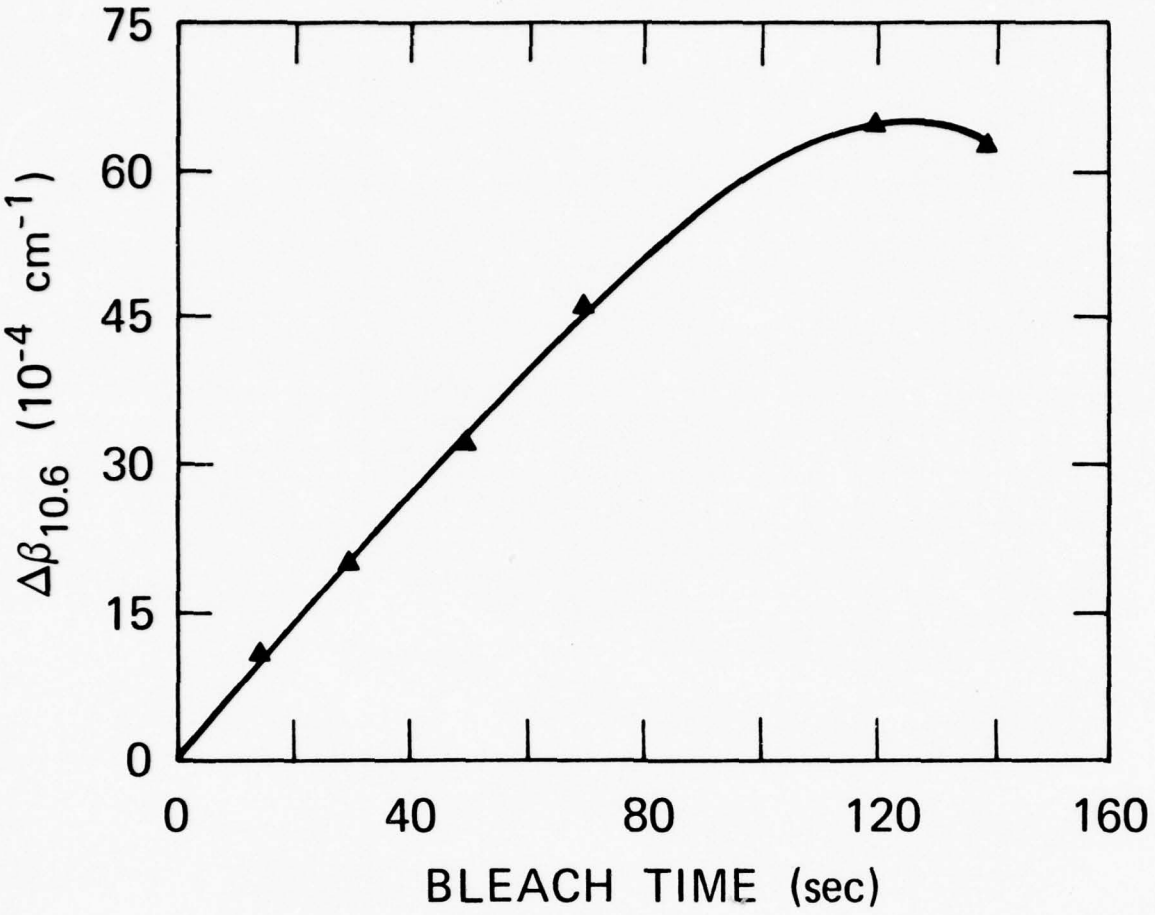
75
60
45
30
15
0
$\Delta\beta_{10.6}$ (10^{-4} cm^{-1})
0
40
80
120
160
BLEACH TIME (sec)

MA-319522-21

APPENDIX C

PREPRINT

"THE EFFECT OF ILLUMINATION ON THE 10.6 μm ABSORPTION COEFFICIENT OF ELECTRON IRRADIATED SINGLE CRYSTAL KCL"

By

T. J. Magee, N. M. Johnson, and J. Peng

(Accepted for publication in Physica Status Solidi (A) 33, 415 1976)

THE EFFECT OF ILLUMINATION ON THE 10.6 μm ABSORPTION COEFFICIENT OF ELECTRON IRRADIATED SINGLE CRYSTAL KCl[1)]

By

T. J. Magee, N. M. Johnson, and J. Peng[2)]
Stanford Research Institute
Menlo Park, California 94025

ABSTRACT

Single crystal KCl samples were irradiated with 1 MeV electrons at a dose rate of approximately 3.3×10^5 R/sec while being simultaneously illuminated with F-band light. Measurements of the 10.6 μm absorption coefficient after each exposure indicated that the induced change in infrared absorption was significantly higher for samples exposed to F-light during irradiation compared with that observed for samples irradiated in the dark. The increase noted in the 10.6 μm absorption coefficient has been shown to be correlated with increasing densities of M-centers. Bleaching experiments performed after irradiation confirmed the fact that the largest changes in 10.6 μm absorption could be associated with the presence of M-centers. Other F-aggregate centers introduced during bleaching exerted a small but measurable influence on the absorption at 10.6 μm.

---

1) Research supported by AFOSR Contract No. F44620-73-C-0019.

2) Postdoctoral research fellow.

1. INTRODUCTION

In a recent investigation [1] of polycrystalline KCl-KBr, KCl-RbCl, and KCl-$EuCl_2$ alloyed samples exposed to high dose rate (3.3×10^5 R/sec) 1 MeV electron irradiation, it was shown that the change in the 10.6 μm absorption coefficient could be correlated with the presence of F-aggregate centers. Subsequent bleaching of the samples after electron irradiation indicated that R-centers exerted the most prominent effect on the infrared absorption coefficient. In studies of polycrystalline (undoped) KCl samples exposed to relatively low dose rate (2.8×10^2 R/sec) gamma irradiation, Lipson et al. [2] also found that the increase in infrared absorption at 10.6 μm could be associated with concentrations of F-aggregate centers. However, each of the previous studies has been concerned with alterations in the infrared absorption of irradiated, mixed or undoped polycrystalline KCl. No reports have been published on comparable studies of irradiated single crystal (undoped) KCl or on the effect of simultaneous electron irradiation and F-band illumination on the infrared absorption of single crystal samples. The purpose of this study is to extend the previous results and to determine the changes in 10.6 μm absorption and F-aggregate center concentrations for KCl single crystal samples exposed to F-band illumination both during and subsequent to high energy electron beam irradiation.

2. EXPERIMENTAL PROCEDURE

Samples used in these experiments were obtained from the Harshaw Chemical Company. Specimens were prepared for irradiation in the form of parallelopipeds of 1 cm and 0.14 cm thickness and 0.75 to 1.5 cm^2 surface area. After polishing the sample surfaces [3], conventional CO_2 laser calorimetry techniques [1,4] were used to measure the 10.6 μm absorption coefficients. Average absorption coefficients of the as-received samples were measured in the range, 4×10^{-4} cm^{-1} to 6×10^{-4} cm^{-1}.

Samples were irradiated at room temperature with 1 MeV electrons at a dose rate of 3.3×10^5 R/sec. A Hg lamp and a Bausch and Lomb monochromator were used for simultaneous F-band (0.55 μm) illumination. An electromechanical shutter, switched in sequence with the electron beam shutter, provided control of F-light exposure during electron irradiation. After each irradiation, the 10.6 μm absorption coefficient was determined for all samples by laser calorimetry and the absorption spectra were monitored in the visible and near-infrared regions with a Beckman DK-2 spectrophotometer.

Post-irradiation bleaching experiments were also conducted on a number of samples by exposing them to F-light for periods ranging from 1 sec to 600 sec.

3. *RESULTS*

Figure 1 shows the F- and M-center peak absorption coefficients, β_F and β_M, as a function of exposure time in a 1 MeV electron beam at a dose rate of 3.3×10^5 R/sec for single crystal KCl samples irradiated in the dark and in the presence of F-band illumination. The induced change in the 10.6 μm absorption coefficients, $\Delta\beta_{10.6}$, under the two exposure conditions is also shown for comparison.

The data indicate that the F-center absorption coefficient exhibits essentially the same qualitative dose dependence for samples irradiated either in the dark or in the presence of F-illumination. However, in all cases, there was a slight reduction in β_F for samples irradiated simultaneously with F-light. In contrast, we observe that the M-center absorption coefficient as a function of dose is consistently higher for the illuminated samples than for those irradiated in the dark.

The $\Delta\beta_{10.6}$ curves in Fig. 1 exhibit an initial rapid change as a function of exposure time followed by an approximately linear region for doses > 10^6 R. Apparent saturation in the $\Delta\beta_{10.6}$ curve has been previously observed [5] for KCl samples electron irradiated in the dark to dose levels > 10^7 R. For the dose range considered in these experiments, $\Delta\beta_{10.6}$ did not reach saturation and was always larger for the illuminated samples than for those irradiated in the dark.

The F-center densities, n_F, and M-center densities, n_m, were calculated using the relations: $n_F(cm^{-3}) = 8.7 \times 10^{15}\ \beta_F W_F$, and $n_m(cm^{-3}) = 1.9 \times 10^{16}\ \beta_M W_M$, where $\beta_F \beta_M$ are the F- and M-center peak optical absorption coefficients in cm^{-1}, respectively, and W_F, W_M, are the corresponding width in eV of the absorption peaks at half maximum amplitudes.

In agreement with previous investigations [1,2] it was found that the change in 10.6 μm absorption could not be adequately correlated with F-center concentration. Figure 2 shows the change in $\Delta\beta_{10.6}$ as a function of M-center density for samples irradiated both in the dark and in the presence of F-illumination. The results indicate that under both exposure conditions the change in 10.6 μm absorption increases linearly as a function of M-center concentration.

Comparison of the data in Figs. 1 and 2 shows that the net effect of simultaneous electron irradiation and F-illumination is to increase the concentration of M-centers relative to that observed for samples irradiated in the dark to similar dose levels. The increase in M-center concentration can subsequently be related to changes in $\Delta\beta_{10.6}$. Since the optical absorption spectra of all samples after irradiation indicated an apparent absence or relatively small concentration of N- and R-centers, it can be assumed that the observed changes in $\Delta\beta_{10.6}$ are strongly correlated with the presence of M-centers and that contributions to $\Delta\beta_{10.6}$ by other F-aggregate centers are small.

Samples electron-irradiated under both exposure conditions were subsequently illuminated with F-band light for periods up to 600 sec to obtain additional information on the correlation between $\Delta\beta_{10.6}$ and F-aggregate center concentrations. Changes in β_F, β_M, β_{R_2} and $\Delta\beta_{10.6}$ were measured as a function of bleach time, and the results are shown in Figs. 3-5. In Figs. 3 and 4 β_F continuously decreases as a function of bleach time, whereas β_M and β_{R_2} show a corresponding increase followed by a continual decrease for bleach times up to 600 sec. For both samples the concentration of M-centers increases rapidly as a function of time, reaching a maximum at bleach times between 25 and 30 seconds and decreasing thereafter. In Fig. 5 the change in $\Delta\beta_{10.6}$ correspondingly exhibits a maximum in the same time period and continually decreases for bleach times > 30 sec.

Comparing the data shown in Figs. 3 and 4 with those of Fig. 5, we observe that the behavior of the $\Delta\beta_{10.6}$ curves can be directly correlated with changes in M-center concentration. However, the presence of increasing concentrations of R- and N-centers at bleach times > 30 sec and the extended tails of the $\Delta\beta_{10.6}$ bleach curves in Fig. 5 indicate that the presence of F-aggregate centers other than the M-center also contribute to the change in $\Delta\beta_{10.6}$, but to a lesser extent. In particular, the R_2-center increases in concentration for times < 140 sec., but decreases for longer F-light exposures. In all cases,for samples subjected to extremely long periods of bleaching, the eventual removal of F-aggregate centers is correlated with a recovery of the 10.6 μm absorption coefficient to its approximate pre-irradiation value.

The results on single crystal undoped KCl indicate that the change in 10.6 μm absorption can be strongly correlated with changes in M-center concentration. In contrast, the previous experiments [1] on polycrystalline

mixed KCl crystals indicated that $\Delta\beta_{10.6}$ saturated with increasing M-center densities and that the R-center was more influential in altering the infrared absorption. In both cases, however, the change in the 10.6 μm absorption was shown to be related to the presence of F-aggregate centers rather than F-centers.

4. CONCLUSIONS

In this study we have shown that simultaneously exposing single crystal KCl samples to F-band illumination and high energy electron irradiation causes a significant increase in the magnitude of the 10.6 μm absorption coefficient when compared with that obtained for samples irradiated in the dark. The observed increase has been shown to be proportional to the increase in F-aggregate center density. In separate bleaching experiments performed after electron irradiation, we have shown that the M-center exerts the most noticeable effect on the 10.6 μm absorption. The presence of R- and N-centers, although having a smaller influence on the infrared absorption, has been shown to be responsible for the extended recovery behavior of the 10.6 μm absorption coefficient of irradiated samples during long term exposure to F-illumination.

REFERENCES

[1] T. J. Magee, N. Johnson, and J. Peng, phys. stat. sol. 26 (1975).

[2] H. G. Lipson, P. Ligor, A. Kahan, and J. J. Martin, Bull. Amer. Phys. Soc. (Ser. 11) 20, 377 (1975).

[3] S. D. Allen, M. Braunstein, C. Giuliano, and V. Wang, "Laser Induced Damage in Optical Materials," Nat'l. Bur. Standards Spec. Pub. No. 414, Washington, D.C. (1974) p. 66.

[4] L. H. Skolnik, A. Hordvik, and A. Kahan, Appl. Phys. Letters 23, 477 (1973).

[5] T. J. Magee, Stanford Research Institute Technical Report No. 2266-1 Menlo Park, California (1972).

LIST OF FIGURES

1. β_F, β_M and $\Delta\beta_{10.6}$ as a function of electron exposure time at 25°C for single crystal KCl samples irradiated in the dark and in the presence of F-band illumination. The scales on the right refer to the value of the absorption constants determined at the peak position of the F-band (β_F) and M-band (β_M). The scale on the left shows the change in the 10.6 μm absorption coefficient $\Delta\beta_{10.6} = (\beta_{10.6})_f - (\beta_{10.6})_o$, where $(\beta_{10.6})_f$ represents the value of the absorption coefficient after irradiation and $(\beta_{10.6})_o$ represents the value for the unirradiated sample ■ - $\Delta\beta_{10.6}$ for samples illuminated with F-light during irradiation; ▲ - $\Delta\beta_{10.6}$ for sample irradiated in dark; -●- β_F for sample illuminated with F-light during electron irradiation; ▬▬ -β_M for samples illuminated with F-light during electron irradiation; unbroken lines represent corresponding values of β_F and β_M for samples irradiated in the dark.
2. $\Delta\beta_{10.6}$ as a function of M-center density in single crystal KCl samples. ▲ - samples irradiated in the dark; ■ - samples illuminated with F-light during electron irradiation.
3. β_F, β_M, and β_{R_2}, as a function of bleach time for an electron irradiated KCl sample. The sample was subjected to simultaneous electron beam irradiation and F-band illumination for a period of 4 sec. and subsequently bleached with 0.55 μm light for variable periods. All measurements were obtained at 25°C. Values of β_M and β_{R_2} are referred to the scales at the right and β_F to the scale at the left. ▲ - β_M, ■ - β_{R_2}, ● - β_F.

4. β_F, β_M, and β_{R_2} as a function of bleach time for an electron-irradiated KCl sample. The sample was subjected to electron beam irradiation in the dark for a period of 2 sec. and subsequently bleached with 0.55 μm light for variable periods. All measurements were obtained at 25°C. Values of β_M and β_{R_2} are referred to the scales at the right and β_F to the scale at the left. ▲ - β_M ■ - β_{R_2}, ● - β_F.

5. Change in $\Delta\beta_{10.6}$ as a function of bleach time. $\Delta\beta_{10.6}$ represents the difference between $\beta_{10.6}$ measured before irradiation and $\beta_{10.6}$ after irradiation and bleach. ▲ - $\Delta\beta_{10.6}$ for sample in Fig. 3; ■ - $\Delta\beta_{10.6}$ for sample in Fig. 4.

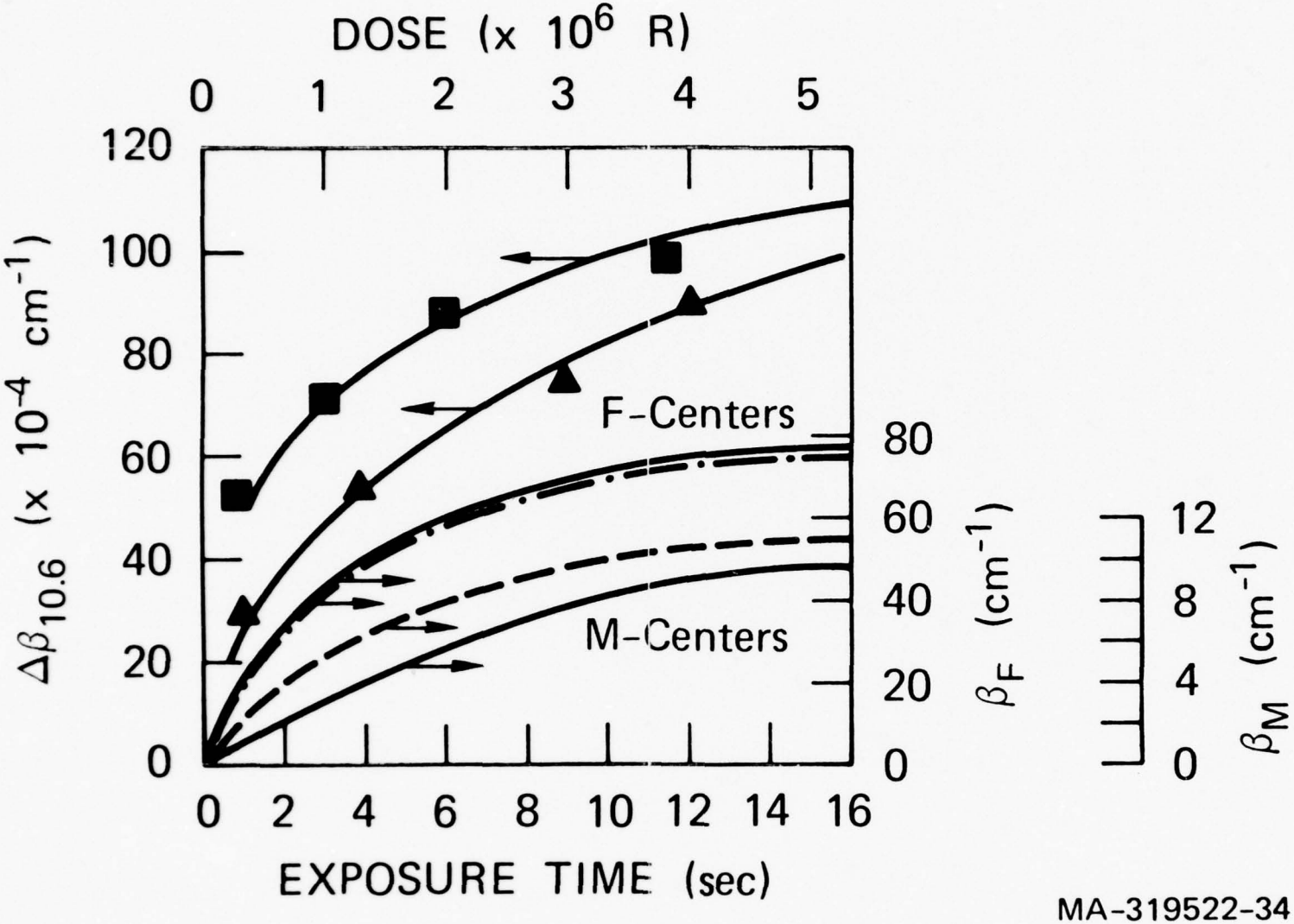
DOSE (x 10^6 R)
0 1 2 3 4 5
120
100
80
60
40
20
0
Δβ10.6 (x 10^-4 cm^-1)
F-Centers
M-Centers
80
60
40
20
0
βF (cm^-1)
12
8
4
0
βM (cm^-1)
0 2 4 6 8 10 12 14 16
EXPOSURE TIME (sec)

MA-319522-34

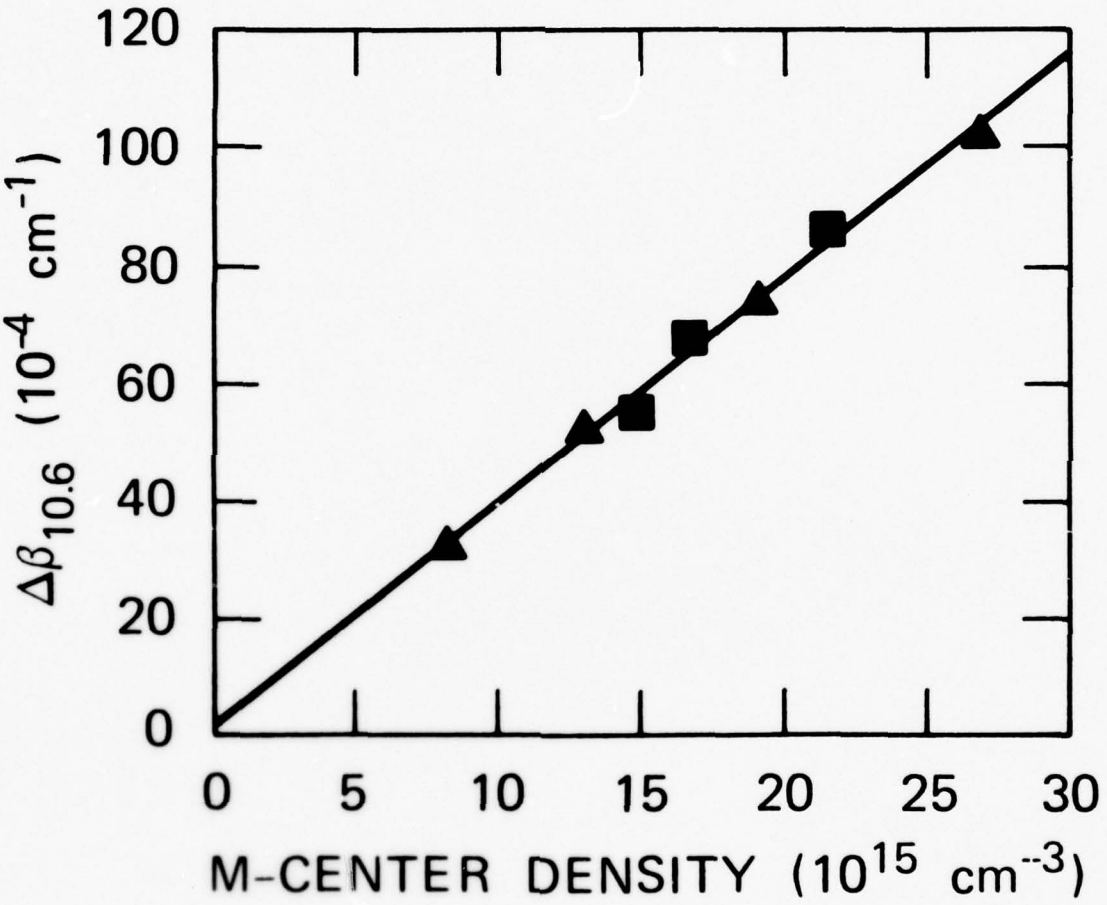
120
100
80
60
40
20
0
$\Delta\beta_{10.6}$ (10^{-4} cm^{-1})
0
5
10
15
20
25
30
M-CENTER DENSITY (10^{15} cm^{-3})

MA-319522-35

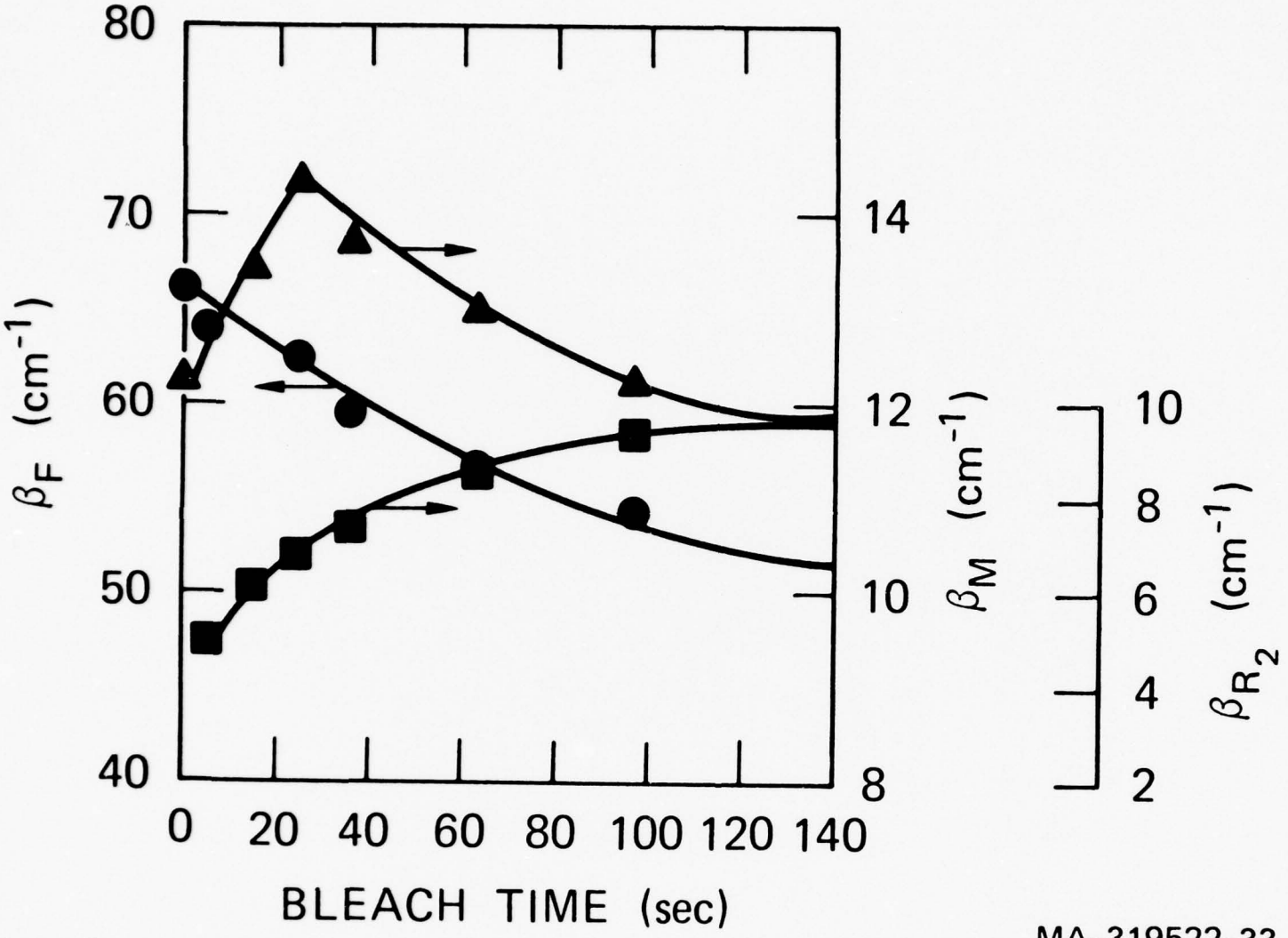
80
70
60
50
40
β_F (cm^{-1})
14
12
10
8
β_M (cm^{-1})
10
8
6
4
2
β_{R_2} (cm^{-1})
0 20 40 60 80 100 120 140
BLEACH TIME (sec)

MA-319522-33

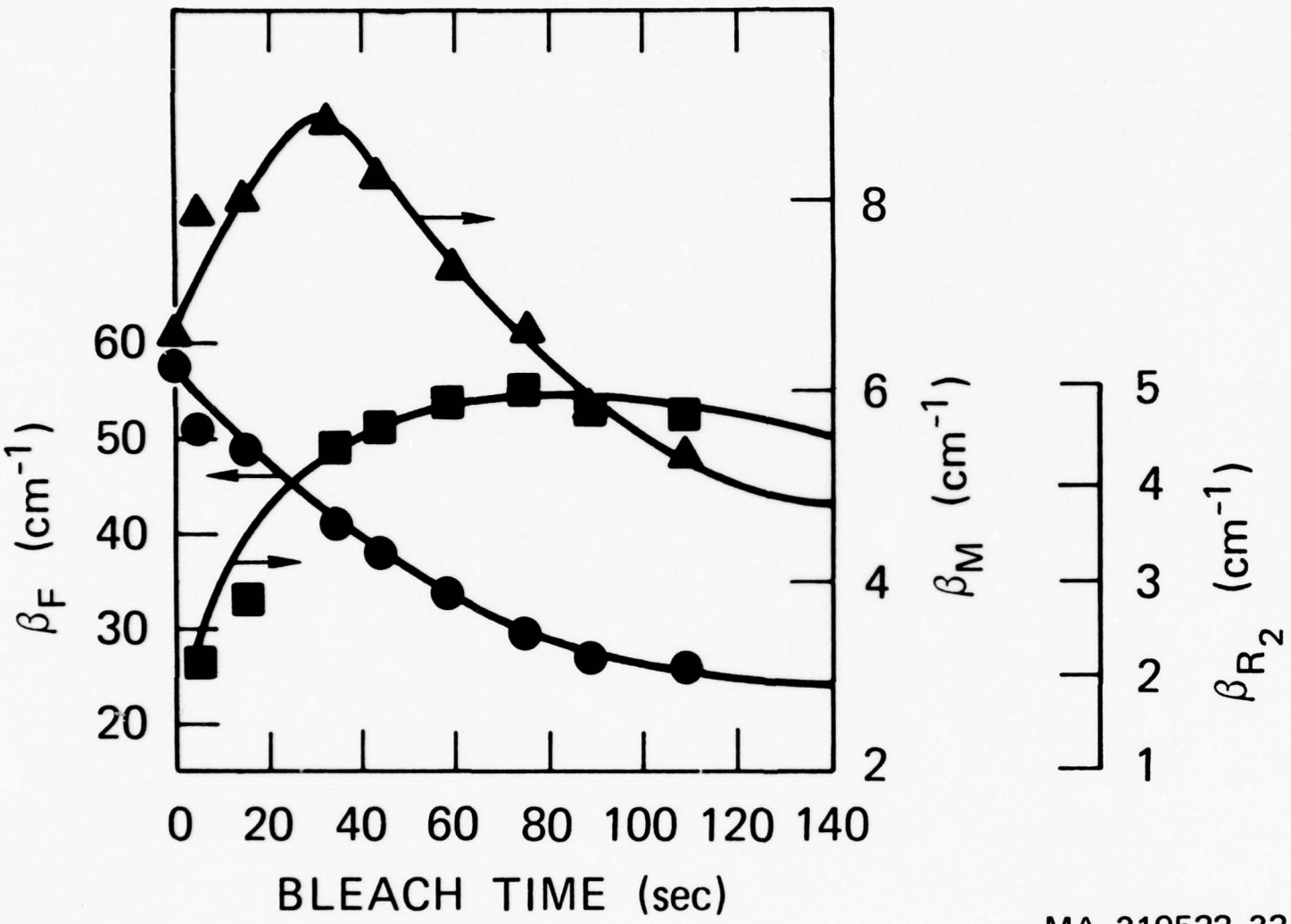
60
50
40
30
20
β_F (cm^{-1})
8
6
4
2
β_M (cm^{-1})
5
4
3
2
1
β_{R_2} (cm^{-1})
0 20 40 60 80 100 120 140
BLEACH TIME (sec)

MA-319522-32

APPENDIX D

REPRINT

"COMPACT LASER CALORIMETER FOR MEASURING ABSORPTION COEFFICIENTS OF SMALL SAMPLES"

By

T. J. Magee, N. M. Johnson, M. Lehmann, J. Peng, and J. Hannigan
Review of Scientific Instruments 47, 301 (1976)

Compact calorimeter for measuring laser absorption coefficients of small samples*

T. J. Magee, N. M. Johnson, M. Lehmann, J. Peng,† and J. Hannigan

Stanford Research Institute, Menlo Park, California 94025

(Received 12 June 1975; in final form, 10 November 1975)

A relatively simple calorimeter has been designed for measuring laser absorption coefficients on samples of small cross-sectional area. This instrument has proven useful in studies of absorption or scattering within samples by microscopic defects, where bulk samples of small volume are required.

Calorimetry has been used extensively for the measurement of laser absorption coefficients in a number of materials. In most cases, laser calorimetric measurements have been obtained on specimens 0.5–10 cm in length and of cross-sectional area ≥ 1 cm^2. However, for samples containing extremely small ($\leq 0.25\,\mu$) defects it is often difficult to assess the influence of these defects on the effective laser absorption coefficient using conventional calorimeters designed for samples of large volume, typically of the order of several cubic centimeters. In this paper we report the development of a simple compact laser calorimeter for measuring absorption coefficients on samples of volume <0.4 cm^3.

Figure 1 shows a photograph of a calorimeter adapted for measurements on small volume samples. In Fig. 2 a cross-sectional view of the instrument shows schematically the interior features of the calorimeter cavity. The case is constructed of brass and the interior of the cavity and cover blackened to reduce spurious reflections. The sample is mounted within a separate plastic case and is supported at the bottom by plastic point contacts to reduce thermal contact losses. A spring-loaded copper–constantan thermocouple bead is depressed against the target and provides the only contact point at the top of the sample. Using the technique of Hass *et al.*,[1] a metallic mirror coating on the thermocouple bead is used to reduce thermal contributions by scattered radiation. The incident laser beam is directed through two 1 mm diam apertures onto the sample surface. The front surface of the external aperture plate is coated with a thin gold film to prevent absorption and subsequent radiative heating of the internal sample chamber.

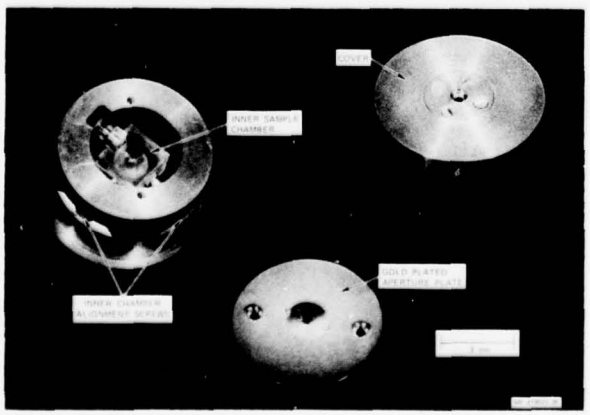

FIG. 1. Photograph of calorimeter.

Alignment is performed using a milliwatt He–Ne laser. The sample position with respect to the incident beam is altered by the $X-Y$ displacement screws, which shift the entire inner chamber within the calorimeter cavity. The temperature rise and decay of the laser irradiated targets are measured with a microvoltmeter, and the data are recorded on an $X-Y$ recorder. All thermocouple wires and interconnecting cables are shielded to reduce electrical noise during the experiments.

From thermocouple measurements, the absorption coefficient, β can be determined using the approximation,[2–4]

$$\beta \simeq \frac{MC_p}{LP_T}\,\frac{2n}{n^2+1}\left(\left.\frac{dT_{\text{rise}}}{dt}\right|_{T_1} + \left|\frac{dT_{\text{decay}}}{dt}\right|_{T_1}\right), \quad (1)$$

where M is the mass of the sample; C_p, the specific heat at constant pressures; L, the length of the sample; P_T, the transmitted power; n, the refractive index; and $dT_{\text{rise}}/dt_{T_1}$, $dT_{\text{decay}}/dt_{T_1}$, the temperature rise and decay rates, respectively, at temperature T_1. To utilize this technique and the approximation given in Eq. (1) requires that a number of experimental parameters be carefully controlled, as discussed in a number of recent papers.[1–5] In comparison with calorimetry performed on large surface area (≥ 1 cm^2) samples, the experimental requirements for laser calorimetry on small surface area ($\simeq 0.09$ cm^2) samples used in the present application are equally stringent. In particular, the small size of the samples necessitates very careful alignment to ensure that the incident laser beam is directed at the center of the sample face and parallel to the z axis of the sample. In addition, extreme care must be exercised in surface polishing to minimize scattering and losses on the smaller samples. Temperature contributions by radiation scattered in the direction of the thermocouple must be minimized. The use of a metallic mirror coating on the thermocouple bead has been shown to be effective in this application and in previous experiments by Hass *et al.*[1] Conduction losses are minimized by the plastic point contact supports at the bottom of the sample. In comparison to conventional laser calorimetry systems the sample mass is reduced by a factor of approximately ten. From Eq. (1) (assuming a

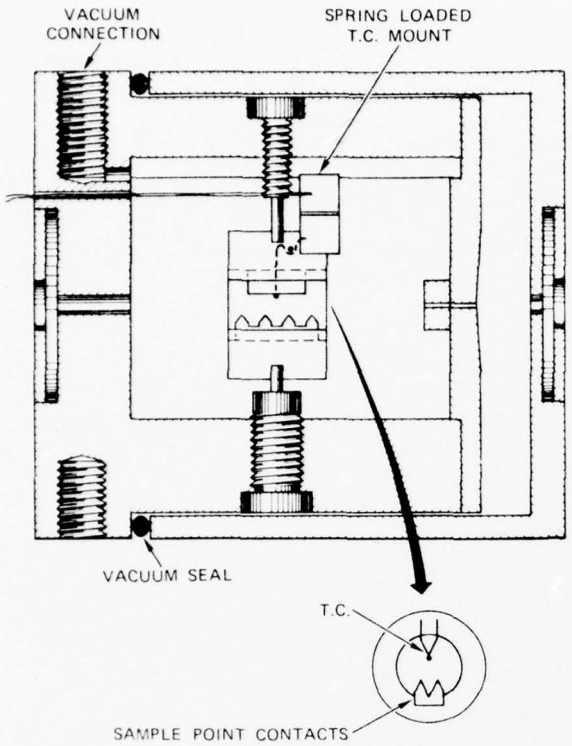

FIG. 2. Schematic of internal calorimeter design.

fixed absorption coefficient) a one-tenth reduction in mass is accompanied by an order of magnitude increase in the temperature rise signal. Hence, in the present system the use of small samples and shielding of thermocouple and interconnecting cables results in a relative increase in the signal-to-noise ratio. On samples tested thus far, thermocouple voltages were measured in the range 2–35 μV. The corresponding error in the measurement of β at 10.6 μ was determined to be $\pm 1 \times 10^{-5}$ cm^{-1}.

In all applications of thermocoupled-based laser calorimetry surface absorption will contribute to the thermal rise signal, possibly introducing errors in the measurement of very low absorption coefficients. Hass *et al.*[1] have presented a detailed description of an experimental method for separating bulk and surface absorption. Briefly, this technique involves measurement of the thermal rise rate at very early times after the onset of laser irradiation. Surface absorption is generally apparent by the presence of an increased slope at much later times on the thermal rise curve. The "initial slope" method then permits an adequate determination of β, essentially independent of the amount of surface absorption. In the present system the thermal rise rate was determined at times less than 10 sec after the onset of recording.

Experiments have utilized a 10 W CO_2 laser, with exposure times in the range 15–30 sec. Samples were in the form of parallelepipeds of cross-sectional area $\approx$0.09 cm^2 and length $\leq$4 cm. The results obtained on a selected number of ZnSe samples are given in Table I. Also listed for reference are the absorption coefficients measured on larger volume samples from the same lot by Raytheon Research Laboratories. The data indicate that visibly clear ZnSe samples displaying no apparent scatter sites or turbidity zones[6] exhibit an absorption coefficient $<2 \times 10^{-3}$cm^{-1}, in agreement with results obtained by Raytheon. Samples displaying a high density of internal defects or turbidity bands exhibit an effective absorption coefficient in the range 2.6×10^{-3}–4.3×10^{-3} cm^{-1}, in proportion to the density of internal scatter sites. Correlated transmission electron microscopy (TEM) examination of these samples revealed submicron sized segregations in the visible scatter regions. Electron diffraction (TED) patterns indicated that the precipitate regions are composed of zinc. In all cases there was no evidence of microscopic voids in turbidity zones.

Additional tests at 10.6 μ on small samples of NaCl and KCl yielded absorption coefficients in reasonable agreement with values measured by Naval Research labs. Other evaluations of CdTe obtained from a number of suppliers have shown a definite correlation between the change in the 10.6 μ absorption coefficient and the microscopic defect density, in agreement with previous results.[7]

The data obtained to date show that the present calorimeter can be used for measuring absorption coefficients of small samples. In particular, the present apparatus appears to be useful in measurements of the relative change in effective absorption by varying densities of microscopic defects within discrete or localized regions of a sample.

The authors wish to acknowledge the assistance of the Raytheon Co. and NRL in supplying samples and information.

TABLE I. Data summary.

Sample	$\beta_{10.6}$ (cm^{-1})	Comments
(1) ZnSe	1.7×10^{-3}	$\beta_{10.6}$ also measured on bulk samples by Raytheon Co. in the range $1-2 \times 10^{-3}$ cm^{-1}; density of apparent scatter sites low.
(2) ZnSe	1.9×10^{-3}	
(3) ZnSe	2.6×10^{-3}	Density of visible scatter sites moderate to high; submicron segregations of Zn identified by TEM and TED.
(4) ZnSe	3.1×10^{-3}	
(5) ZnSe	4.3×10^{-3}	

* Research supported by Air Force Office of Scientific Research Contract No. F44620-73-0019.

† Postdoctoral fellow.

[1] M. Hass, J. W. Davisson, H. B. Rosenstock, and J. Babiskin, Appl. Opt. **14,** 1128 (1975).

[2] H. G. Lipson, L. H. Skolnik, and D. L. Stierwalt, *Proceedings of the Third Conference on High Power Infrared Laser Window Materials*, edited by C. A. Pitha and B. Bendow, U.S. Air Force Cambridge Research Labs Tech. Rep. TR-74-0085(1), Bedford, MA, 1974, p. 337.

[3] A. Kahan, H. G. Lipson, and L. H. Skolnik, in Ref. 2, p. 307.

[4] L. H. Skolnik, A. Hordvik, and A. Kahan, Appl. Phys. Lett. **23,** 477 (1973).

[5] E. G. Bernal, Appl. Opt. **14,** 314 (1975).

[6] R. N. Donadio, A. W. Swanson, and J. Pappis, *Proceedings of the Fourth Annual Conference on Infrared Laser Window Materials*, edited by C. R. Andrews and C. L. Strecker, U.S. Air Force Materials Lab Special Report, Wright-Patterson AFB, OH, 1974, p. 493.

[7] T. J. Magee, J. Peng, and J. Bean, Phys. Status Solidi A **27,** 557 (1975).

APPENDIX E

REPRINT

"A COUPLED LASER-SCANNING ELECTRON MICROSCOPE
SYSTEM FOR INVESTIGATING LASER-MATERIALS INTERACTIONS"

By

T. J. Magee, P. Krehl, K. Hirschberg and J. Terry
Review of Scientific Instruments 45, 907 (1974)

A coupled laser scanning electron microscope system for investigating laser materials interactions*

Thomas J. Magee, Peter Krehl†, Kenneth Hirschberg, and Jan Terry

Stanford Research Institute, Menlo Park, California 94025

(Received 2 November 1973; and in final form, 14 March 1974)

This paper reports the development of a coupled laser scanning electron microscope system that enables a laser beam to be introduced into the microscope sample cavity and permits active-mode monitoring of surface modifications during or subsequent to laser pulsing. Instrumentation is also incorporated within the system design for measuring laser induced pressures and equivalent laser coupling coefficients in target materials.

INTRODUCTION

Considerable effort has been devoted over the past few years to the investigation of laser interaction with materials.[1,2] The use of the scanning electron microscope (SEM) has proven to be a powerful adjunct in laser damage studies of metals, thin film coatings, and optical components. However, the use of SEM analysis in laser interaction studies has, in the past, been confined to examining materials subsequent to exposure to a laser beam.

This paper reports the development of a coupled laser scanning electron microscope system that enables a laser beam to be introduced into the SEM cavity and permits active-mode monitoring of surface modifications obtained during or subsequent to laser pulsing. The system is presently being used to record data on video tape during long cw laser exposure, or in a multiple frame mode subsequent to pulsed laser exposure. In the sections to follow, modifications to the SEM and time synchronization circuity design will be described, accompanied by descriptions of incorporated instrumentation for measuring laser induced pressures and equivalent coupling coefficients.

MODIFICATION OF THE SEM SAMPLE CHAMBER

A Cambridge scanning electron microscope (Stereoscan model Mark IIA) was utilized in the present system, and alterations were provided to accommodate the laser beam within the sample chamber. To ensure that the laser beam would not interfere with the mechanical or electrical components of the SEM during laser pulsing, an entrance port at the rear of the SEM was selected, and a mounting plate designed to include an extender tube and focusing lens. A 28 cm focal length lens was used to obtain variable laser spot sizes at the sample surface. Use of a manually operated shutter assured essentially light-tight conditions for normal SEM applications. A telescope mounted at the front of the SEM cavity was deployed to optically align the laser beam on the sample surface.

Due to the lack of sufficient tilt adjustment on the sample stage of the SEM, it was necessary to fabricate special sample holders to allow simultaneous positioning of the specimen with respect to both the electron beam and the laser beam; 76 μ Chromel/constantan thermocouple wires were also spot welded to the rear of 1 cm diam samples on the modified holders, thereby permitting the foil temperature to be monitored within the SEM subsequent to laser pulsing.

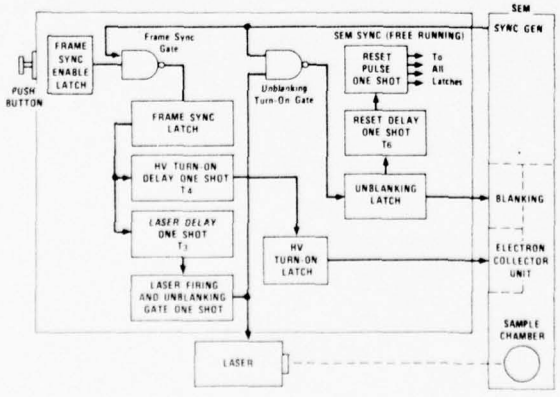

FIG. 1. Block diagram of the electrical system for the coupled laser–SEM unit.

LASER–SEM SYNCHRONIZATION

To obtain active mode monitoring of laser-irradiated surfaces the following requirements must be fulfilled:

(i) The first frame in the single- or multiple-frame mode must be initiated at a desirable time after laser firing for high power pulsed lasers or at some time during laser activation for long pulse (cw) or low power laser applications.

(ii) The laser pulse has to be synchronized with the frame sweep to avoid "partial" framing.

(iii) The time required to obtain a single frame should be variable, but the maximum should be $\lesssim$100 msec.

(iv) To prevent damage of the metallization coating on the light pipe the low voltage (250 V) on the entrance grid of the collector unit must be switched on only after high power laser pulsing and plasma dispersion ($\lesssim$1 msec), but prior to initiation of framing.

A block diagram and a schematic of the electronic system designed for this application are shown in Figs. 1 and 2. To facilitate understanding of the system and the correlation

 Copyright © 1974 by the American Institute of Physics

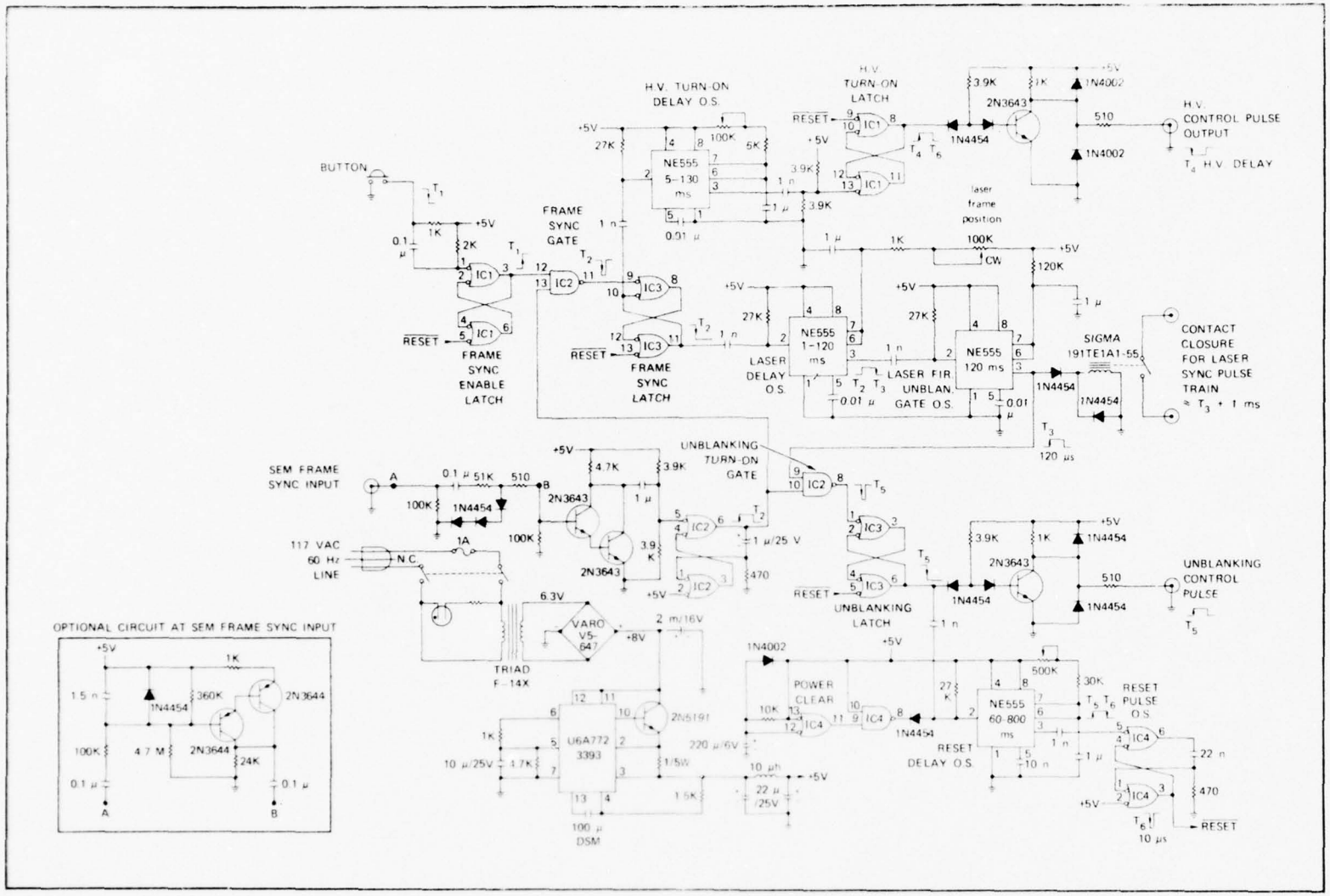

FIG. 2. Schematic of the electrical circuit for laser–SEM coupling. Unless otherwise indicated, all resistors are ¼ W. Units IC1–IC4 are SN7400N and on each of the units pin 7 is connected to ground and pin 14 is connected to +5 V. Pin 14 is also bypassed to ground with a 0.01 μF low voltage ceramic capacitor. On all NE555 units pins 4 and 8 are bypassed to ground with 0.01 μF low voltage ceramic capacitors. The RESET DELAY ONE SHOT pulse may be lengthened by replacing the 500 kΩ variable resistor with a larger unit. If the SEM is equipped with a standard TV system, the section between A–B is replaced at the SEM FRAME SYNC INPUT with the optional circuit.

between the various delay times mentioned in the description to follow, a timing diagram is shown in Fig. 3.

CIRCUIT DESCRIPTION

Synchronization pulses are continually received from the SEM synchronization generator. The leading edge of each pulse is used to trigger the FRAME SYNC PULSE ONE SHOT, which produces well-defined, $\frac{1}{2}$ msec sync pulses. At some arbitrary time, T_1, a push button is depressed to initiate the experiment. The push button is ac-coupled to the FRAME SYNC ENABLE LATCH, thus eliminating contact-bounce effects and assuring only one operation per push of the button. This latch is set at T_1 and enables the FRAME SYNC GATE until it is reset at T_6. Beginning with the next sync pulse (T_2) after the framing period when the button was pushed, a train of this pulse and each succeeding sync pulse appears at the output of the FRAME SYNC GATE, until the system is reset at T_6. The width of the sync pulse ($\frac{1}{2}$ msec) is small compared to the frame width, so that any time ambiguity caused by the button being pushed during a sync pulse is negligibly small and, further, only likely to occur in 0.5% of the experiments. The first pulse that occurs at the output of the FRAME SYNC GATE is the only one of interest for timing purposes; hence the leading edge is preserved, and all succeeding pulses are inhibited by means of the FRAME SYNC LATCH, whose output is set at T_2 and not reset until T_6.

The output of the FRAME SYNC LATCH initiates two independently adjustable timing chains. The first of these determines the time the laser will be fired in the frame following the one in which the button was pushed. The second chain determines the time the high voltages will be restored for viewing.

The first chain begins with the initiation at T_2 of the LASER DELAY ONE SHOT, an analog timer with a period that is adjustable from 1 to 120 msec. The end of the timing period that is generated by this timer, T_3, is edge-coupled to and initiates a second analog timer with a fixed period of 120 msec. The pulse output from this timer is used to fire the laser at T_3, and it also enables the UNBLANKING TURN-ON GATE for 120 msec, a period sufficient to ensure that at least one SEM sync pulse will actuate this gate. At T_5, the next SEM sync pulse activates the UNBLANKING TURN-ON GATE, which in turn sets the UNBLANKING LATCH. The signal from this latch turns on the unblanking control pulse, thus restoring SEM data recording. It also initiates the RESET DELAY ONE SHOT, an analog timer whose timing period is adjustable from 60 msec to infinity to determine the number of frames desired. At the completion of the RESET DELAY ONE SHOT timing period, T_6, the RESET PULSE ONE SHOT is initiated to reset the four latches at T_6, making the system ready for the next experiment. The generation of a "power clear" signal initiates the RESET DELAY ONE SHOT and then the RESET ONE SHOT, allowing any circuitry that may have been activated by power "turn-on" to finish timing out. After that, all the latches are reset.

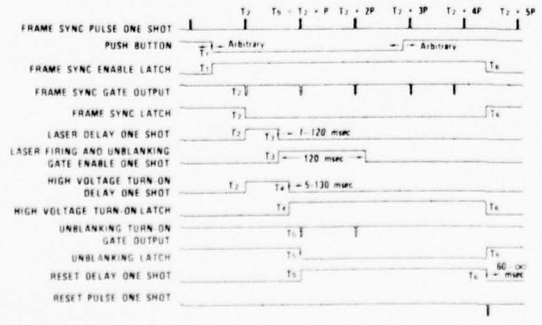

FIG. 3. Timing diagram.

The second timing chain begins with the initiation of T_2 of the HIGH-VOLTAGE TURN-ON DELAY ONE SHOT, an analog timer with a timing period that is adjustable from 25 to 160 msec. The end of the timing period is likewise edge-coupled to, and sets the HIGH-VOLTAGE TURN-ON LATCH, which simultaneously turns on the HIGH-VOLTAGE CONTROL PULSE. The latter unit is reset at T_6.

COMBINED SEM SAMPLE HOLDER AND PRESSURE GAUGE

A Sandia-type quartz gauge[3–5] has been designed for use in the coupled laser–SEM system. In Fig. 4 a schematic of the gauge in cross section provides information on constructional details. The packet was designed so that the outer diameter would be of approximately the same dimension as that of a normal sample holder ($\simeq$12 mm) used in the SEM. The quartz-gauge element was 10 mm in diameter, 1 mm in thickness and had a guard ring diameter of 5 mm. The sensitivity of the gauge was 1.13 V/kilobar when used with a 50 Ω load resistor. The propagation time for the sound pulse was 174 nsec ($v = 5.72$ mm/μsec) and very long compared to the half-width of the laser (30 nsec). The thickness of the sample d_s, used in the experiment, had to satisfy the condition

$$d_s > 174 \text{ nsec } v_s/2,$$

where v_s is the velocity of sound in the sample. If this requirement is not fulfilled, a pulse reflected at the rear surface of the sample would again reach the gauge during the loading phase (174 nsec), resulting in erroneous or ambiguous pressure gauge records.

Figure 5 shows the experimental configuration. A Korad 1500 Nd–glass laser was focused by a simple lens of 600 mm focal length through a quartz plate 10 mm thick into a 10 mm circular region on an aluminum disk of 2 mm thickness and 10 mm diam. The output of the quartz gage was recorded on a Tektronix 7704 oscilloscope. On the same oscilloscope, the laser pulse was displayed to provide an ac-

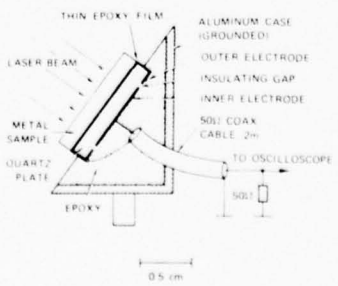

FIG. 4. Cross section of the quartz gauge with mounted sample.

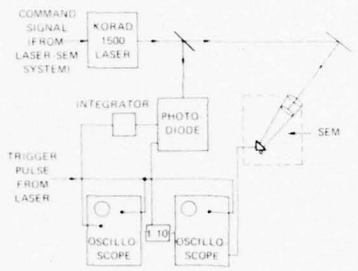

FIG. 5. Schematic of the experimental configuration.

curate time correlation between laser firing and the arrival of the pressure pulse. A second oscilloscope was used to monitor the beam energy, which in these experiments was between 3 and 10 J.

EXPERIMENTAL APPLICATION

Metal and semiconductor samples exposed to a laser beam within the laser–SEM system included tantalum, porous beryllium, aluminum, tin, and cadmium telluride. The metal foils were exposed to a 60 nsec 1 J laser beam focused to a power density of $\simeq 10^8$ W/cm² and 30 nsec Nd laser pulses (1–10 J) of maximum power density, 10^{10} W/cm². Cadmium telluride was exposed to a 100 W cw CO_2 laser beam focused to a power density of $\simeq 10^4$ W/cm².

Metal samples examined subsequent to pulsed laser exposure indicated the presence of melt-produced craters, recrystallization, and thermal microcracking. Anodized aluminum samples exhibited a more severe surface alteration and the number of melt-produced craters were found to increase as a function of oxide thickness.

Correlated measurements of the equilibration temperatures T_e, at the back surface of the laser irradiated surfaces were used to determine the laser coupling coefficient, α. In this case, α is defined as the fractional amount of laser energy coupled into the sample and converted into thermal energy, such that

$$\alpha = mc\Delta T/E, \tag{1}$$

where m is the mass of the target, c is the specific heat, ΔT is the difference between the equilibration temperatures and room temperature, and E is the incident laser energy. It has been shown[6] that the corrected equilibration temperature ΔT, relative to room temperature can be described by

$$\Delta T = T_1 \exp(ct_1), \tag{2}$$

where $c = (1/t_2 - t_1)\ln(T_1/T_2)$ and T_1 and T_2 are the monitored above ambient temperature at time t_1 and t_2. Substituting Eq. (2) for ΔT in Eq. (1) and using appropriate experimentally determined values, we found the laser coupling coefficient for aluminum samples irradiated with a pulsed ruby or Nd laser beam to lie in the range 0.28–0.30. Similarly, for laser irradiated tantalum foils, the coupling coefficient was found to be 0.36. The presence of an anodization layer on the aluminum samples increased the coupling slightly and values of α in the range 0.32–0.36 were recorded.

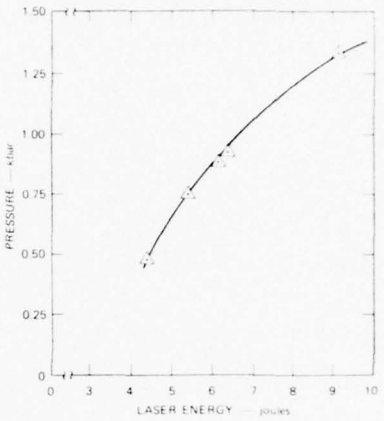

FIG. 6. Stress induced in aluminum as a function of laser energy. Sample thickness—0.2 cm.; irradiated area—0.8 cm².

Using the combined SEM sample holder–pressure gauge package shown in Fig. 4, laser-induced pressures were recorded in uncoated and anodized aluminum targets of approximately 2 mm thickness. Oscilloscope records displaying both the laser signal and the pressure signal indicated a time separation of 370 nsec, agreeing well with the propagation time of the pressure pulse through the 2 mm thick aluminum target. The widths of the pressure signal at half maximum were approximately the same as that of the laser pulse (30 nsec) in all experiments. In Fig. 6 the results obtained on uncoated aluminum are shown in a plot of measured pressure as a function of laser energy, assuming an irradiation area of 0.8 cm².

Thermocouple measurements indicated that the effective laser coupling coefficient was less than 0.30 for untreated aluminum surfaces and that only a small portion of the laser energy was absorbed in the samples. However, both the absorption and the induced pressure increased when the surface was anodized. In addition, more severe surface damage was observed in the anodized samples, implying that the surface quality is an important parameter in laser–metal interactions.

*Work supported by AFOSR Contract No. F44620-73-0019.
†Visiting scientist from Physics Department, Technical University, Berlin, West Germany.
[1] *Laser Interaction and Related Plasma Phenomena*, edited by H. J. Schwarz and H. Hora (Plenum, New York, 1971).
[2] J. F. Ready, *Effects of High-Power Laser Radiation* (Academic, New York, 1971).
[3] R. A. Graham, F. W. Neilson, and W. B. Benedick, J. Appl. Phys. **36**, 1775 (1965).
[4] W. J. Halpin, O. E. Jones, and R. A. Graham, ASTM Special Pub. No. 336, 1963.
[5] G. A. Jones and W. J. Halpin, Rev. Sci. Instrum. **39**, 258 (1968).
[6] K. G. Gilbert and R. L. Carson, Technical Report No. AFWL-TR-72-168, Air Force Weapons Laboratory, 1972.

APPENDIX F

PREPRINT

"MICROSCOPIC DEFECTS AND INFRARED ABSORPTION IN CADMIUM TELLURIDE"

By

T. J. Magee, J. Peng, and J. Bean
Physica Status Solidi (A) 27, 557 (1975)

MICROSCOPIC DEFECTS AND INFRARED ABSORPTION IN CADMIUM TELLURIDE[1)]

By

T. J. Magee, J. Peng[2)], and J. Bean[3)]

Stanford Research Institute, Menlo Park, California 94025

ABSTRACT

This paper reports on the observed correlation in CdTe between microscopic defects and the infrared absorption at 10.6 μm. The data were obtained from transmission electron microscopy, scanning electron microscopy, infrared and optical microscopy, spectrophotometry, and laser calorimetry. For chlorine and indium doped samples it was determined that increasing the concentrations of In_2Te_3 and $CdCl_2$ precipitate platelets subsequently increases the 10.6 μm infrared absorption coefficient in CdTe. Isolated dislocations, dislocation networks, tellurium precipitates, vacancy loops, and stacking faults were also shown to exercise an important influence on infrared absorption. Localized regions of defect aggregations in many samples were found to be responsible for the macroscopic absorption sites typically observed by infrared microscopy. The significant differences between the present data and previously reported macroscopic defect models are discussed.

---

1) Research supported by Air Force Office of Scientific Research Contract No. F44620-73-0019 and Office of Naval Research Contract No. N00014-73-C-0378.

2) Post doctoral fellow, Stanford Research Institute.

3) Doctoral candidate, Dept. Applied Physics, Stanford University.

In dieser Arbeit wird über den Zusammenhang zwischen mikroskopischen Fehlstellen und der 10,6 µm Infrarotabsorption in CdTe berichtet, der bei der Auswertung von Daten, gewonnen durch Transmissionselektronenmikroskopie, Rasterelektronenmikroskopie, Infrarot-und Lichtmikroskopie, Spektrophotometrie und Laserkaloremetrie, beobachtet wird. In Clor und Indium dotierten Proben ergibt sich, daß steigende Konzentrationen von In_2Te_e und $CdCl_2$ Ausscheidungslamellen anschließend den 10,6 µm Infrarotabsorptionskoeffizienten in CdTe erhöhen; isolierte Versetzungen, Versetzungsnetzwerke, Telluraus-scheidungen, Leerstellenringe und Stapelfehler haben ebenfalls einen wesentlichen Einluß auf die Infrarot-absorption. In vielen Proben werden lokale Bereiche von Fehlstellenanhäufungen als Ursache für die in der Infrarotmikroskopie häufig beobachteten makroskopischen Absorptionsstellen gefunden. Die wesentlichen Unterschiede zwischen den gefundenen Ergebnissen und den vorher beschriebenen Fehlstellenmodellen werden diskutiert.

---

1. Introduction

Considerable interest has been shown in the development of highly transparent window materials for use in high-power infrared laser systems. Cadmium telluride (CdTe) has offered some promise in this area because of its superior thermomechanical properties and resistance to environmental influences. However, the development of laterally uniform, large surface-area samples having infrared absorption coefficients, β, as low as 10^{-4} cm^{-1} in the 10.6 μm range has posed difficulties.

It was previously shown [1,2] for a number of laser window materials that the exponential changes in β as a function of frequency were intrinsic and could be related to multiphonon absorption processes. Theoretical analyses, however, indicate that only a small portion of the observed 10.6 μm absorption in currently available CdTe samples could be related to an intrinsic absorption mechanism. [3] It has been demonstrated [3-5] that native or secondary defects are inevitably present in CdTe and that these defects are responsible for the increased infrared absorption. Recently, Sparks and Duthler [6] presented a theoretical model that indicated that small concentrations of bulk or surface defects or inclusions in window materials can significantly alter the value of β at 10.6 μm.

In all the previous experimental studies, the defect structure has been inferred from optical and infrared microscopic examinations of samples after growth and subsequent post-anneal treatments. Because of the limited resolution available with these techniques, the nature

of microscopic defects in CdTe and the mechanism of absorption at 10.6 μm have not been clearly defined. This paper presents data on microstructural defects observed in CdTe samples and discusses the correlation between the defect concentration and infrared absorption at 10.6 μm.

2. Experimental

Cadmium telluride samples of (111) orientation were obtained from Hughes Research Labs, II-VI Corporation, and Tyco Labs. The samples were doped with either indium or chlorine to concentrations $\geq 10^{17}/cm^3$. After mechanical and chemical polishing, samples were examined in the SEM for surface defects. Energy dispersive x-ray analyses were also performed within the SEM to ascertain the presence of contaminants that might influence the value of infrared absorption at the surface.

Laser calorimetry experiments using copper-constantan thermocouples attached to the sides of the sample, were conducted to measure absorption at 10.6 μm. In all experiments we used a 50-Watt Coherent Radiation (Model 42) CO_2 laser focused to a beam diameter of 3 mm to 8 mm at the center of the sample face. A Coherent Radiation (Model 201) power meter was used to measure incident or transmitted laser powers. Separate measurements of infrared absorption were also made before and after laser irradiation with a Perkin Elmer (Model 247) infrared spectrophotometer.

Small (3-mm-diameter) disks were cut from each of the samples for TEM analysis. A jet thinning technique was used to prepare extremely thin CdTe samples for examination in the electron microscope (7). Data obtained from TEM analyses were then correlated with gross macrostructural defects ($\geq$ 1 μm) observed in an infrared microscope (Research Devices, Model D).

Samples were annealed in evacuated quartz ampoules with pieces of 6N-purity cadmium. Cd and CdTe samples were positioned at opposite ends of the ampoule and the CdTe end placed at the maximum temperature point of the furnace to inhibit Cd vapor transport to the sample surfaces. Individual samples were annealed at temperatures from 100°C to 900°C for periods of 1 to 48 hours.

3. Results

Data obtained from transmission electron microscopy analyses of indium and chlorine doped samples are summarized briefly in Table 1. Representative micrographs illustrating the microstructure are shown in Figs. 1-3.

Identification of the precipitate platelet composition (Fig. 1) was established in two separate experimental methods. These included an analysis of the electron diffraction patterns and an analysis of measured Moire fringe spacings (8) observed on the platelets. Measurements of lattice plane spacings from electron diffraction ring patterns and subsequent measurements of relative diffraction intensities were compared with ASTM data (9). Agreement between experimental and published data was found within $\pm$ 1 percent. Using measurements of Moire fringe spacings on over 400 precipitates, lattice plane spacings were determined which consistently agreed with values for In_2Te_3. In similar fashion, $CdCl_2$ precipitates were identified in chlorine-doped samples.

From the earlier work of de Nobel (10) in 1959 it is known that the presence of indium in CdTe can result in an increased concentration of Cd vacancies or an excess of tellurium. In the present investigation polycrystalline tellurium rings have been observed in most of the electron diffraction patterns obtained from indium-doped samples. The tellurium

precipitates have been directly observed by TEM and found to be $\simeq 60$ Å in diameter. In samples annealed at temperatures $\geq 500^{\circ}C$, there was no evidence of tellurium precipitation either in the transmission electron micrographs or electron diffraction patterns. Since the melting point of Te is $< 500^{\circ}C$, it seems likely that the precipitates have decomposed and the tellurium diffused into the lattice.

In several samples, stacking faults (Fig. 2) were observed to increase in both size and number after short-term annealing within the electron microscope. In regions of stacking fault growth, a large number of 1000 Å-1500 Å diameter dislocation loops were observed. Using conventional TEM techniques (11,12), the loops were subsequently determined to be composed of vacancies. It is believed that the increase in stacking fault length occurs in localized vacancy-rich regions of the sample, but the mechanism of growth will require an accurate determination of thermal activation energies for the process.

An electron micrograph of a sample containing dislocations in the form of complex tangles or forests is shown in Fig. 3. After annealing, reordering occurs within the forests and isolated dislocations remain. Examination of selected area electron diffraction patterns within localized regions of high dislocation density have repeatedly indicated the presence of tellurium precipitates. The data then indicate that dislocation networks are inevitably associated with tellurium segregation regions or with areas containing excess cadmium vacancies.

Using infrared microscopy, a number of investigators have reported (3-5) macroscopic (≥ 1 μm) absorption regions in CdTe and subsequently proposed void or precipitate models related to crystal growth and post-anneal conditions. We also examined samples in the infrared microscope and found absorption sites of varying morphologies, ranging from $\simeq 1$ μm to 6 μm in size. Typically, the smaller sites (1 μm to 2 μm) appeared granular, suggesting nonuniform absorption or scattering within the defect site. After annealing at temperatures $> 500^{\circ}C$ in cadmium vapors, several of the sites were either reduced in size or no longer visible. Some of the absorption centers remained essentially unaltered after annealing for 48 hours, with only a slight reduction in size.

To obtain further information on the structure of the macroscopic absorption sites (1 μm to 6 μm), samples were sectioned within the absorption regions and subsequently thinned for TEM analysis. Evidence of large micron sized voids, as hypothesized previously (3-5) from optical and infrared microscopic data, was not detected in the electron microscope. Instead, macroscopic absorption sites were shown to be associated with distinct defect aggregations, namely: (1) complex arrays of dislocation lines and tangles, (2) aligned stacking faults, and (3) localized regions of In_2Te_3 or $CdCl_2$ precipitate platelets.

To provide correlation between the observed microstructural defects and infrared transmission, we determined the absorption coefficient at 10.6 μm from spectrophotometer and laser calorimetry measurements. It has been shown (13-15) that the absorption coefficient, β, can be determined from laser calorimetry measurements by using thermocouple measurements of the thermal rise and decay rates of laser irradiated targets. The approximation is given by:

$$\beta \simeq \frac{M C_p}{L P_T} \frac{2n}{n^2 + 1} \left[\left(\frac{dT}{dt} \right)_{rise, T_1} + \left| \left(\frac{dT}{dt} \right)_{decay} \right|_{T_1} \right] , \qquad (1)$$

where M is the mass of the sample, C_p, the specific heat at constant pressure, L, the length of the sample, P_T, the transmitted power, n, the refractive index, and, $\left(\frac{dT}{dt} \right)_{rise, T_1}$, $\left| \left(\frac{dT}{dt} \right)_{decay} \right|_{T_1}$, the temperature rise

and decay rates, respectively, at temperature T_1. In this formulation it is assumed that $\beta L \ll 1$ and that sample losses due to radiation, conduction, and convection are estimated from the thermal decay slope.

In this study samples were exposed to 10 W-30 W, 10.6 μm laser irradiation for periods of 30 to 240 seconds. Using equation 1, the absorption coefficient, β, was determined for each of the samples. The results are shown in Table 1 for as-received samples. Based on the experimental technique utilized, accuracies for β can be expected within $\pm$ 0.0005 cm^{-1}.

Also given in Table 1 are brief summaries and characterizations of the defect structure, determined primarily by TEM analysis and appropriate correlations with infrared microscopy data, as discussed in detail in the previous sections. In all cases, TEM data were obtained on 2 to 5 specimens per sample.

From the data presented, it can be seen that the infrared absorption coefficient increases as a function of increasing defect density. In particular, for samples with large concentrations of In_2Te_3 or $CdCl_2$ precipitate platelets, the infrared absorption is markedly affected. The presence of macroscopic absorption sites, isolated dislocations, and tellurium precipitation regions also exercises a considerable influence on the infrared absorption properties. Samples with the lowest infrared absorption exhibit the lowest defect concentrations and are relatively free of macroscopic ($\geq$ 1 μm) inclusions.

4. Conclusions

In this investigation we have shown that defects in CdTe samples can dramatically alter infrared absorption at 10.6 μm, thereby limiting the attainment of absorption coefficients $< 10^{-4} cm^{-1}$. In contrast to previous studies which have reported on macroscopic structures observed in infrared and optical microscopy, we have obtained systematic data on microstructural defects and their influence on infrared absorption. It has been shown that many of the macroscopic defects ($\gtrsim$ 1 μm) observed are composed of aggregations of precipitate platelets, dislocations, or stacking faults.

Although we have investigated the effects of annealing in Cd vapors, further work is required to identify the effect of sequential annealing in Cd and Te vapors, since it is known that the infrared absorption coefficient can be further reduced by a series of multiple anneals (4). Additional investigation is required, using correlated microstructural analysis and measurements of the infrared absorption coefficient to determine the behavior of microstructural defects after multiple thermal annealing schedules.

References

1. M. Sparks and L. J. Sham, Solid State Comm. 11, 1451 (1972).

2. M. Sparks, Fourth American Society for Testing Materials Symposium on Damage in Laser Materials, Boulder, Colorado, 1972 (unpublished).

3. A. L. Gentile, J. E. Kiefer, N. R. Kyle, and H. V. Winston in Proc. Conference on High Power Laser Window Materials, C. A. Pitha, ed., U.S. Air Force Cambridge Research Laboratories Tech. Report TR-73-0372 (11), Bedford, Mass., 1973 (p. 625).

4. L. R. Shiozawa, D. A. Roberts, and J. M. Jost, in Proc. Conference on High Power Laser Window Materials, C. A. Pitha, ed., U.S. Air Force Cambridge Research Laboratories Tech. Report TR-37-0372(11), Bedford, Mass., 1973 (p. 639).

5. G. E. Kuhl, in Proc. *Conference on* High Power Laser Window Materials, C. A. Pitha, ed., U.S. Air Force Cambridge Research Laboratories Tech. Report TR-73-0372(11), Bedford, Mass., 1973 (p. 607).

6. M. Sparks and C. J. Duthler, J. Appl. Phys. 44, 3038 (1973).

7. T. J. Magee, J. Peng, and J. Bean, Proceedings Electron Microscopy Soc. America, Claitor Publ. Co., Baton Rouge, La., 1974 (p. 548).

8. S. Amelinckx, "The Direct Observation of Dislocations," Academic Press, New York (1964), p. 414.

9. American Society for Testing Materials, X-ray Diffraction Data File, Philadelphia, Pa.

10. D. de Nobel, Philips Res. Reports 14, 361 (1959).

11. G. W. Groves and A. Kelly, Phil Mag. 7, 892 (1962).

12. B. Edmondson and G. K. William, Phil. Mag. 9, 277 (1964).

13. B. Bendow, A. Hordvik, H. Lipson, and L. Skolnik, U.S. Air Force Cambridge Laboratories Tech. Report TR-73-0372, Bedford, Mass., 1973.

14. H. G. Lipson, L. H. Skolnik, and D. L. Stierwalt, in Proc. Third Conference on High Power Infrared Laser Window Materials, C. A. Pitha and B. Bendow, eds., U.S. Air Force Cambridge Research Laboratories, Tech. Report TR-74-0085(1), Bedford, Mass., 1974 (p. 337).

15. L. H. Skolnik, A. Hordvik, and A. Kahan, Appl. Phys. Letters 23, 477 (1973).

TABLE 1. DEFECT CONCENTRATIONS IN CdTe SAMPLES

	DENSITY	SIZE	COMMENTS
In_2Te_3 platelets	10^{14} - $10^{16}/cm^3$	100 - 125 Å	No significant decomposition after anneals $> 500^oC$
$CdCl_2$ platelets	$> 10^{16}/cm^3$	150 Å	
Te precipitates	10^{14} - $10^{16}/cm^3$	60 Å	Decomposition after anneals $\geq 500^oC$
Stacking faults	$> 10^7/cm^2$	> 1 μm in length	Aligned; localized in discrete zones
Dislocation lines	10^5 - $10^8/cm^2$	0.1 μm - 5 μm	Isolated line segments and tangles
Dislocation loops		1000 - 1500 Å	Localized; observed after annealing

TABLE 2 DATA SUMMARY

Sample No.	β (cm^{-1})	Microstructural Characterization
1	.0092	Distributed In_2Te_3 precipitate platelets ($3 \times 10^{16}/cm^3$); localized tellurium segregation regions.
2	.0124	Distributed In_2Te_3 precipitate platelets ($7 \times 10^{16}/cm^3$); tellurium precipitates ($10^{16}/cm^3$) in localized discrete sites.
3	.0290	Macroscopic absorption sites (1 μm-6 μm) composed of complex dislocation networks; In_2Te_3 platelet enrichment zones (absorption sites) - density $> 10^{17}/cm^3$ within sites, vacancy loops.
4	.0012	In_2Te_3 precipitate platelet density low ($\simeq 10^{14}/cm^3$); evidence of slight tellurium precipitation phase; dislocation density low.
5	.0160	$CdCl_2$ precipitate platelets ($10^{16}/cm^3$); high dislocation line density ($> 10^8$ lines/cm^2); stacking faults (localized); vacancy loops (localized).
6	.0065	Distributed In_2Te_3 precipitate platelets ($3 \times 10^{15}/cm^3$); some tellurium precipitation; isolated dislocation lines.
7	.0009	In_2Te_3 precipitate density low ($< 10^{14}/cm^3$); little or no evidence of tellurium precipitation; no detectable dislocations.

List of Figures

Fig. 1 *Transmission electron micrograph* and diffraction pattern of indium-doped CdTe sample. In_2Te_3 precipitate platelets are observed in distributed regions throughout the sample.

Fig. 2 Transmission electron micrograph of chlorine-doped CdTe sample illustrating the presence of aligned stacking faults.

Fig. 3 Transmission electron micrograph obtained on indium-doped CdTe sample containing macroscopic absorption sites.

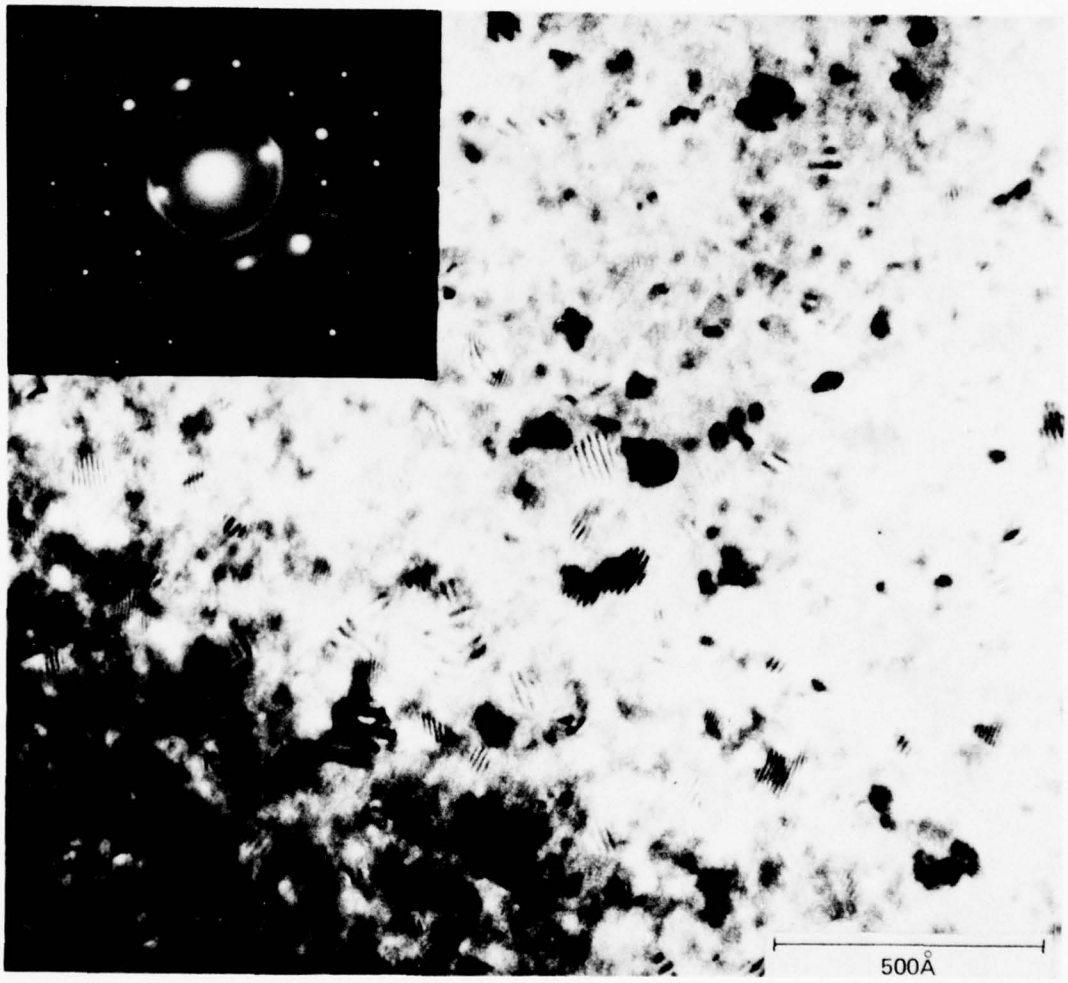
500Å

MP-2266-15

MA-2266-16

APPENDIX G

PREPRINT

"LASER INDUCED STRESSES IN COATED AND UNCOATED TARGETS"

By

T. J. Magee, R. A. Armistead, and P. Krehl

(Accepted for publication in
Journ. Physics (D): Appl. Physics 8, 498 1975)

Laser Induced Stresses in Coated and Uncoated Targets[1]

by

T. J. Magee, R. A. Armistead, and P. Krehl[2]
Poulter Laboratory, Stanford Research Institute,
Menlo Park, California 94025

Abstract. A number of experiments were conducted with a pulsed Nd:glass laser to assess the effect of thin coatings with varying optical properties on laser coupling and stress wave generation in aluminum targets. The coatings included liquid cement, which is transparent at 1.06 μm; Aquadag, which is opaque; and silver paint, which ranges from translucent to opaque, depending upon the curing time. Considerable stress enhancement was found for the transparent plasma-confining coatings and the partially cured silver paint, which was semitransparent and contained a volatile binder. Stress levels for untreated aluminum and samples with Aquadag or cured silver paint coatings varied approximately with the coupling coefficient for these materials. The potential ramifications of these results to laser-fusion experiments are discussed.

1) Research supported in part by AFOSR Contract No. F44620-73-C-0019

2) Post-Doctoral Fellow; present address: Ernst Mach Institut, Freiburg, Germany

1. Introduction

A number of recent investigations have demonstrated that pulsed laser irradiations of materials produce stress waves that can be appropriately monitored at the back surface of the sample (O'Keefe and Skeen 1972, 1973, Anderholm 1970, Fox 1974, Yang 1974). In these experiments the materials were either unconfined, confined between two transparent materials, or coated with a thin, normally transparent film. In the first case, the plasma produced at the surface of the material during laser irradiation is responsible for the generation of the stress wave. In the second configuration, a confined, high temperature plasma is produced, which drives high amplitude stress waves into the transparent materials (Anderholm 1970, Yang 1974). Using the third technique, thin coatings are partially decomposed and vaporized as a result of thermal conduction from the laser-heated metal surface. The subsequent expansion of the gas and partial confinement of the plasma at the metal/thin-film interface causes stress waves to be generated in the substrate (O'Keefe and Skeen 1972). In all cases, previous investigations have been concerned with laser irradiation of relatively thin foils of thicknesses typically in the order of several micrometers. The focal spot area has also been varied in the past to systematically obtain higher power densities. However, this introduces the possibility that the data may be complicated by spot size effects, especially for laser exposures in air. Experiments by J. Lowder (1973) at MIT Lincoln Laboratories, for example, have suggested a dependence of the peak stress level on laser spot size. Stress levels measured at the rear surface of Plexiglas targets irradiated in air by a 20 microsecond CO_2 laser pulse ($E \leq 50$ joules) increased several fold for a given power level as the spot size was increased from 0.32 cm^2 to 0.8 cm^2.

In the present study, thick ($\geq$ 2 mm) aluminum targets have been irradiated with 25 nanosecond pulses from a Nd: glass laser and the stress histories monitored at the back surface of the material with x- cut quartz piezoelectric gages. Experiments have been conducted on untreated aluminum and samples coated with thin transparent, translucent, and opaque layers. In all cases the focal spot size was held constant and the laser power changed to provide varying intensity levels at the sample surface.

2. Experimental

The experimental arrangement is shown in Fig. 1. The laser used in these studies was a Q-switched Korad K- 1500 oscillator - amplifier neodymium system with an output ranging from 2 to 12.5 joules. The pulse width at half-peak power was 25 nanoseconds. The 1.9-cm beam diameter was focused by a 600-mm focal length lens through a quartz plate 10-mm thick into a chamber maintained at a vacuum of approximately 10^{-4} torr. The power-time history of the laser pulse was detected by a calibrated biplanar photodiode in conjunction with a Tektronix 7704 oscilloscope and the energy determined by integrating the signal over the pulse duration. The photodiode signal was displayed together with the quartz gage signal on a second oscilloscope for time referencing.

A Sandia-type quartz gage (Graham et al. 1965, Halpin et al. 1963, Jones and Halpin 1968) was fabricated for monitoring stress-time records at the rear of the targets. The quartz gage element (Valpey Corp.) was 1 cm. in diameter, 1 mm. in thickness and had a guard ring at the edge of the element. Using a 50 ohm shunt resistor, the sensitivity of the gage was 1.09 mV/bar. The propagation time for the sound pulse in the quartz was 174 nanoseconds and long compared to the half-width of the laser pulse (25 nanoseconds). To ensure that a pulse reflected at the

rear surface of the sample would not reach the gage during the loading phase, thicknesses of target samples, d_s, had to satisfy the condition:

$$d_s > 174 \text{ nsec.} \frac{v_s}{2} ,$$

where v_s is the velocity of sound in the sample.

Targets were prepared from 10-mm diameter, 1145-aluminum disks ($\simeq$ 2 mm in thickness) and subsequently mounted on the electrode of the quartz gage with a thin epoxy layer. Although mineral oil (Fox, 1974) and stopcock grease (O'Keefe and Skeen, 1972) have been used in the past to mount target materials to the gage, it was found that inhomogeneities in these mounting mediums could cause improper coupling between the gage and the target and result in error in the measured stress. A very thin epoxy layer was found to give the best stability and acoustic matching. After mounting, the samples were placed on a rigid stand within the vacuum chamber and aligned so that the face of the target was normal to the optical axis of the laser beam. In all experiments the laser spot size was slightly greater than the target diameter (1 cm) to ensure essentially uniaxial stress conditions.

Bare aluminum samples and samples coated with Aquadag (Acheson Colloids Co.), silver paint (Walsco No. 36-1), and nitrocellulose liquid cement (Duratite Corp.) were irradiated with 1.06 μm laser light. In esch case the films were applied uniformly to a thickness of $\simeq$ 60 μm and subsequently dried for variable periods. Before and after all irradiations, samples were examined with scanning electron and optical microscopy to determine the relative degree of surface modification.

3. Results

Fig. 2 shows a portion of a typical oscilloscope record illustrating the quartz gage signal obtained from an irradiated 2 mm thick aluminum sample coated with silver paint and cured for five minutes. The laser energy was 5 joules and the active irradiation area, 0.8 cm^2. The propagation time of the stress wave from the front to the back surface of the target was 317 nanoseconds (V_s = 6300 m/sec, Kinsler and Frey, 1962) resulting in a time separation between the laser (photodiode) signal and the stress signal. In all experiments, the time correlation between the initiation of laser firing and the onset of gage recording agreed well with the propagation time of the stress wave through the aluminum sample.

Data obtained for untreated aluminum samples and those containing various surface coatings are compared in Figs. 3 and 4. It can be observed that the amplitude of the stress wave can be substantially enhanced when coatings are included on the surface. The maximum enhancement of stress by these coatings occurs at the lower laser energies, while at higher energies the effect of the coatings diminishes and the stress-fluence curves appear to be approaching an asymptotic value, suggesting a saturation limit.

An examination of the stress-fluence curves for uncoated and Aquadag-coated samples reveals that the peak stress is enhanced by a factor of two for the coated samples irradiated at lower laser fluences. Since the graphite acts as an absorbing layer, a greater amount of laser energy will be coupled into the coated targets. Lowder (1974) found in laser calorimetry experiments that the ratio of the 10.6 μm laser coupling coefficients for graphite and aluminum was approximately 2 to 1. In this case, the coupling coefficient is defined as the fractional amount of laser energy converted into thermal energy within the material. Using

the same techniques and an appropriate correction factor for the equilibration temperature (Gilbert and Carson 1972) we found a similar ratio for samples irradiated at 1.06 μm. Comparing these results with the stress-fluence curves of Fig. 3, it can be seen that the stress enhancement factor for Aquadag coated samples irradiated in the lower laser fluence range is approximately proportional to the ratio of the coupling coefficients for graphite and aluminum.

In the higher fluence range, the effect of the Aquadag coating is effectively diminished. Recent experiments by Rudder (1974) on aluminum and graphite targets irradiated by a 1 μsec. 1.06 μm laser pulse have shown that, at levels above 3×10^8 W/cm^2, there is only a negligible difference between the impulse delivered to the two targets, while there is a somewhat greater momentum transfer to the graphite at levels below 1.5×10^8 W/cm^2. Although the previous experiments cannot be directly compared with those of the present study the results obtained support the concept of an "apparent" material independent coupling for opaque materials irradiated at higher laser energies. This can be ascribed to the formation of a dense absorbing plasma at high laser energies that effectively shields the surface during irradiation, resulting in the observed saturation of stress at higher laser fluences.

Referring to Fig. 3, it can be noted that increasing the drying time of silver paint coatings decreases the magnitude of laser induced stress. To investigate the influence of drying time on the magnitude of stress enhancement, a glass slide was coated with thin films of silver paint and allowed to dry for variable periods. The silver paint used in these experiments is composed of silver colloids suspended in a transparent butyl acetate solution. Spectrophotometric measurements indicated that the silver paint layer was approximately 40% transmitting at 1.06 μm when the layer was dried for a period of 5-10 minutes, whereas after 48

hours, the layer was completely opaque due to the evaporation of all of the butyl acetate binder. Scanning electron micrographs indicated that the remaining silver colloids formed a loosely packed continuous layer on the surface of the aluminum. Quartz gage records showed that the measured stress was approximately within the range of values recorded for uncoated aluminum, which is to be expected since the coupling coefficients of the silver layer and aluminum should be comparable.

For a curing time of five minutes, the induced stress was increased relative to the uncoated sample or samples with a fully cured silver paint layer by a factor of 2-3 in the lower fluence range. Fox (1974) reported on the enhancement of stress in irradiated aluminum targets coated with a black paint layer, but did not consider the influence of volatile binders within the layer on stress enhancement. O'Keefe and Skeen (1972) found that when an RTV adhesive layer was allowed to dry for longer periods of time, the stress also decreased. These results suggest that a portion of the stress is generated by high pressure gas produced by the partial decomposition of the volatile transparent binder, in addition to the effect caused by trapping of the high temperature plasma at the aluminum-coating interface. At higher laser fluences the degree of stress enhancement arising from the partially cured silver paint layer is reduced. It appears likely that at high energies the coating becomes essentially opaque due to the presence of a plasma formed at the silver colloids and vaporization of the butyl acetate binder.

The most notable enhancement in laser-induced stress occured for aluminum samples coated with a thin transparent liquid cement layer (Fig. 4). For a sample subjected to 11.75 joules/cm^2 (4.7 x 10^8 W/cm^2) the maximum stress was 5.3 kbar. For untreated aluminum samples, irradiated at approximately the same flux level, the stress was 0.88 kbar. At lower flux levels, the stress enhancement factor is even more pronounced,

approaching a value of ten at 5 joules/cm^2. In similar experiments on laser-irradiated aluminum targets, O'Keefe and Skeen (1972) reported a stress of 0.47 kbar for uncoated aluminum and a stress of 7.9 kbar for aluminum coated with liquid cement at a flux of 91 joules/cm^2. Their data, however, suggest that a stress saturation value is reached at much lower fluence levels. In the present study a stress of 5.3 kbar was measured at a flux of 11.75 joules/cm^2, and the saturation limit had not been attained. The significant variation between our experiments and those reported by O'Keefe and Skeen was in the laser focal spot size. In all the current experiments the spot size remained constant and was approximately 4-5 times larger than that used in the previous study.

Experiments were also conducted on untreated and liquid cement-coated samples maintained under vacuum conditions and exposed to air. Fox (1974) recently reported that the laser induced stress was reduced for samples irradiated in the air, but did not present comparative data on samples maintained under both exposure conditions. The present data indicates that at fixed laser irradiation levels (2.4×10^8 W/cm^2 - 3.2×10^8 W/cm^2), the amplitude of the induced stress was approximately 20-40 percent higher in the samples exposed under vacuum conditions than in those exposed to air. Stress enhancement on coated samples was noted under both exposure conditions, but the degree of enhancement was reduced for samples exposed to air.

4. Conclusions

The results of these experiments have demonstrated that the amplitude of laser-induced stresses in aluminum targets can be enhanced by including transparent, translucent, and opaque coatings at the surface of the material. The magnitude of the stress enhancement factor for targets containing an opaque absorbing layer is roughly proportional to the ratio of laser coupling coefficients for the coating and substrate. Significant

stress enhancement was noted when a transparent or translucent volatile plasma confining coating was included on the target surface. In comparative experiments on samples maintained under a vacuum and exposed to air it has been shown that the magnitude of peak stress recorded for samples irradiated in air is significantly smaller than that obtained for vacuum-irradiated samples.

Previous investigators have suggested applications of the enhancement of peak pressures by the presence of thin-film coatings. O'Keefe and Skeen (1972) reported that these techniques could be used to load complex geometries and, in fact, used the technique to test the bond strength of electronic components Yang (1974) investigated the applicability of enhanced stress from confined thin films for the detonation of insensitive explosives.

We, however, would like to suggest the possibility that stress enhancement by the application of selected coatings could be used advantageously in laser fusion studies. In these experiments fuel pellets must be imploded by blow-off momentum transfer to reach densities 10^3 to 10^4 times the solid state density. For essentially opaque materials, like LiD, transparent thin film coatings could be applied directly to the surface. Other targets, like DT, are largely transparent in the 1.06 - 10.6 μm range. However, a number of laboratories are currently investigating the use of opaque coatings on fuel pellets to prevent preheating of the center of the pellet during irradiation (Holzrichter 1974). Consequently, a second transparent layer could be applied to achieve stress enhancement. Since the laser energies and pulse durations used differ markedly from laboratory investigations conducted to date on small metallic targets, experiments should be performed to determine the effects of single coatings and stacked layers in typical experimental configurations used in laser fusion studies.

The authors would like to acknowledge the assistance of F. Schwirzke of the Naval Post Graduate School in Monterey, California, during the performance of these experiments.

References

1) N. C. Anderholm, 1970, Appl. Phys. Lett. 16, 113-115.

2) J. A. Fox, 1974, Appl. Phys. Lett. 24, 461-464.

3) K. G. Gilbert and R. L. Carson, 1972, U.S. Air Force Weapons Laboratory Rpt. TR-72-168.

4) R. A. Graham, F. W. Neilson, and W. B. Benedick, 1965, J. Appl. Phys. 36, 1775-1783.

5) W. J. Halpin, O. E. Jones, and R. A. Graham, 1963, ASTM Special Publ. No. 336.

6) J. F. Holzrichter, 1974, Lawrence Livermore Laboratory, Livermore, California (private communication).

7) G. A. Jones and W. J. Halpin, 1968, Rev. Sci. Instr. 39, 258-259.

8) J. Lowder, 1973, Proc. Laser Effects/Laser Hardening Conf. Naval Postgraduate School, Monterey, Calif.

9) J. Lowder, 1974, MIT Lincoln Labs, Massachusetts (private communication).

10) J. D. O'Keefe and C. H. Skeen, 1972, Appl. Phys. Lett. 21, 464-466.

11) J. D. O'Keefe, C. H. Skeen, and C. [redacted] York, 1973, J. Appl. Phys. 44, 4622-4626.

12) L. E. Kinsler and A. R. Frey, 1962, "Fundamentals of Acoustics," (John Wiley, New York), 502-503.

13) R. R. Rudder, 1974, U.S. Air Force Weapons Laboratory Rpt. TR-74-100.

11) L. C. Yang, 1974, J. Appl. Phys. 45, 2601-2608.

List of Figures

Fig. 1. Schematic of experimental configuration.

Fig. 2. Reproduction of a quartz gage/oscilloscope stress-time history record. The laser energy was 5 joules and the active irradiation area, 0.8 cm^2. The sample was coated with silver paint and cured for 5 minutes. The maximum stress was 0.89 kbar.

Fig. 3. Laser induced stresses in coated and uncoated aluminum samples as a function of laser energy density. In all experiments the active laser irradiation area was 0.8 cm^2.

Fig. 4. Laser induced stresses in liquid cement coated aluminum samples as a function of laser energy density. The active laser irradiation area was 0.8 cm^2.

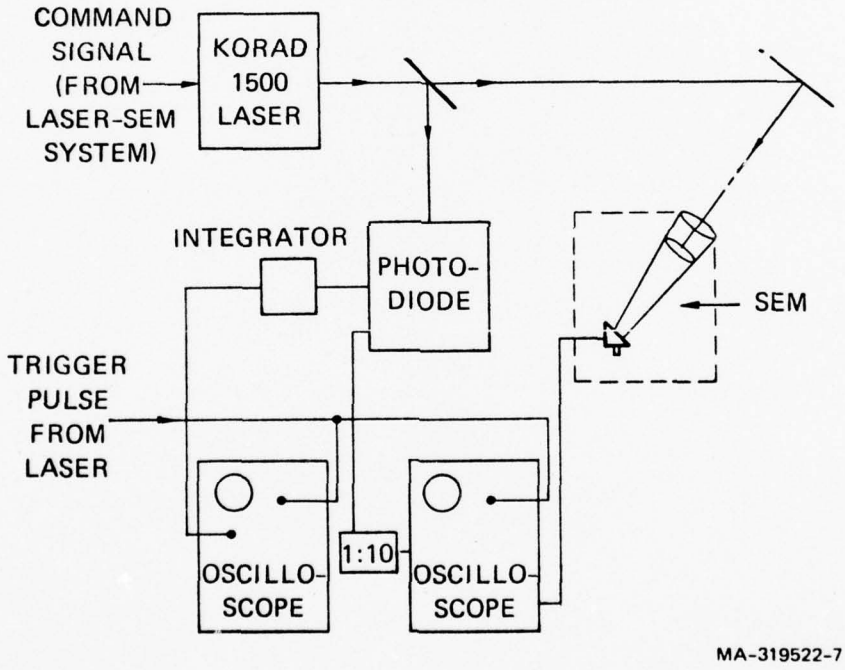
COMMAND
SIGNAL
(FROM
LASER-SEM
SYSTEM)
KORAD
1500
LASER
INTEGRATOR
PHOTO-
DIODE
SEM
TRIGGER
PULSE
FROM
LASER
OSCILLO-
SCOPE
1:10
OSCILLO-
SCOPE
MA-319522-7

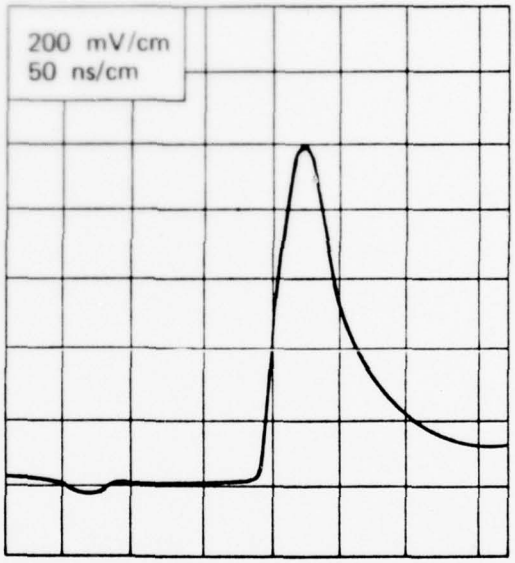

MP-319522-17

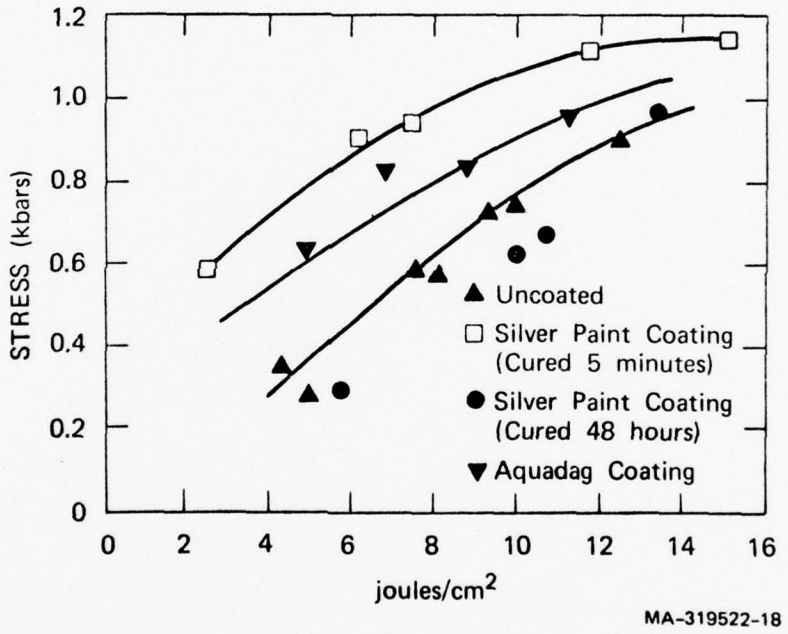
1.2
1.0
0.8
0.6
0.4
0.2
0
STRESS (kbars)
0
2
4
6
8
10
12
14
16
joules/cm2
Uncoated
Silver Paint Coating (Cured 5 minutes)
Silver Paint Coating (Cured 48 hours)
Aquadag Coating
MA-319522-18

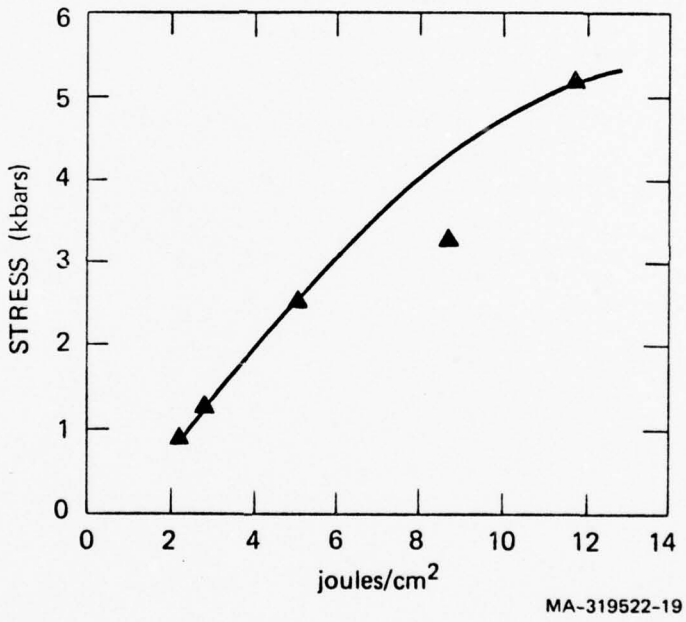
STRESS (kbars)
0
1
2
3
4
5
6
0
2
4
6
8
10
12
14
joules/cm2
MA-319522-19

APPENDIX H

"LASER DAMAGE PHENOMENOLOGY IN MATERIALS"

By

R. A. Armistead and T. J. Magee

(to be published in "Laser Interaction and Related Plasma Phenomena," ed. by H. Hora and H. J. Schwartz Plenum Publ. Corp., New Y

LASER DAMAGE PHENOMENOLOGY IN MATERIALS*†

R. A. Armistead** and T. J. Magee**

Stanford Research Institute

333 Ravenswood Avenue, Menlo Park, CA 94025

INTRODUCTION

Improvements in laser technology must be accompanied by concomitant improvements in optical materials. The presence of both macroscopic and microscopic defects contribute significantly to the evolution of damage in optical components. It is well known that macroscopic defects such as scratches, polishing pits, and inclusions at the surface of a material will tend to scatter incident light from the sample. Absorption and local heating will occur at cavities or near inclusions of varying dielectric constant, often resulting in catastrophic surface breakdown or bulk material failure. The presence of microscopic defects such as vacancies, interstitials, or "impurities" in a crystal may affect the absorption of light by causing a local perturbation of the lattice spectrum. Larger defects such as dislocations, voids, inclusions, and grain boundaries often serve as scattering centers or absorbers, depending upon dimensions, charge configuration, the wavelength of light, and the relative absorption efficiencies. Other defects, introduced either during material growth or as a result of exposure to ionizing radiation (e.g., electronic traps, color centers, impurity-vacancy pairs) can substantially affect absorption in both the visible-UV region and the infrared region of the spectrum.

---

*Presented at the Fourth Workshop on "Laser Interaction and Related Plasma Phenomena" held at RPI, Troy, New York, November 8-12, 1976.

AD-A037 163 STANFORD RESEARCH INST MENLO PARK CALIF F/G 20/5
LASER DAMAGE PHENOMENA IN MATERIALS.(U)
NOV 76 T J MAGEE, J PENG, R A ARMISTEAD F44620-73-C-0019
UNCLASSIFIED AFOSR-TR-77-0155 NL

2 OF 2
AD A037163

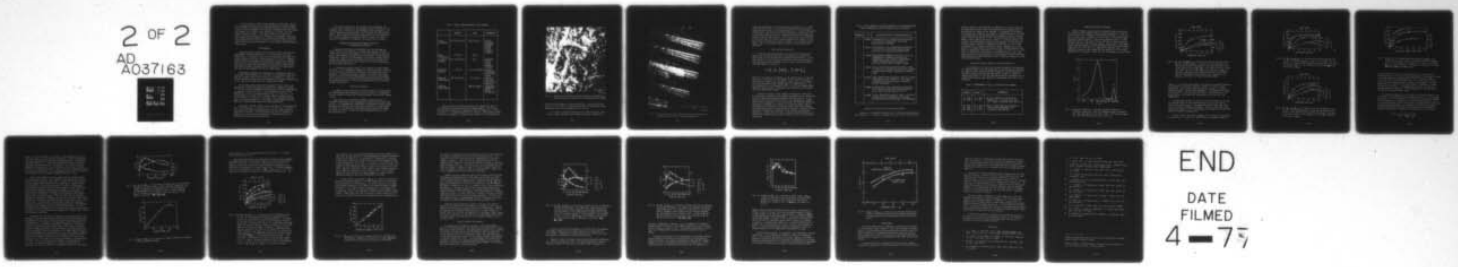

END
DATE FILMED
4-77

If laser-induced nuclear fusion becomes an operational reality, it is necessary not only that optical materials be further improved, but also that the transient and long-term effects of ionizing radiation on optical components be carefully considered since the working environment will include x-rays, gamma rays, neutrons, and high-energy charged particles. This paper presents the results of a series of investigations on the influence of microscopic defects on the infrared optical properties of selected semiconductor high-power laser window materials and the effects of ionizing radiation on the visible-UV and infrared absorption of alkali halide and semiconductor laser windows.

EXPERIMENTAL

Cadmium telluride samples used in these studies were obtained from Hughes Research Laboratories, II-VI Corporation, and Tyco Laboratories. The samples were of (111) orientation and doped with either indium or chlorine to concentrations $\geq 10^{17}$ cm^{-3}. Chemical-vapor-deposited ZnSe samples were provided by the Raytheon Company. Single crystal and polycrystalline mixed KCl samples were obtained from either Harshaw Chemical Company or the Honeywell Corporation. The mixed KCl samples included (1) KCl alloyed with 5 mol% RbCl or KBr, and (2) KCl alloyed with 0.05 to 1 mol% $EuCl_2$.

Semiconductor samples were prepared for transmission electron microscope (TEM) examination in the form of 3-mm diameter disks that were jet-thinned from the back surface of the sample.[1,2] Data obtained from TEM analyses were then correlated with gross macrostructural (≥ 1 μm) defects observed in an infrared microscope.

Conventional laser calorimetry techniques[3-5] were used to determine the infrared absorption coefficients of samples of volume ≥ 1 cm^3 and a newly developed microcalorimeter[2] used for measurements on samples of volume < 0.5 cm^3. The corresponding error in the measurement of β at 10.6 μm determined to be $\pm 1 \times 10^{-5}$ cm^{-1}. In all experiments, we used a 50-W Coherent Radiation (Model 42) CO_2 laser focused at the center of the sample face. Separate measurements of infrared absorption in the 2-μm to 15-μm regions were also made with a Perkin-Elmer (Model 247) spectrophotometer.

In separate studies, samples were irradiated at room temperature with 1-MeV electrons at a dose rate of 3.3×10^5 R/sec. A Hg lamp and a Bausch and Lomb monochromator were used for simultaneous illumination of samples. An electromechanical shutter, switched in sequence with the electron beam shutter, provided control of illumination during electron irradiation.

After each irradiation, the infrared laser absorption coefficients were determined for all samples by laser calorimetry. Absorption spectra from alkali halide samples were monitored in the visible and near-infrared regions with a Beckman DK-2 spectrophotometer. Postirradiation bleaching experiments were also conducted on a number of samples by exposing them to F-light (0.55 μm) at levels of 400 $\mu W/cm^2$ to 500 $\mu W/cm^2$ for periods from 1 to 600 s.

MICROSCOPIC DEFECTS AND INFRARED ABSORPTION IN SEMICONDUCTOR WINDOWS

Cadmium telluride and zinc selenide have been proposed as window materials in high-power infrared laser systems. Both materials have offered some promise in this area because of their superior thermomechanical properties and resistance to environmental influences. However, the development of laterally uniform, large-surface-area samples exhibiting spatially invariant infrared absorption coefficients β, as low as 10^{-4} cm^{-1} in the 10.6-μm range, has often posed difficulties.

It has been previously shown[6,7] for a number of laser window materials that the exponential changes in β as a function of frequency were intrinsic and could be related to multiphonon absorption processes. Theoretical analyses, however, show that only a small portion of the observed 10.6-μm absorption in CdTe or ZnSe samples can be related to an intrinsic absorption mechanism and that native and secondary defects are inevitably responsible for the increased infrared absorption.[8]

CdTe Defect Analysis

A summary of data obtained from TEM analyses of over 500 indium- and chlorine-doped CdTe specimens is given in Table 1. Representative micrographs illustrating the microstructure are shown in Figures 1 and 2.

Identification of precipitate platelet composition was established unequivocably from transmission electron diffraction (TED) patterns. In complementary experiments, we measured the Moire fringe spacingsand determined the lattice plane spacings on a large number of platelets; the resulting values consistently agreed with values for In_2Te_3 and $CdCl_2$, thereby providing supplementary data to the TED identification.

Table 1 DEFECT CONCENTRATIONS IN CdTe SAMPLES

	DENSITY	SIZE	COMMENTS
In_2Te_3 PLATELETS	10^{14} TO $10^{16}/cm^3$	100 TO 125 Å	NO SIGNIFICANT DECOMPOSITION AFTER ANNEALS $> 500°C$
$CdCl_2$ PLATELETS	$> 10^{16}/cm^3$	150 Å	
Te PRECIPITATES	10^{14} TO $10^{16}/cm^3$	60 Å	DECOMPOSITION AFTER ANNEALS $\geq 500°C$
STACKING FAULTS	$> 10^7/cm^2$	$> 1\mu m$ IN LENGTH	ALIGNED: LOCALIZED IN DISCRETE ZONES
DISLOCATION LINES	10^5 TO $10^8/cm^2$	0.1 TO $5\mu m$	ISOLATED LINE SEGMENTS AND TANGLES
DISLOCATION LOOPS		1000 TO 1500 Å	LOCALIZED: OBSERVED AFTER ANNEALING

Polycrystalline tellurium rings have been observed in many of the diffraction patterns obtained from doped samples. The Te precipitates have been directly observed by TEM and found to be $\simeq 60$ Å in diameter. In samples annealed in Cd vapors at temperatures $\geq 500^{o}C$, there was no evidence of Te precipitation either in the transmission

Fig. 1. Transmission electron micrograph showing the presence of complex dislocation tangles in an indium-doped CdTe sample

electron micrographs or diffraction patterns. Since the melting point of Te is < 500°C, it seems likely that the precipitates have decomposed and Te has diffused into the lattice.

In a number of samples examined by infrared microscopy, small (2 μm to 4 μm) absorption sites appeared granular, suggesting

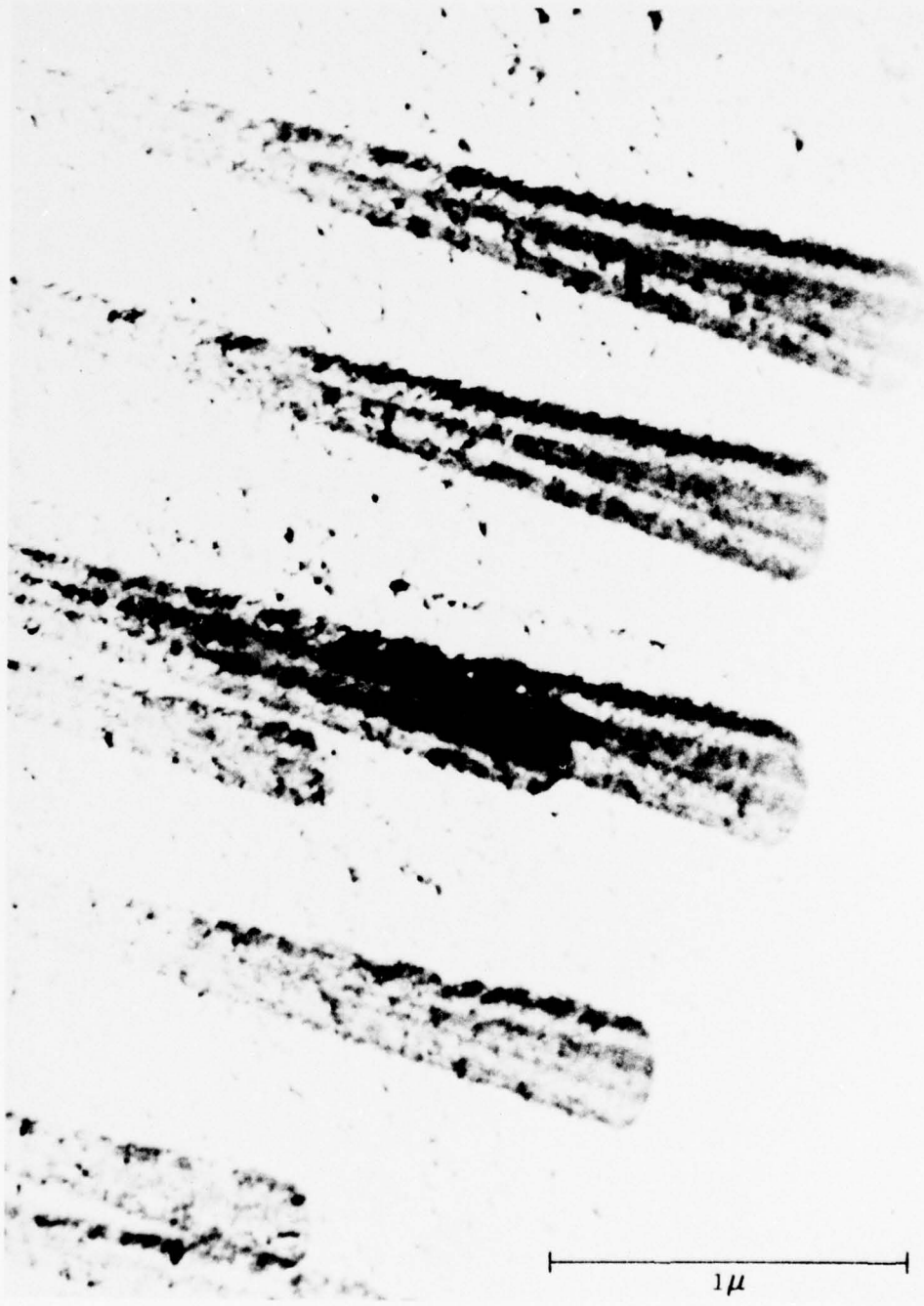

Fig. 2 Transmission electron micrograph showing the presence of aligned stacking faults in chlorine-doped CdTe

nonuniform absorption or scattering within the defect site. These sites have been shown to be associated with preferential damage or "burn-through" regions at high-power densities. To obtain additional information on the structure of these macroscopic absorption sites, we sectioned samples within the absorption regions and subsequently prepared them for TEM analysis. In all cases, the sites were shown to be associated with distinct defect aggregations, namely (1) complex arrays of dislocation lines and tangles, (2) aligned stacking faults, and (3) localized regions of In_2Te_3 on $CdCl_2$ precipitate platelets.

CdTe Infrared Absorption

To provide correlation between the observed microstructural defects and infrared transmission, we determined the absorption coefficient at 10.6 μm from laser calorimetry measurements. It has been shown[2-5] that the absorption coefficient β can be determined from the thermal rise and decay rates of laser irradiated targets. The approximation is given by:

$$\beta = \frac{MC_p}{LP_t} \frac{2n}{n^2+1} \left(\left. \frac{dT_{rise}}{dt} \right|_{T_1} + \left. \frac{dT_{decay}}{dt} \right|_{T_1} \right)$$

where M is the mass of the sample, C_p the specific heat at constant pressure, L, the length of the sample, P_t the transmitted power, n, the refractive index, and $dT_{rise}/dt/T_1$ $dT_{decay}/dt/T_1$, the temperature rise and decay rates, respectively, at temperature T_1. In this formulation it is assumed that $\beta L \ll 1$ and that sample losses resulting from radiation, conduction, and convection are estimated from the thermal decay slope.

In Table 2 we give a brief summary of absorption coefficient data obtained on representative samples correlated with microstructural defect characterizations determined from TEM analysis. In all cases, TEM data were obtained on two to five specimens per sample. From the data presented, it can be seen that the infrared absorption coefficient increases as a function of increasing defect density. The presence of macroscopic absorption sites, dislocation tangles, tellurium precipitates, In_2Te_3 and $CdCl_2$ platelets, and other defects exercises a considerable influence on the absorption properties. Conversely, samples with the lowest infrared absorption exhibit the lowest defect concentrations and are relatively free of macroscopic inclusions.

Table 2 DATA SUMMARY FOR SAMPLES CORRELATED WITH MICROSTRUCTURAL DEFECT CHARACTERIZATIONS DETERMINED FROM TEM ANALYSIS

SAMPLE	β (cm^{-1})	MICROSTRUCTURAL CHARACTERIZATION
1	0.0092	DISTRIBUTED In_2Te_3 PRECIPITATE PLATELETS ($3 \times 10^{16}/cm^3$); LOCALIZED TELLURIUM SEGREGATION REGIONS
2	0.0124	DISTRIBUTED In_2Te_3 PRECIPITATE PLATELETS ($7 \times 10^{16}/cm^3$); TELLURIUM PRECIPITATES ($10^{16}/cm^3$) IN LOCALIZED DISCRETE SITES
3	0.0290	MACROSCOPIC ABSORPTION SITES (1 TO 6 μm) COMPOSED OF COMPLEX DISLOCATION NETWORKS; In_2Te_3 PLATELET ENRICHMENT ZONES (ABSORPTION SITES), DENSITY $> 10^{17}/cm^3$ WITHIN SITES, VACANCY LOOPS
4	0.0012	In_2Te_3 PRECIPITATE PLATELET DENSITY LOW ($\approx 10^{14}/cm^3$); EVIDENCE OF SLIGHT TELLURIUM PRECIPITATION PHASE; DISLOCATION DENSITY LOW
5	0.0160	$CdCl_2$ PRECIPITATE PLATELETS ($10^{16}/cm^3$); HIGH DISLOCATION LINE DENSITY ($> 10^8$ lines/cm^2); STACKING FAULTS (LOCALIZED; VACANCY LOOPS (LOCALIZED)
6	0.0065	DISTRIBUTED In_2Te_3 PRECIPITATE PLATELETS ($3 \times 10^{15}/cm^3$); SOME TELLURIUM PRECIPITATION; ISOLATED DISLOCATION LINES
7	0.0009	In_2Te_3 PRECIPITATE DENSITY LOW ($< 10^{14}/cm^3$); LITTLE OR NO EVIDENCE OF TELLURIUM PRECIPITATION; NO DETECTABLE DISLOCATIONS

ZnSe Defect Analysis and Infrared Absorption

Similarly, we performed TEM analyses of chemical-vapor-deposited ZnSe samples. In a number of samples, distinct visible scatter bands

could be observed, and annealing the samples in Zn or Se vapors did not appreciably reduce either the concentration or apparent size of particles within these scatter regions. To determine the influence of microdefects in ZnSe on the effective infrared absorption, we used a microcalorimeter[2] and measured $\beta_{10.6}$ on samples of cross sectional area $\simeq 0.09$ cm^2 and length ≤ 4 cm. The results obtained on a select number of ZnSe samples are shown in Table 3. The data indicate that visibly clear ZnSe samples, displaying no apparent scatter sites or turbidity zones, exhibit an absorption coefficient $< 2 \times 10^{-3}$ cm^{-1}, in agreement with results obtained by others. Samples with a high density of internal defects or marked turbidity banding exhibited an effective absorption coefficient in the range 2.6×10^{-3} to 4.3×10^{-3} cm^{-1}, in proportion to the density of internal scatter sites. TEM examination of sectioned portions of these samples revealed submicron-sized segregations and dislocation nests in selected regions or within visible scatter zones.

Radiation-Induced Changes in Infrared Absorption

An abundance of literature is available regarding the influence of ionizing radiation on the properties of selected optical materials, but reports on the radiation-induced changes in infrared absorption have been limited. In the past five years, however, a number of studies have shown[9-12] that the 10.6-μm absorption coefficient can be altered significantly upon exposure to high-energy electron or x irradiation.

Table 3 MEASUREMENTS OF $\beta_{10.6}$ ON SELECTED ZnSe SAMPLES

SAMPLE	$\beta_{10.6}$(cm^{-1})	COMMENTS
(1) ZnSe	1.7×10^{-3}	$\beta_{10.6}$ also measured on bulk samples by Raytheon Co. in the range $1\text{-}2 \times 10^{-3}$ cm^{-1}; density of apparent scatter sites low.
(2) ZnSe	1.9×10^{-3}	
(3) ZnSe	2.6×10^{-3}	Density of visible scatter sites moderate to high; submicron segregations of Zn identified by TEM and TED.
(4) ZnSe	3.1×10^{-3}	
(5) ZnSe	4.3×10^{-3}	

Undoped and Mixed KCl Samples

Figure 3 shows a typical optical absorption spectra obtained on a mixed KCl-RbCl sample illustrating the presence of F- and M-centers after a 4-s irradiation with 1-MeV electrons at a dose rate of 3.3×10^5 R/sec. Figures 4 to 6 show the F- and M-center peak absorption coefficients as a function of exposure time to a 1-MeV electron beam at a dose rate of 3.3×10^5 R/s for polycrystalline KCl-KBr, KCl-RbCl, and KCl-$EuCl_2$ samples, respectively. Also shown is the induced change in the 10.6-μm absorption coefficients $\Delta\beta_{10.6}$ ($(\beta_{10.6})0 \simeq 8 \times 10^{-4}$ cm^{-1}) as a function of exposure time. A comparison of Figures 4 and 6 shows that the behavior of the F-center absorption as a function of dose for all the samples is qualitatively

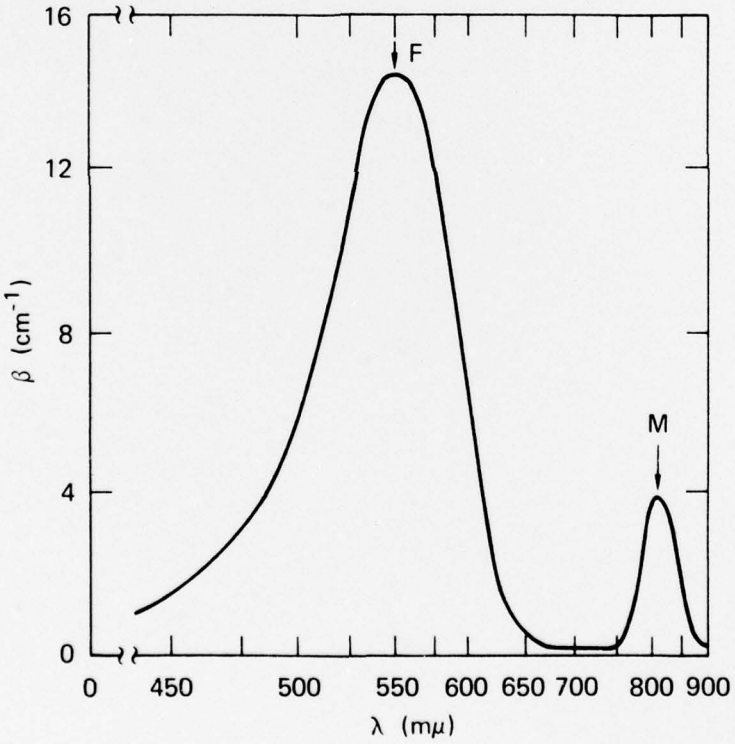

Fig. 3 Absorption spectra of a KCl-RbCl sample following a 4-s electron irradiation. Both the irradiation and the measurement were performed in the dark at 25°C. The electron energy was 1 MeV and the dose rate, 3.3×10^5 R/S.

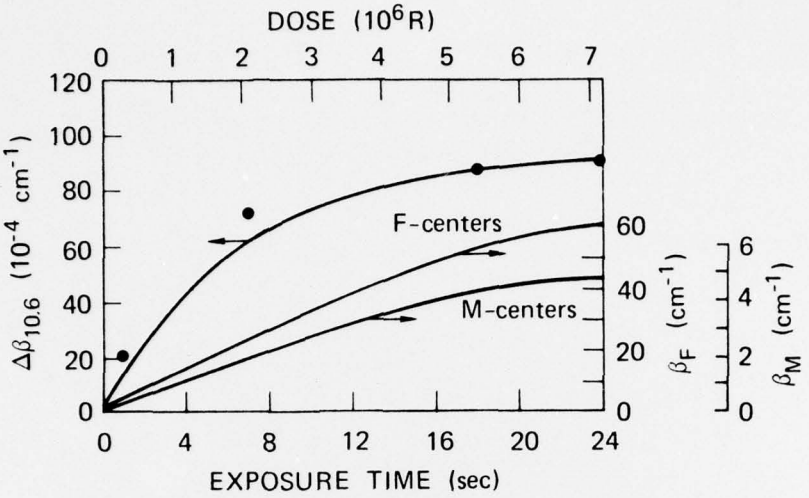

Fig. 4 β_F, β_M, and $\Delta\beta_{10.6}$ as a function of electron exposure time at 25°C in KCl-KBr samples. The scales on the right show the absorption constants determined at the peak position of the F-band (β_F) and the M-band (β_M). The scale on the left shows the change in the 10.6-μm absorption coefficient, $\Delta\beta_{10.6} = (\beta_{10.6})_f - (\beta_{10.6})_0$, where $(\beta_{10.6})_f$ represents the value of the 10.6-μm absorption coefficient after irradiation and $(\beta_{10.6})_0$, the value for the unirradiated sample.

similar. In the lower dose ranges, the absorption increases linearly, with apparent saturation occurring at doses $> 3 \times 10^6$ R. Correespondingly, the M-center absorption and the change in 10.6-μm absorption exhibit a similar dose dependence. In agreement with previous studies[13-15], the coloration rate for F- and M-centers in the mixed crystals was found to be considerably lower than that for undoped KCl.

A comparison was made of calculated F-center densities, N_F, and the induced change in the absorption coefficient at 10.6 μm as a function of electron dose. The comparison did not show that there was a correlation between N_F and $\beta_{10.6}$. Similar results have been reported by Lipson et al.[16] from studies of low-dose-rate (2.8×10^2 R/sec)γ-irradiated (undoped) KCl.

Figure 7 shows the change in $\Delta\beta_{10.6}$ as a function of increasing M-center density. These data indicate that the induced change in

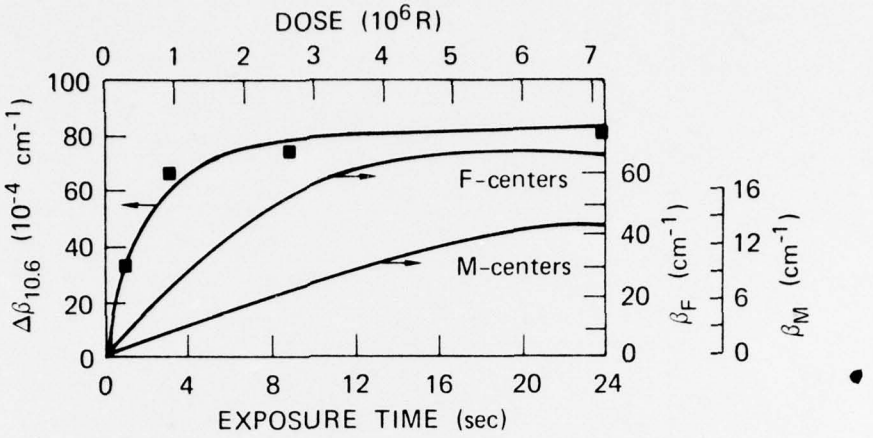

Fig. 5 β_F, β_M, and $\Delta\beta_{10.6}$ as a function of electron exposure time at 25°C in KCl-RbCl samples. Scales on the right refer to values of the absorption coefficients, β_F and β_M. The scale on the left refers to the change in the 10.6 μm absorption coefficient, $\Delta\beta_{10.6}$

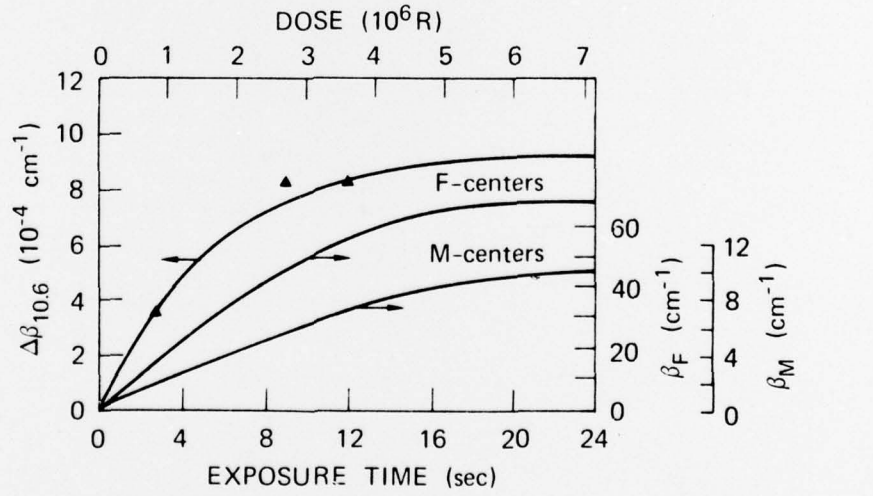

Fig. 6 β_F, β_M, and $\Delta\beta_{10.6}$ as a function of electron exposure time at 25°C in KCl-$EuCl_2$ samples. Scales on the right refer to values of the absorption coefficients β_F and β_M. The scale on the left refers to the change in the 10.6-μm absorption coefficients, $\Delta\beta_{10.6}$

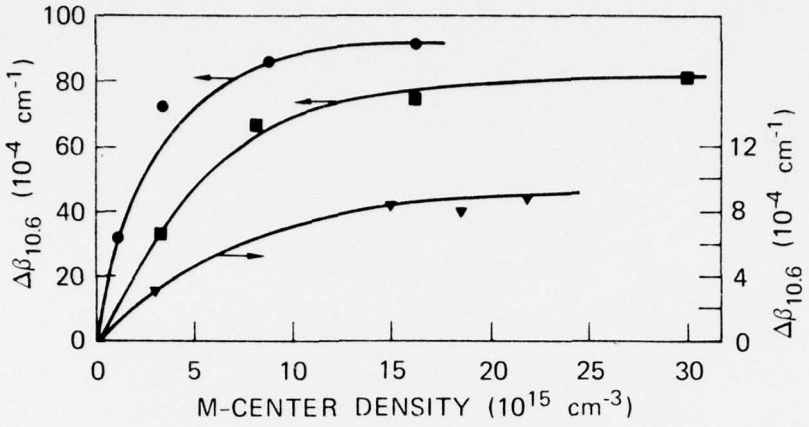

Fig. 7 Change in the 10.6-μm absorption coefficient $\Delta\beta_{10.6}$ as a function of M-center density in mixed KCl crystals. $\Delta\beta_{10.6}$ for KCl-$EuCl_2$ samples is referred to the scale at the right; $\Delta\beta_{10.6}$ for other samples is referred to thescale at the left. ●KCl-KBr; ■KCl-RbCl; ▼KCl-$EuCl_2$

10.6-μm absorption reaches a saturation limit at relatively low M-center densities. The KCl-$EuCl_2$ samples exhibit the smallest change in 10.6-μm absorption, approaching a saturation value of $\Delta\beta_{10.6} \approx 9 \times 10^{-4}$ cm^{-1} for M-center densities $> 1.5 \times 10^{16}$ cm^{-3}. In all cases, the mixed crystals show an initial rapid change in 10.6-μm absorption as a function of M-center density, followed by a region of relative saturation. For undoped KCl crystals, the change in 10.6-μm absorption exhibits a linear dependence on M-center concentration over the same density range.

The results suggest that the increase in 10.6-μm absorption can be related to the same mechanism causing absorption in F- or F-aggregate bands, or to the presence of Cl interstitial clusters introduced by the irradiation. In addition, it was considered possible that F- or F-aggregate bands, having a Lorentzian line shape, might contribute to the 10.6-μm absorption. The presence of interstitial clusters has been effectively eliminated as a michanism for increasing the infrared absorption.[16] Assuming a Lorentzian curve of the form:

$$\beta(\lambda) = \frac{b}{\pi\left(1 + C^2\right)\left(\frac{1}{\lambda} - \frac{1}{\lambda_m}\right)^2},$$

where λ_m is the wavelength at the peak of the absorption band, calculations based on the absorption data predict a greater absorption than the experimentally determined 10.6-μm absorption. Furthermore, the amplitudes of the F- and M-center absorption bands were often comparable and should exhibit, according to the previous equation comparable absorptions at 10.6 μm. However, this is not in agreement with the experimental data. Hence, Lorentzian band-shape tailing of absorption peaks from F- or F-aggregate centers cannot satisfactorily account for the increased infrared absorption in KCl.

To test this hypothesis and to obtain further information on the correlation between F- and F-aggregate centers and the increase in the 10.6-μm absorption coefficient, a number of the electron-irradiated samples were bleached with 0.55-μm light at nominal levels of 500 μ W per cm^2 for periods between 1 to 600 s. Subsequently, the 10.6-μm absorption coefficient was measured and the visible and near-infrared absorption spectra were recorded. In all cases, R- and N-centers appeared and increased in concentration during the early stages of bleaching. Figures 8 and 9 illustrate the results obtained for a KCl-RbCl sample. Figure 8 shows that the F-center absorption decreases continuously as a function of bleach time, while the M-center absorption increases rapidly, but decreases after a 30-s bleach time. In like manner, the R_2-center absorption increases, eventually decreasing for bleach times exceeding 120 s. Measurements obtained on all samples indicated a continual decrease in F- and F-aggregate center absorption for exposure times between 140 and 600 s. In Figure 9, the 10.6 μm absorption increases for bleach times < 120 s, but decreases thereafter.

A comparison of the data in Figures 8 and 9 indicates that the increase in the 10.6-μm absorption shows no positive correlation with the presence of F-centers, since the F-center absorption coefficient is decreasing. In contrast, the F-aggregate center absorptions are increasing when the infrared absorption is increasing. Changes in the M-center absorption coefficient cannot alone explain the large increase in $\Delta\beta_{10.6}$ observed in Figure 9 since it has been shown that relative changes in M-center absorption of the magnitude observed in the bleached samples are correlated with only small changes in $\Delta\beta_{10.6}$, while the increase and decrease of the R_2-center absorption coefficient show a direct correlation with the behavior of the 10.6-μm absorption. In particular, the R_2-center increases in concentration for times < 140 s, but decreases for longer F-light exposures. In all cases, for samples subjected to extremely long periods of bleaching, the eventual removal of F-aggregate centers is correlated

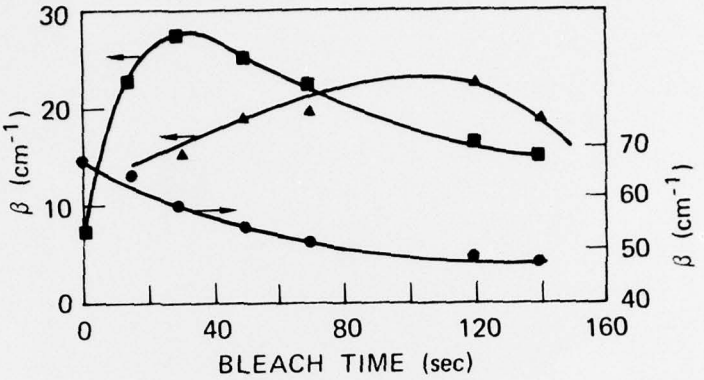

Fig. 8 β_F, β_M, and β_{R2}, as a function of bleach time for an electron-irradiated KCl-RbCl sample. After electron irradiation, the sample was exposed to 0.55-μm light for variable periods. All measurements were obtained at 25°C. Values of β_M and β_{R_2} are referred to the scale at the left and β_F, to the scale at the right. ■β_M; ▲β_{R_2}; ●β_F

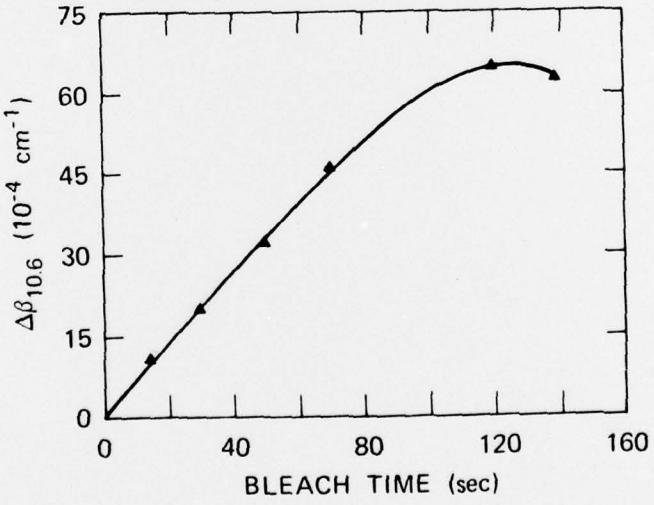

Fig. 9 Change in $\Delta\beta_{10.6}$ as a function of bleach time for an electron-irradiated KCl-RbCl sample

with a recovery of the 10.6-μm absorption coefficient to its approximate preirradiation value.

Additional experiments were conducted on single-crystal (undoped) KCL samples exposed to simultaneous electron and F-band irradiation. Figure 10 shows the F- and M-center absorption coefficients as a function of electron irradiation time for samples irradiated in the dark and in the presence of F-band illumination. The induced changes in the 10.6-μm absorption coefficient $\Delta\beta_{10.6}$ ($(\beta_{10.6})_0 \simeq 4 \times 10^{-4}$ cm^{-1}) under the two exposure conditions is also shown for comparison. The

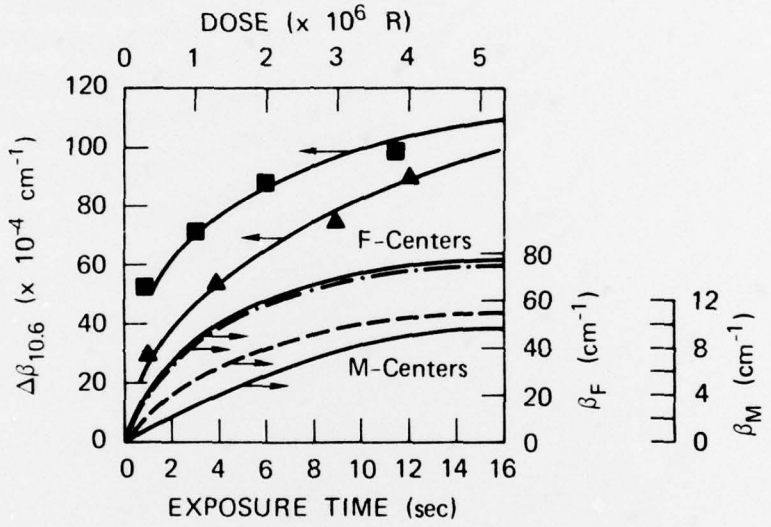

Fig. 10 β_F, β_M, and $\Delta\beta_{10.6}$ as a function of electron exposure time at 25°C for single-crystal KCl samples irradiated in the dark and in the presence of F-band illumination. The scales on the right refer to the value of the absorption constants determined at the peak position of the F-band (β_F) and M-band (β_M). The scale on the left shows the change in the 10.6-μm absorption coefficient $\Delta\beta_{10.6} = (\beta_{10.6})_f - (\beta_{10.6})_0$, where $(\beta_{10.6})_f$ represents the value of the absorption coefficient after irradiation and $(\beta_{10.6})_0$ the value for the uniradiated sample. ■ $\Delta\beta_{10.6}$ for samples illuminated with F-light during irradiation; ▲ $\Delta\beta_{10.6}$ for sample irradiated in dark; -·- β_F for sample illuminated with F-light during electron irradiation; ---- β_M for samples illuminated with F-light during electron irradiation; unbroken lines represent corresponding values of β_F and β_M for samples irradiated in the dark

data indicate that the F-center absorption coefficient exhibits essentially the same qualitative dose dependence for samples irradiated either in the dark or in the presence of F-illumination. However, in all cases, there was a slight reduction in β_F for samples irradiated simultaneously with F-light. In contrast, we observe that the M-center absorption coefficient as a function of dose is consistently higher for the illuminated samples than for those irradiated in the dark. Apparent saturation was observed[9] for KCl samples irradiated in the dark with electrons to dose levels $> 10^7$R. In all cases, $\Delta\beta_{10.6}$ was always larger for samples exposed to F-light during electron irradiation than those irradiated in the dark.

Figure 11 shows the change in $\Delta\beta_{10.6}$ as a function of M-center density for samples exposed to electron irradiation in the dark and in the presence of F-illumination. The results indicate that under both exposure conditions, the change in 10.6-μm absorption increases linearly as a function of M-center concentration, for doses $< 10^7$R. In contrast, data from the previous experiments on KCl samples show a saturation in $\beta_{10.6}$ for comparable F-center concentrations at doses $> 10^6$R. Comparison of the data in Figures 10 and 11 shows that the net effect of simultaneous electron irradiation and F-illumination is

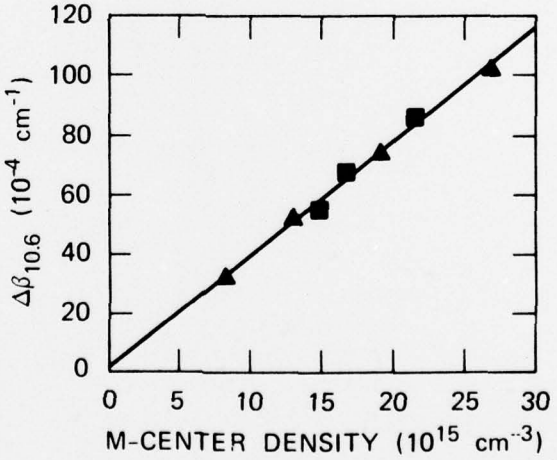

Fig. 11 $\Delta\beta_{10.6}$ as a function of M-center density in single-crystal KCl samples. ▲ samples irradiated in the dark; ■ samples illuminated with F-light during electron irradiation

to increase the concentration of M-centers relative to that observed for samples irradiated in the dark to similar dose levels. The increase in M-center concentration can subsequently be related to changes in $\Delta\beta_{10.6}$. Since the optical absorption spectra of all samples after irradiation indicated an apparent absence or relatively small concentration of N- and R-centers, it can be assumed that the observed changes in $\Delta\beta_{10.6}$ at doses $< 10^7$R are strongly correlated with the presence of M-centers and that contributions to $\Delta\beta_{10.6}$ by other F-aggregate centers are small by comparison.

Samples electron irradiated under both exposure conditions were subsequently illuminated with F-band light for periods up to 600 s to obtain additional information on the correlation between $\Delta\beta_{10.6}$ and F-aggregate center concentrations. Changes in β_F, β_M, β_{R_2}, and $\Delta\beta_{10.6}$ were measured as a function of bleach time, and the results are shown in Figures 12 to 14. In Figures 12 and 13, β_F continuously decreases as a function of bleach time, whereas β_M and β_{R_2} show a corresponding increase followed by a continual decrease for bleach times up to 600 s. For both samples, the concentration of M-centers increases rapidly as a function of time, reaching a maximum at bleach times between 25 and 30 s and decreasing thereafter. In Figure 14 the change in $\Delta\beta_{10.6}$ correspondingly exhibits a maximum in the same time period and continually decreases for bleach times >30 s.

Comparing the data shown in Figures 12 and 13 with those of Figure 14, we observe that the behavior of the $\Delta\beta_{10.6}$ curves can be directly correlated with changes in M-center concentration. However, the presence of increasing concentrations of R- and N-centers at bleach times >30 s and the extended tails of the $\Delta\beta_{10.6}$ bleach curves in Figure 14 indicate that the presence of F-aggregate centers other than the M-center also contributes to the change in $\Delta\beta_{10.6}$, but to a lesser extent.

Polycrystalline ZnSe Samples

In undoped ZnSe and ZnSe:Al crystals, a broad-band (2000 to 500 cm^{-1}) infrared absorption has been previously reported[17] at 77°K under xenon lamp excitation. The photoinduced absorption was ascribed to electronic transitions from neutral donor states of impurities or selenium vacancies to the conduction band. The characteristics of the infrared absorption band can be altered markedly upon exposure to ionizing radiation at 77°K. To our knowledge there have been no systematic studies of the radiation-induced change in the 10.6-μm absorption on currently available ZnSe samples exposed to high-energy electron irradiation at room temperature.

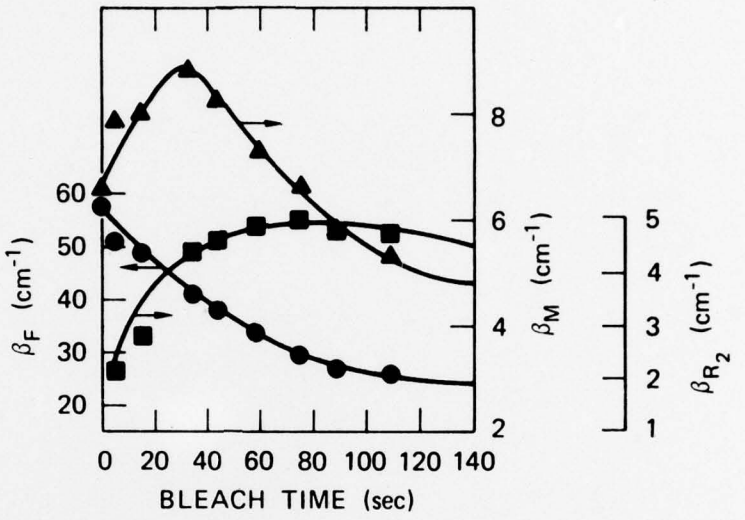

Fig. 12 β_F, β_M, and β_{R_2} as a function of bleach time for an electron-irradiated KCl sample. The sample was subjected to simultaneous electron beam irradiation and F-band illumination for a period of 4 s and subsequently bleached with 0.55-μm light for variable periods. All measurements were obtained at 25°C. Values of β_M and β_{R_2} are referred to the scales at the right and of β_F to the scale at the left. ▲β_M; ■β_{R_2}; ●β_F

We have irradiated ZnSe samples in the dark and in the presence of Hg-lamp illumination with 1-MeV electrons at a dose rate of 3.3×10^5R/s. Samples were characterized before irradiation using TEM analysis as discussed in the previous section.

Figure 15 shows the change in the 10.6-μm absorption coefficient as a function of exposure time. The results obtained in these experiments showed that essentially the same change in $\Delta\beta_{10.6}$ was

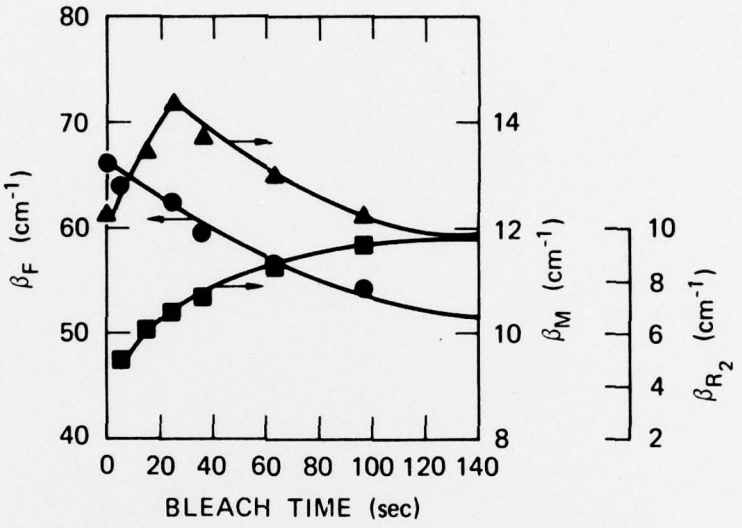

Fig. 13 β_F, β_M, and β_{R_2} as a function of bleach time for an electron-irradiated KCl sample. The sample was subjected to electron beam irradiation in the dark for a period of 2 s and subsequently bleached with 0.55-μm light for variable periods. All measurements were obtained at 25°C. Values of β_M and β_{R_2} are referred to the scales at the right and of β_F to the scale at the left. ▲β_M; ■β_{R_2}; ●β_F

observed, independent of whether or not the sample was illuminated during electron irradiation. All samples exhibited a relative saturation in $\Delta\beta_{10.6}$ at doses >12 MR. In extended irradiations to 50 MR, there was no significant variation from the saturation value of $\Delta\beta_{10.6}$.

Of particular interest was the observation that samples containing the highest concentration of growth defects (Zn precipitates, dislocation lines, and tangles) consistently exhibited the largest change in effective infrared absorption after irradiation. In the previous section, we presented data showing that the presence of

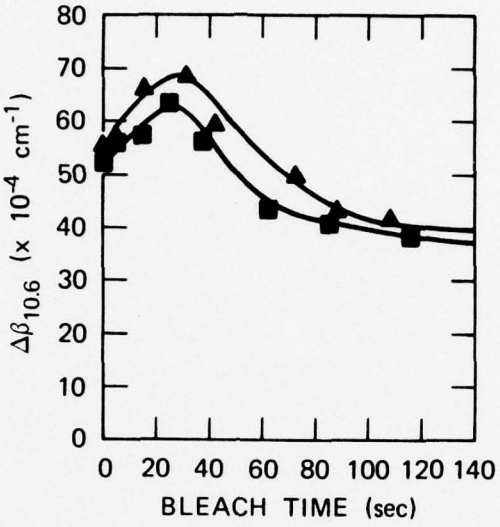

Fig. 14 Change in $\Delta\beta_{10.6}$ as a function of bleach time. $\Delta\beta_{10.6}$ represents the difference between $\beta_{10.6}$ measured before irradiation and $\beta_{10.6}$ after irradiation and bleach. ▲$\Delta\beta_{10.6}$ for sample in Fig. 12; ■$\Delta\beta_{10.6}$ for sample in Fig. 13

defects and collected scattering centers could be correlated with changes in β_o at 10.6 μm. The radiation-induced change in $\Delta\beta_{10.6}$ is also thought to be related to the retention of residual damage introduced during electron bombardment. The growth defects present in the ZnSe samples are known to act as capture sites for defects and will result in a slightly larger shift in $\Delta\beta_{10.6}$ as observed in Figure 1. Annealing the samples in a vacuum at temperatures of $\sim$ 900°C for 12 hr does appear to result in some slight recovery of $\beta_{10.6}$, but long extended anneals would be required to reduce the 10.6-μm absorption to its approximate preirradiation value.

From the data obtained, it is apparent that high-energy electron irradiation at room temperature produces a small but perceptible shift in the infrared absorption at 10.6 μm. However, the largest changes in absorption should occur during and immediately after high-dose-rate pulsed electron or x irradiation, and additional experiments are required to identify the transient infrared response of ZnSe.

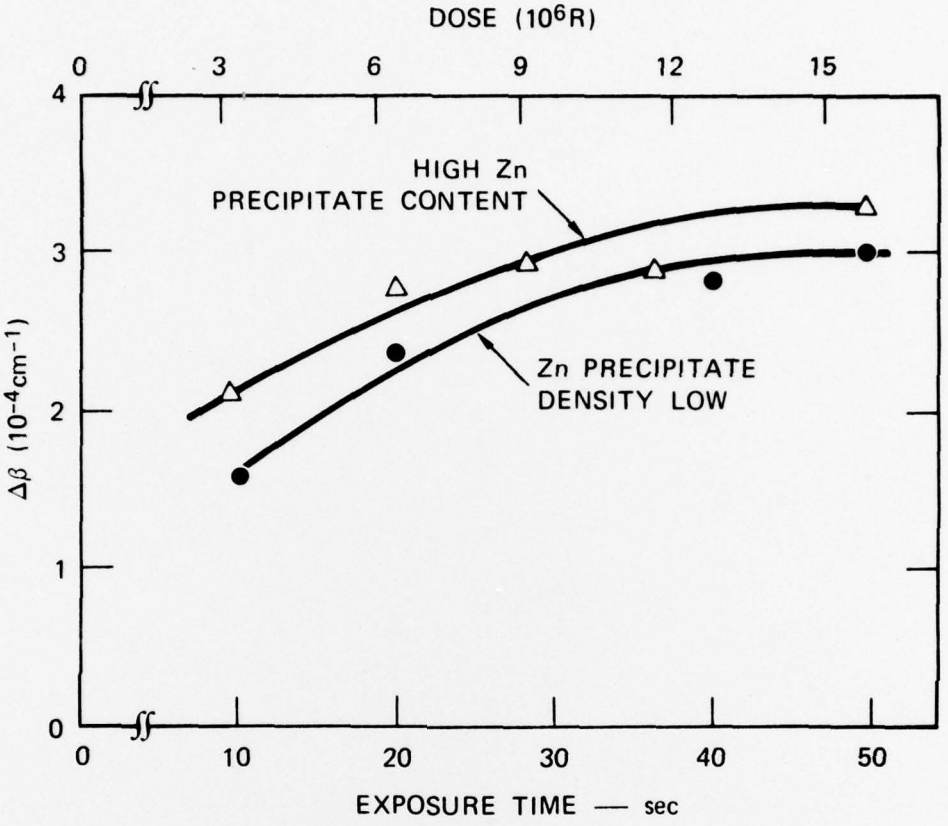

Fig. 15 Change in $\Delta\beta_{10.6}$ as a function of electron exposure time at 25°C for polycrystalline CVD-ZnSe samples containing variable densities of Zn precipitates and initial growth defects

CONCLUSIONS

We have studied materials phenomena in materials of interest to the high-power laser community. Our study included a determination of the relationship between microstructural defects and the optical properties of compound semiconductor materials used for laser window and a study of the effect of high-energy electrons on the optical properties of semiconductor and alkali halide laser windows.

Infrared microscopic examination of CdTe and ZnSe samples revealed the presence of localized absorption sites that have been

shown to function as preferential damage regions under high-power laser illumination. Detailed microstructural examinations showed that these absorption sites were associated with distinct defect aggregations (complex arrays of dislocation lines, aligned stacking faults, and precipitates of compounds involving the compensating impurity).

Our study of radiation-induced effects revealed that for some optical materials, irradiations with ionizing radiation will cause substantial increases in the infrared absorption in important spectral bands. Our study included mixed crystal KCl (i.e., KCl-KBr, KCl-RbCl, and KCl-$EuCl_2$) as well as undoped single crystal KCl. We found that the optical properties of the mixed crystals were considerably less sensitive to the ionizing radiation than the undoped samples. It was determined that the principal cause of the degradation of the optical properties was the formation of F-aggregate centers, principally M centers.

The ZnSe windows, irradiated at room temperature, also were degraded by exposure to ionizing radiation, but to a lesser degree than the alkali halide windows. In addition, we found that the samples with the highest defect concentrations exhibited the largest radiation-induced infrared absorption. It also should be realized that if a particular application results in the semiconductor windows being cooled during irradiation, the radiation-induced optical degradation would be expected to be much greater.

It would be of interest to determine the bleaching behavior of the center as a function of illumination intensity. If non-linear bleaching is observed, radiation damaged alkali halides may be suitable for use as saturable absorbers.

REFERENCES

1. T. J. Magee, J. Peng and J. Bean, Proc. Electron Micros. Soc. Amer., Claitor Publ. Co., Baton Rouge, Louisiana, 1974, p. 548.
2. T. J. Magee, N. M. Johnson, M. Lehmann, J. Peng and J. Hannigan, Rev. Sci. Instruments 47, 301 (1976).
3. M. Hass, J. W. Davisson, H. B. Rosenstock and J. Babiskin, Appl. Opt. 14, 1128 (1975).
4. L. H. Skolnik, A. Hordrick and A. Kahan, Appl. Phys. Lett. 23, 477 (1973).

5. E. Bernal, Appl. Opt. 14, 314 (1975).

6. M. Sparks and L. J. Sham, Solid State Comm. 11, 1451 (1972).

7. M. Sparks, 4th Amer. Soc. Testing Mater. Symp. - Damage in Laser Mater., Boulder, Colorado, 1972 (unpublished).

8. T. J. Magee, J. Peng and J. Bean, Phys. Stat. Solidi (A) 27, 557 (1975).

9. T. J. Magee, SRI Technical Report No. 2266-1, Menlo Park, California, 1972.

10. C. Phillipi, U.S. Air Force Materials Lab., Dayton, Ohio, 1973 (unpublished data).

11. T. J. Magee, N. M. Johnson and J. Peng, Phys. Stat. Solidi (A) 30, 81 (1975).

12. T. J. Magee, N. M. Johnson and J. Peng, Phys. Stat. Solidi (A) 33, 415 (1975).

13. J. R. Hopkins, J. J. Martin and J. Larkin, J. Appl. Phys. 45, 2804 (1975).

14. J. Arends, H. W. Den Hartog and A. J. Dekker, Phys. Stat. Sol. 10, 105 (1965).

15. P. B. Still and D. Pooley, Phys. Stat. Sol. 32, K147 (1969).

16. H. G. Lipson, P. Ligor, A. Kahan and J. J. Martin, Bull. Amer. Phys. Soc. 20, 377 (1975).

17. S. Miyamoto, S. Kawashima and S. Shionoya, J. Phys. Soc. Japan 24, 1182 (1968).

---

† Research supported by the Air Force Office of Scientific Research under Contract F44620-73-C-0019.

** Present address, Advanced Research and Applications Corporation, P.O. Box 1439, Los Altos, California 94022